ABSTRACT

ELASTIC NEUTRON-PROTON CHARGE EXCHANGE SCATTERING

BETWEEN 1.75 GeV/c AND 7.20 GeV/c

by

Smith Thompson Powell,III

Chairman: Michael J. Longo

The differential cross sections for neutron-proton elastic scattering in the charge exchange region have been measured for incident neutron momenta between 1.75 GeV/c and 7.20 GeV/c. A neutron beam with a broad energy spectrum was produced by steering the external proton beam from the Bevatron onto a beryllium target. After collimation the neutrons were scattered off the protons in a liquid hydrogen target. The momenta of the forward-going protons were measured in a magnet and spark chamber system, while the much less energetic neutrons were detected by an array of thick scintillation counters. The detection efficiencies of the thick plastic scintillators were calculated. Several possible contaminating processes were investigated by Monte Carlo techniques, and were shown to be effectively eliminated by the cuts made on the data. The data indicate the existence of an energy dependent structure in the differential cross sections.

ELASTIC NEUTRON-PROTON CHARGE EXCHANGE SCATTERING

BETWEEN 1.75 GeV/c AND 7.20 GeV/c

by

Smith Thompson Powell,III

A dissertation submitted in partial fulfillment
of the requirements for the degree of
Doctor of Philosophy in
The University of Michigan
1970

Doctoral Committee:

    Professor Michael J. Longo, Chairman
    Professor Byron P. Roe
    Professor Robert S. Tickle
    Associate Professor Gordon L. Kane
    Assistant Professor Henry C. Griffin

ACKNOWLEDGMENTS

TABLE OF CONTENTS

LIST OF TABLES

LIST OF FIGURES

I. INTRODUCTION

A. General Comments

The neutron-proton charge exchange experiment described
here was a part of a more encompassing experiment designed
to measure the n-p differential cross sections over a large
range of the center-of-mass scattering angle and as a
function of energy. Despite its fundamental importance,
very little was known about the n-p interaction above 1 GeV
at the time of the conception of this experiment. The only
existing data were, in fact, charge exchange data at 2.04
GeV and 2.85 GeV.[1] The lack of data could be attributed,
in part, to the difficulty of working with neutron beams.

The experiment, which was performed in 1964, was
divided into two parts as dictated by the energies of the
scattered neutrons. That is, for scattering angles ≤150°
in the center-of-mass system, the scattered neutrons had
energies greater than 0.5 GeV and could be detected by
their interactions in an array of thick-plate spark chambers
and scintillation counters. In the charge exchange region
(scattering angles ≥150° in the center-of-mass) the scattered
neutrons did not have sufficient energy to trigger such a
detection system. The charge exchange data were taken with
an array of thick plastic scintillation counters as neutron
detectors in place of the steel chambers. Otherwise, the
two parts of the experiment employed essentially identical
equipment and techniques.

Only the charge exchange data will be discussed in this report. For the details and results of the other phases of the experiment, the reader is referred to the published accounts.[2]

Previous charge exchange experiments detected only the recoil proton. Below 1 GeV it was possible to produce monochromatic neutron beams or to use time-of-flight techniques to determine the energy of the incident neutrons. Above 1 GeV a double charge exchange technique was used to set the energy of the experiment. In this technique a proton beam was directed at a target and a neutron beam taken off at zero degrees with respect to the proton beam. The neutron beam scattered off a second target which was composed of liquid hydrogen, and the protons which recoiled at small angles were detected. Charge exchange processes in both targets gave recoil protons with the full energy of the initial proton beam. By accepting only such protons, the experimenter could be assured that the n-p interaction were elastic.

This experiment employed a new technique to measure simultaneously the charge exchange cross sections over a large energy range. The idea was to use a neutron beam containing a broad range of neutron energies (up to the accelerator energy) and to use the kinematics of the elastic events to determine the energy of the incident neutron on an event by event basis. To this end, both the recoil proton and the scattered neutron were detected. This

provides a powerful means of rejecting inelastic events since it is possible to measure the neutron angle and, somewhat crudely, its energy by time-of-flight. The efficacy of this technique is illustrated in Figure 1 which compares the kinematics for n-p charge exchange with those for the reaction $n+p \rightarrow \Delta^+(1236)+n$. Figure 1 also shows the kinematical limit for neutrons produced by any inelastic process. (The process $n+p \rightarrow n+(p+\pi)$ in which the pion and the proton go off together gives neutrons most nearly like those produced in the elastic scattering.) We see there is a rather large range of neutron lab angles (which covers the extreme backward peak in the cross sections) from which the inelastic neutrons are excluded. It seemed, therefore, that the elastic and inelastic events could be sufficiently separated so that the differential cross sections for n-p charge exchange could be measured simultaneously for several energies. The experiment was thus of an exploratory nature in that a principle goal was to test the technique.

The neutron beam used for both phases of the experiment was produced by steering the Bevatron external proton beam onto a beryllium target. The protons, which had kinetic energies of 6.3 GeV, produced neutrons with a broad energy spectrum which peaked in the vicinity of 5 GeV. Downstream from the beryllium target a large magnet swept the remaining protons and other charged contaminants from the beam. After passing through a defining collimator the neutrons struck a liquid hydrogen target. The charge
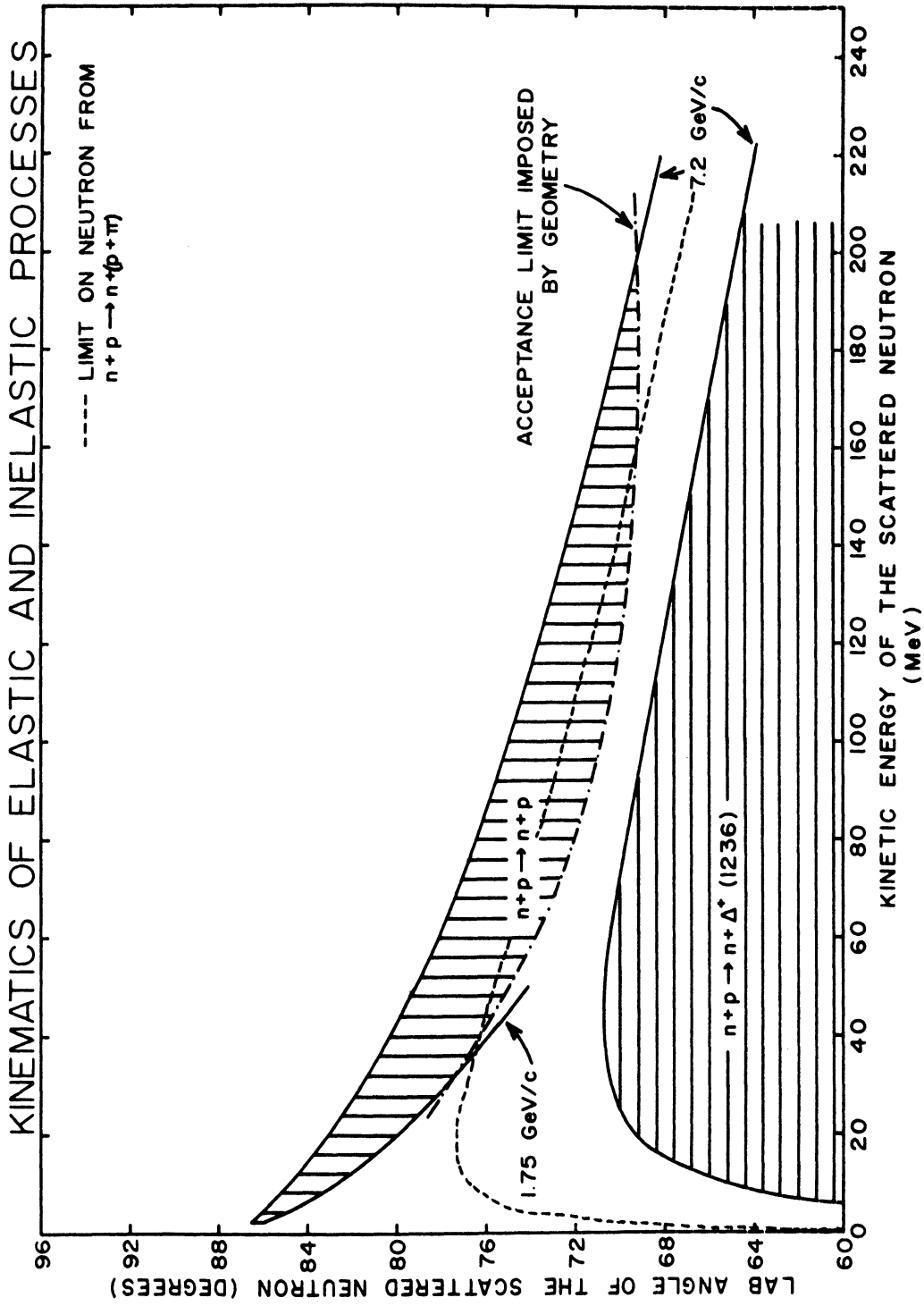
Fig. 1 Kinematics of Elastic and Inelastic Processes

exchange interaction produced a proton which carried nearly the full energy of the beam particle and which proceeded at a small angle with respect to the beam line. In contrast, the scattered neutron carried very little kinetic energy (1-200 MeV) and its flight path was at approximately right angles to the beam line.
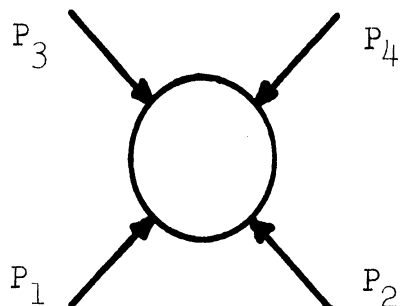
The momenta of the forward-going protons were measured in a spectrometer composed of a bending magnet and four thin-foil spark chambers. If it were assumed that the interaction was n-p elastic, knowledge of the proton momentum allowed one to solve the kinematical equations for the incident neutron momentum.

The scattered neutrons were detected by an array of thick plastic scintillators. In addition to indicating the presence of a neutron, the neutron detectors provided a coplanarity restriction and a crude determination of the neutron scattering angle. Further, the detectors provided time-of-flight information which was displayed on an oscilloscope and photographed. The information supplied by the neutron detectors was used in the later analysis to weed out inelastic events.

B. Kinematical Preliminaries

The Mandelstam variables are particularly useful for connecting experiment with theory.[3] For the purpose of developing these Lorentz invariant variables we restrict the discussion to two-body nucleon-neucleon collisions in

which we neglect the neutron-proton mass difference. We

define the Mandelstam variables s, t, and u by:

$$s=-(P_1+P_2)^2$$

$$t=-(P_1+P_3)^2 \tag{1}$$

$$u=-(P_1+P_4)^2$$

in which the four-momentum is defined by

$$P=(\vec{p},iE) \tag{2}$$

and

$$P^2=p^2-E^2=-m^2 \tag{3}$$

where $\vec{p}$ is the ordinary momentum, E is the total energy,

and m is the rest mass. As we have drawn all of the

four-momenta pointing in, we have not specified a scattering

process. The fundamental hypothesis is that a single

scattering amplitude, $A(s,t,u)$, will describe any two-body

nucleon process which one can represent by reversing the

directions of any two of the four-momenta. In the case of

n-p elastic scattering the processes could be represented

as shown in Fig. 2.

The interaction under study is usually referred to as

the "s channel". It should also be noted that the s, t,

and u are not independent, but rather are constrained by

THE VARIABLES s,t,u

s channel

P_1	P_2	P_3	P_4
$n + p$	$\rightarrow$	$n + p$
$\bar{n} + \bar{p}$	$\rightarrow$	$\bar{n} + \bar{p}$

$s = -(P_1 + P_2)^2$
$t = -(P_1 - P_3)^2$
$u = -(P_1 - P_4)^2$

t channel

P_1	P_2	P_3	P_4
$\bar{p} + p$	$\rightarrow$	$n + \bar{n}$
$\bar{n} + n$	$\rightarrow$	$p + \bar{p}$

$s = -(P_1 - P_2)^2$
$t = -(P_1 + P_3)^2$
$u = -(P_1 - P_4)^2$

u channel

P_1	P_2	P_3	P_4
$n + \bar{p}$	$\rightarrow$	$n + \bar{p}$
$\bar{n} + p$	$\rightarrow$	$\bar{n} + p$

$s = -(P_1 - P_2)^2$
$t = -(P_1 - P_3)^2$
$u = -(P_1 + P_4)^2$
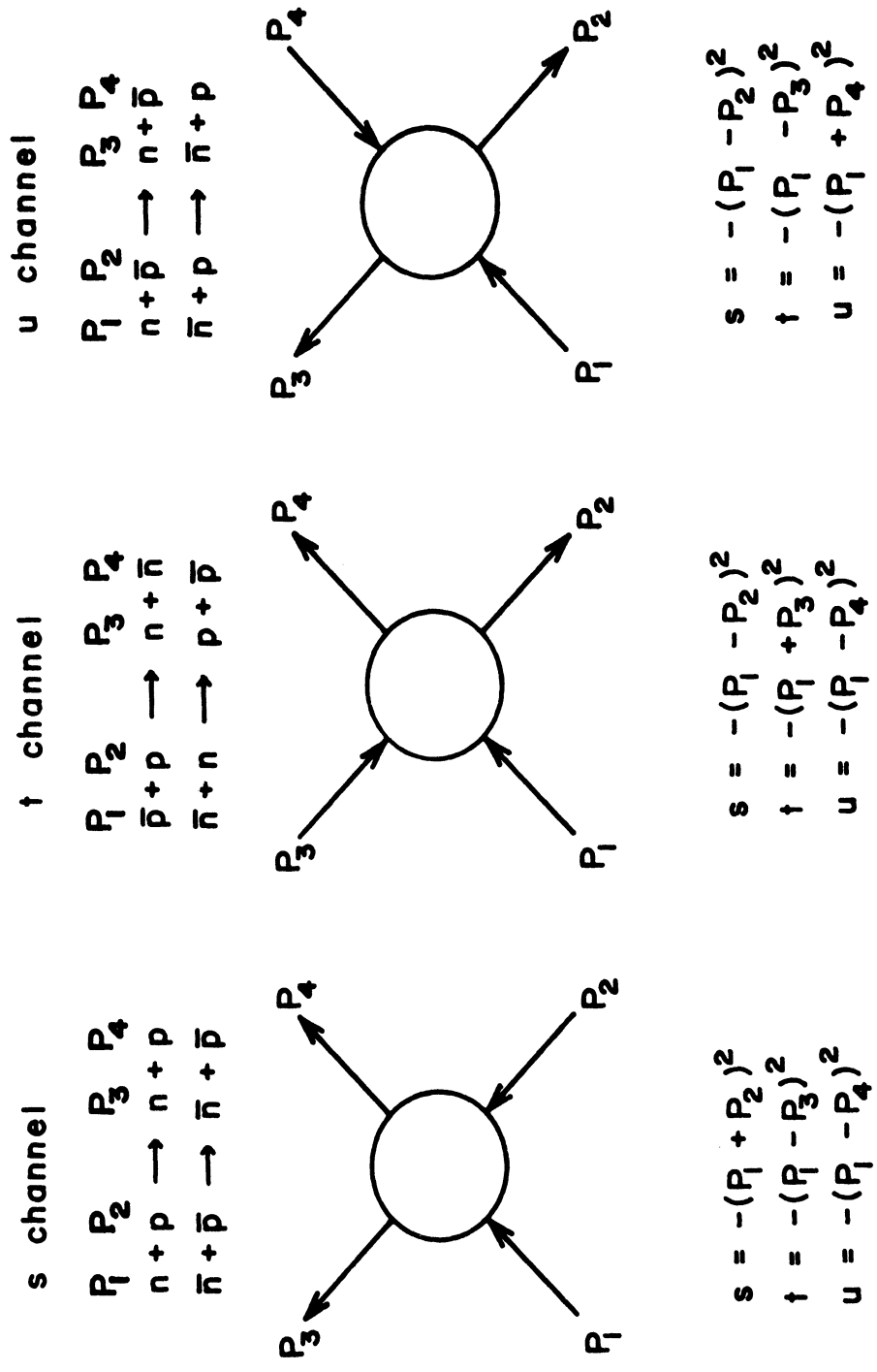
Fig. 2 The Variables s, t, u

the equation

$$s+t+u=4m^2 \tag{4}$$

in which m is the mass of the nucleon.

We now consider an n-p scattering in the center-of-mass system and label the four-momenta of the particles as shown.

$$n + p \rightarrow n + p$$

$$P_1 \quad P_2 \quad P_3 \quad P_4$$
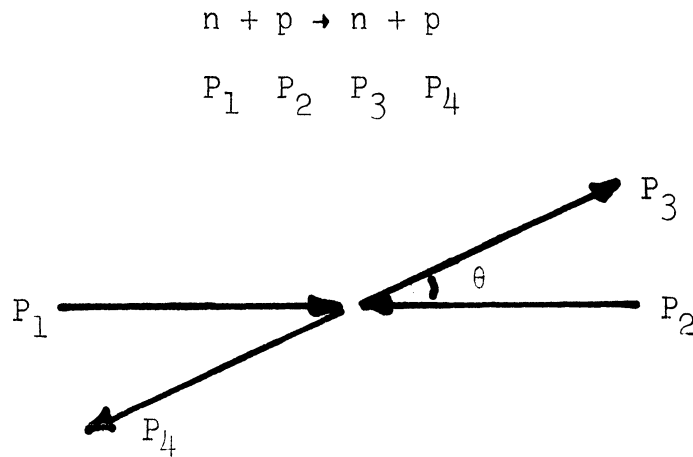
In the center-of-mass system it can be shown that

$$s=(E_1+E_2)^2$$

$$t=-2p^2(1-\cos\theta) \tag{5}$$

$$u=-2p^2(1+\cos\theta).$$

The differential cross section can be expressed as $d\sigma/dt$ for foward scattering and $d\sigma/du$ for backward scattering. Neutron-proton charge exchange scattering is backward elastic scattering. However, it should be noted that many authors reverse the definitions of t and u when discussing backward scattering so that they can express the backward

differential cross section as $d\sigma/dt$. Another useful

relation may be obtained by evaluating u in the lab system

in which case

$$u=-2mT \qquad (6)$$

where T is the kinetic energy of the scattered neutron in

the lab system. Finally, the differential cross section

as a function of angle in the center-of-mass system is

related to the differential cross section as a function

of four-momentum transfer by

$$\frac{d\sigma}{d\Omega} = \frac{p^2}{\pi} \frac{d\sigma}{du}.\qquad (7)$$

II. SURVEY OF EXPERIMENTAL DATA AND THEORY

A. Experimental Data

In 1962 Palevsky et al.[1] published the results of their n-p charge exchange experiment at beam kinetic energies of 2.04 GeV and 2.85 GeV. Although, as we shall see, quite a bit of n-p charge exchange data existed at lower energies, the attention of the physics community was focused on the multi-GeV experiments. Palevsky and his colleagues noted that the n-p backward cross section at u=0 was an order of magnitude less than the p-p forward cross section at t=0. The charge exchange data also exhibited a very much sharper peak than that found in p-p scattering. The sharp peak indicated an interaction range of the order of 2 Fermis rather than the accepted nucleon size of 1 Fermi. And finally, the data posed a problem as to which particles mediated the interaction. The one-pion exchange contribution varies as the square of the four-momentum transfer and should, therefore, give a dip at u=0. However, the exchange of higher mass particles would have been inconsistent with the narrow peak.

In 1965 the same group extended their measurements to 2.2 GeV.[4] They combined their new data with their data at 2.04 GeV and plotted $d\sigma/du$ versus $-u$. In this plot the extreme peaking of the data was more apparent. They parameterized the data as

$$\frac{d\sigma}{du} = 6.9e^{49u} + 4.1e^{4u}. \tag{8}$$

Shortly thereafter Manning et al.[5] published data
for n-p charge exchange at 8 GeV/c. When plotted against
-u their data showed a somewhat sharper peak than that
observed at the lower energies. Further the u=0 differen-
tial cross section was found to decrease rapidly with
increasing energy. The data of Friedes et al. and that of
Manning et al. are shown in Fig. 3.

In 1965 Wilson[6] redirected attention to the low
energy data in an analysis of the energy and the
four-momentum transfer dependence of n-p charge exchange
data. He plotted the data against -u for all energies and
observed that a single curve, normalized to the u=0 values,
fitted the data reasonably well from 91 MeV to 2850 MeV.
He simply drew a smooth line through the data at 350 MeV
to obtain the curve to which he compared all of the data.
He also noted that $d\sigma/du(u=0)$ was a strong function of
energy. He concluded that, over a large energy range, the
variation of the cross section with energy and the variation
with four-momentum transfer were independent.

In 1969 Mischke et al.[7] measured the charge exchange
differential cross sections for beam momenta between 600
MeV/c and 2000 MeV/c. They divided their data into fifteen
momentum bins and fitted the data in each bin to

$$\frac{d\sigma}{du} = \left(\frac{d\sigma}{du}\right)_{u=0} e^{\beta u} \tag{9}$$

in which they restricted the range of u to cover the sharp
peak. Combining their data with those of other experi-
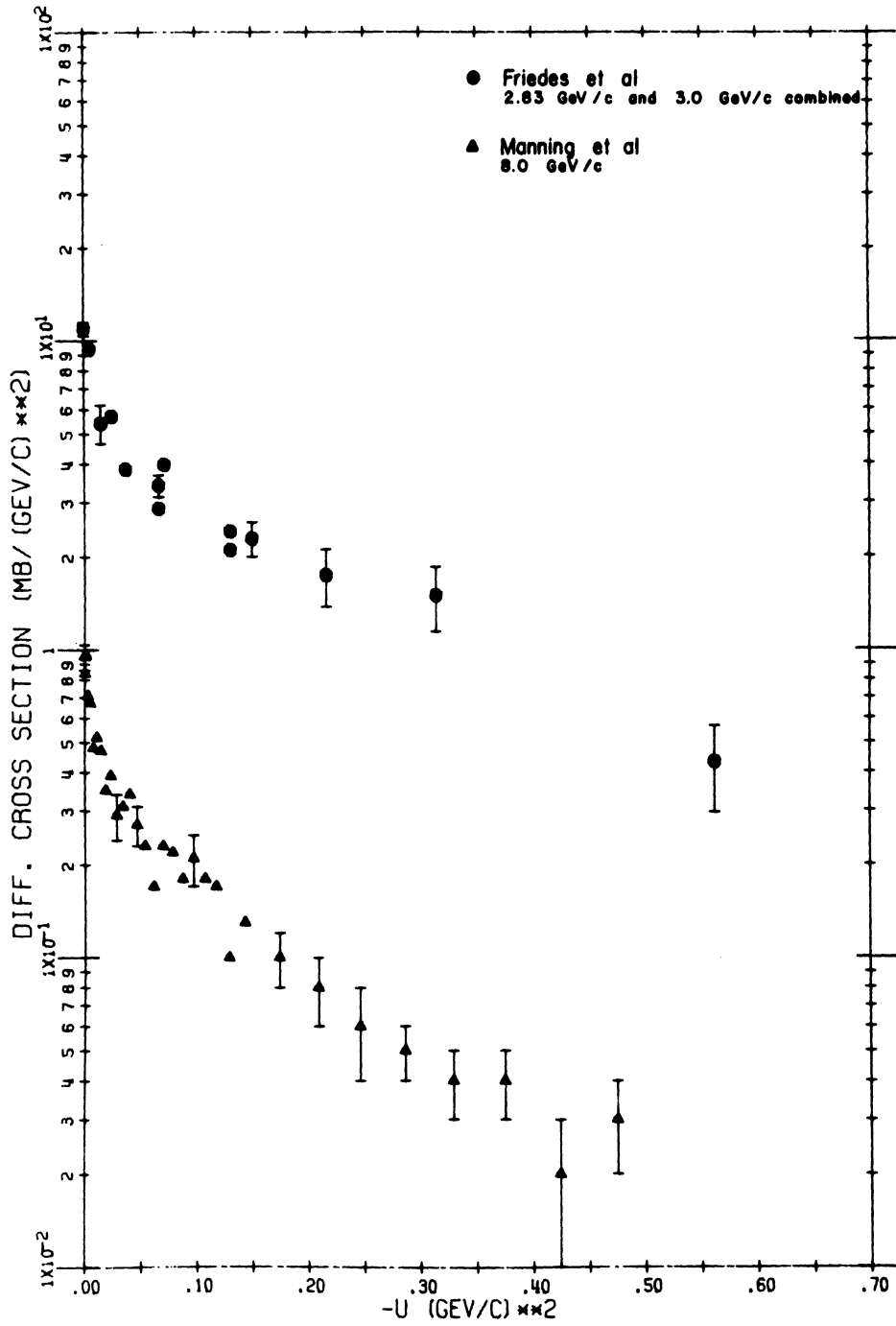
Fig. 3   The n-p Charge Exchange Data of Friedes et al. and of Manning et al.

menters, they showed that β increased from about 20 $(GeV/c)^{-2}$ at an incident momentum equal to 0.3 GeV/c to a maximum of 110 $(GeV/c)^{-2}$ in the neighborhood of 0.8 GeV/c. β then decreased to about 20 $(GeV/c)^{-2}$ at momenta around 2 GeV/c before increasing to 70 $(GeV/c)^{-2}$ at 8 GeV/c momentum. Thus the behavior at small u was considerably more complicated than that suggested by Wilson.

B. Theory

The nature of the nucleon-nucleon force has always presented many difficulties for theorists. Yukawa first conjectured that the force was mediated through the exchange of a particle—later identified as the pion.[8] During the following years attempts were made, with some success, to write down a potential involving pion exchange.[9] However, as the energies under consideration increased the validity and usefulness of the concept of a potential became more and more questionable. In recent years the emphasis has been on an S-matrix approach which relies heavily on phenomenological input.[10]

Implicit in the S-matrix approach is the fact that a theory of n-p charge exchange has many constraints placed on it. For instance, as discussed in Section I-B, the amplitude which describes np→np must also describe p̄p→nn̄ and np̄→np̄. Further, isotopic spin invariance leads to connections between np and pp cross sections. And finally, completely different reactions may involve some of or all

of the same Regge exchanges. Adjusting the exchange parameters to fit n-p charge exchange has consequences for other reactions.

In 1958 Chew[11] gave a prescription for extrapolating n-p charge exchange data to the pion pole and thereby determining the pion-nucleon coupling constant. At energies less than 1 GeV several experimenters performed the extrapolation.[12-14] With some difficulty they all were able to obtain values for the pion-nucleon coupling constant which were in good agreement with the values obtained from pion-nucleon scattering experiments. Therefore, it was somewhat surprising that the early papers, in the main, ignored the one-pion exchange when attempting to explain the data of Palevsky et al.

However, Drell[15] had pointed out that the exchange of a single pion gave an amplitude which was proportional to u, and that the amplitude should therefore vanish at u=0. Consequently, following the publication of the data of Palevsky et al., several authors[16-19] attempted to fit the data with exchanges of various combinations of elementary particles or of Regge poles, but in which no attempt was made to include u=0 pion effects. These theories were not able to fit all of the relevant data.

An exception to these attempts was found in an early paper which was written by Phillips.[20] He noted that one-pion exchange, through interference with a large, broad background due to other processes, could lead to

a sharp backward peak. He chose the background amplitudes

to fit the data.

With the realization that absorptive effects could

drastically alter the effects of one-particle exchange,[21]

theorists reconsidered one-pion exchange. It was noted

that absorption corrections could change the one-pion contri-

bution at u=0 from a dip to a peak. Unfortunately, the

many attempts to fit the n-p charge exchange data with

absorptive corrections indicated the presence of a

secondary maximum which was not evident in the data.[22-24]

Another difficulty was that, as noted above, the charge

exchange peak persisted to very low energies—even below

the threshold for any inelastic processes. Thus absorp-

tive effects could not explain the low energy data.

Other schemes to alter the u=0 contribution to the

scattering amplitude involved conspiracies and daughter

trajectories.[25-27] A conspiracy requires two trajectories

with opposite parities which coincide at u=0. Daughter

trajectories form an infinite series of trajectories whose

spin values at u=0 are depressed by 1,2,3,... units from

the parent trajectory. However, it was recognized that

these mathematical constructs represented weaknesses in

the theory and were not well motivated physically.[26,28]

A more physically motivated model was developed by

Byers and Yang[29] and was applied to n-p charge exchange

by Byers.[30] Their "coherent droplet" model combines

absorptive effects for small impact parameters with one-pion exchange for longer range interactions.

At the present time several theorists are attempting to fit a large number of processes, including n-p charge exchange, using Regge pole exchanges and Regge cuts.[28,31] The cuts are due to absorptive effects. The processes and exchanges which they consider are summarized in Table I. Their efforts seem to be meeting with some success.

One difficulty which remains is that of explaining the presence of the sharp peak at low energies where absorptive effects can play no role. At high energies absorptive effects modify the low partial waves the most. It has been suggested[32] that for low energies the elastic unitarity requirement modifies the lower partial waves in qualitatively the same way as do absorptive effects at higher energies.

In concluding this survey it should be noted again that the attempt to understand the nucleon-nucleon force has been beset with many difficulties. However, progress has been made. It now seems clear that one-pion exchange effects must be considered in attempts to describe the n-p backward peak. Further, it seems clear that absorptive effects must somehow be included. Finally, the realization that many diverse processes must be considered simultaneously presents an exciting challenge to theorists.

Processes		Exchanges
Charged Photoproduction	$\gamma p \to \pi^+ n$ $\gamma n \to \pi^- p$	π, ρ, A
Neutral Photoproduction	$\gamma p \to \pi^\circ p$ $\gamma p \to \eta^\circ p$	ρ, ω
Nucleon-Nucleon Charge Exchange	$np \to pn$ $p\bar{p} \to n\bar{n}$	π, ρ, A
Backward Pion Scattering	$\pi^+ p \to p\pi^+$ $\pi^- p \to p\pi^-$ $\pi^- p \to n\pi^\circ$	N, Δ
Backward Photoproduction	$\gamma p \to \pi^+ n$ $\gamma p \to \pi^\circ p$	N, Δ

Table I   Processes and Exchanges[31]

III. EXPERIMENTAL APPARATUS AND PROCEDURES

A. Neutron Beam

Neutrons were produced by focusing the Bevatron external proton beam onto a beryllium target. Approximately $5-7 \times 10^{10}$ protons with 6.3 GeV kinetic energy were supplied during each 300 msec flat-top beam spill. The repitition rate was about nine pulses per minute. The beryllium target presented a cross section to the proton beam of 1/4 inch by 3/8 inch and was 8 inches long, or about 0.68 collision lengths, so that approximately 50% of the protons scattered in the target. Figure 4 shows the layout of the neutron beam production area.

The proton beam size and position were monitored in two ways. For the first method, a mask composed of two thin scintillation counters mounted on 53AVP photomultiplier tubes as shown in Fig. 5 were placed immediately upstream of the beryllium target. The outputs from these counters were displayed on an oscilloscope. For the second method, a thin piece of clear plastic scintillator was placed directly in front of the target and viewed through a closed circuit TV system. The target, the counter mask, and the beam spot could be seen. With these two methods, shifts of the beam spot of about 1/16 inch could be detected, and the beam size could be monitored. The structure in the beam spill was also monitored with the oscilloscope display of the outputs from the mask counters.
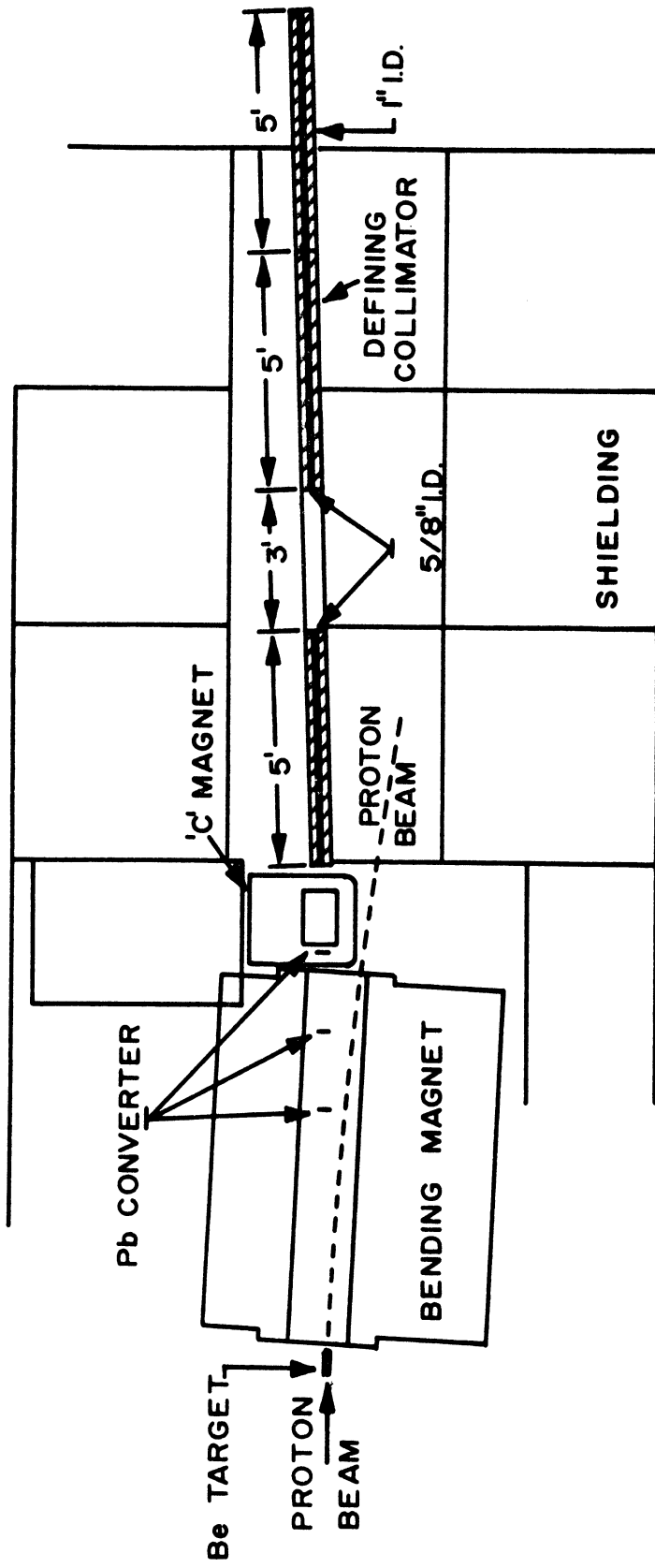
Fig. 4   The Neutron Beam Production Area
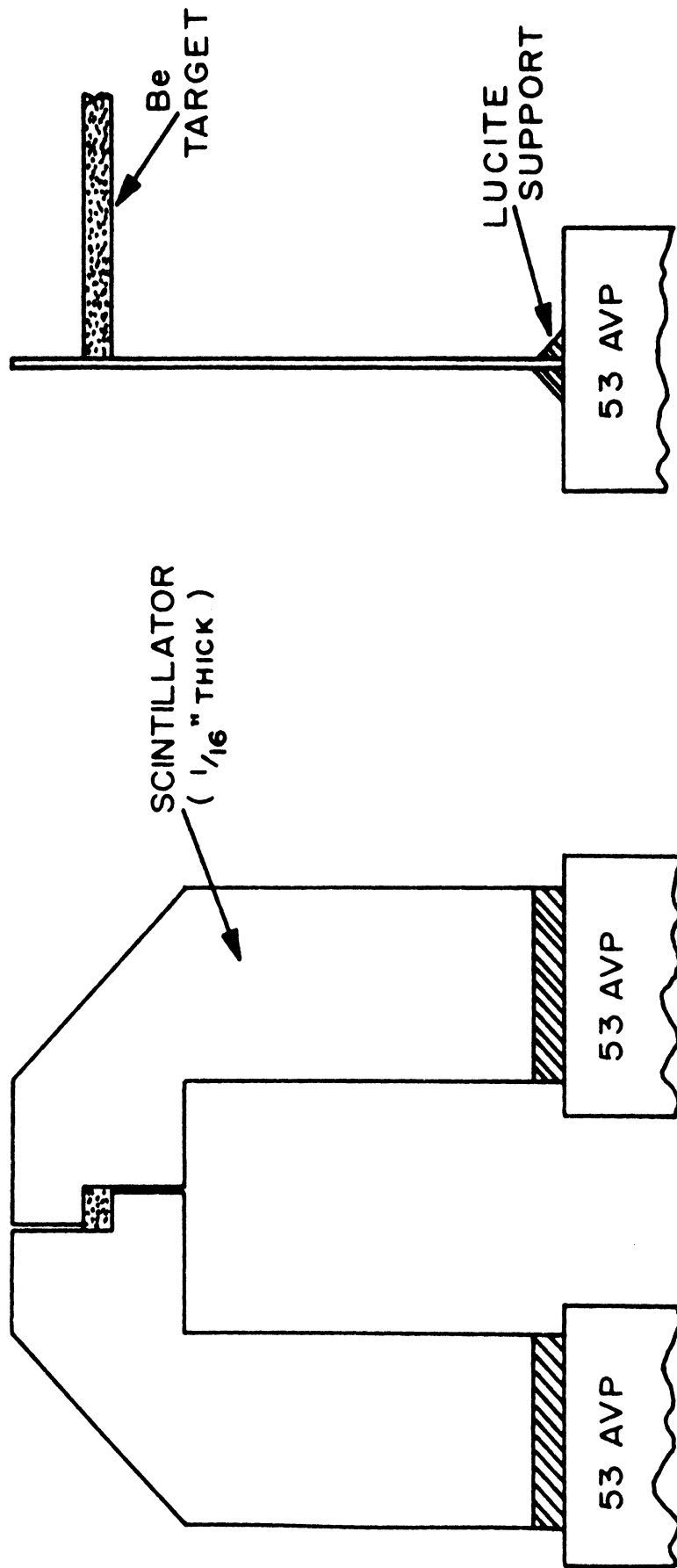
Fig. 5 The Beryllium Target Scintillator Mask

The beryllium target was also viewed by a three-counter telescope, called monitor B, which was placed about 7 feet below and aimed at the target. The telescope B, in conjunction with others to be described later, was used to monitor the intensities of the neutron and the proton beams.

A broad energy spectrum of neutrons was produced at the beryllium target. In addition, unwanted particles were produced copiously. The charged contaminants were removed by the large bending manget, M4D, which immediately followed the beryllium. M4D had a field gap that was 84 inches long, 15 inches wide, and 4 inches high. Nominally run at 1000 amperes (14 kilogauss at midfield), M4D deflected the proton beam away from the neutron collimator and into the shielding.

Three pieces of 1/8-inch thick lead were placed in the gap of M4D as shown in Fig. 4 to serve as converters for gammas. Separating the lead allowed an electron-positron pair to be swept aside with less chance of radiating, thereby increasing the efficiency of the converter. M4D was followed by a 9 inch by 12 inch C magnet which further swept the charged pairs from the beam.

The shielding wall was composed of 5 feet of steel followed by 10 feet of "heavy" concrete. The neutron beam was defined by a three-piece collimator imbedded in the wall. The first two sections had inside diameters of 5/8 inch while the final section had an inside diameter

of 1 inch. All sections were 5 feet long. The exit from
the second section, which formed the defining aperture,
was 23 feet from the beryllium target. The inside diameter
of the final section was not directly illuminated by the
beryllium target; it served to reduce beam halo by stopping
many of the particles which underwent small-angle scatter-
ing in the defining collimator. The solid angle subtended
by the collimator was 4×10^{-6} steradians. An angular
spread of about 2 milliradians was expected. A prelim-
inary survey indicated increasing neutron flux for
decreasing angles with respect to the proton beam line;
however, for safety reasons the collimator was aligned at
$1°$ with respect to the proton beam. This was done because
the Radiation Control Group at the Bevatron did not want
a magnet failure to allow the full proton beam into the
experimental area.

The size, spread, and position of the neutron beam
was determined by placing Polaroid 3000 film at the
collimator exit and at the back of the experiment cave.
The Polaroid at the collimator exit was exposed during
some test runs by placing some polyethylene immediately
in front of the Polaroid. Neutrons which scattered in
the polyethylene produced charged particles which exposed
the film. The downstream Polaroid was exposed during
the course of the experiment. It was placed downstream
from the M monitor telescope and from the 3-inch aluminum
block. Thus many charged particles were generated which

could expose the film. Sample Polaroids are shown in Fig. 6 and a plan view of the experiment is shown in Fig. 7. The back of the experimental cave was 184 inches downstream from the collimator exit. At the collimator exit the beam was found to be about 0.9 inch in diameter and very sharply defined. The downstream Polaroid showed the beam size to be about 1.2 inches which gives a full angular spread to the beam of about 2 milliradians as predicted from the collimator dimensions.

An anticounter, A1, was placed at the collimator exit to insure that the beam particles were neutrally charged. The counter was 3 inches on a side and 1/8 inch thick. The anticounter also marked the entrance to the main experimental area as shown in Fig. 7.

B. Liquid Hydrogen Target

The liquid hydrogen target was placed in the beam with its center 1 foot from the collimator exit. The target was 4 inches long and 2 inches in diameter. Figure 8 shows the target assembly. The liquid hydrogen was contained in a Mylar flask with 0.005 inch-thick walls. The flask was wrapped with 10 layers of aluminized Mylar and 10 layers of aluminum foil. Each layer of the wrapping was 0.00025 inch thick. The flask was enclosed by an 8 inch diameter vacuum jacket. The beam entrance port was made of 0.020 inch Mylar, the sides through which scattered neutrons passed were made of 0.040 inch aluminum, and the forward
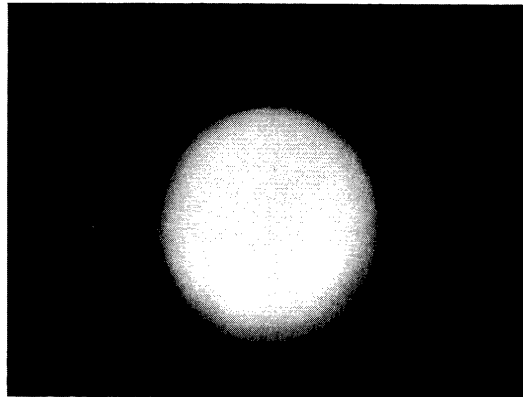
(a)

1 inch
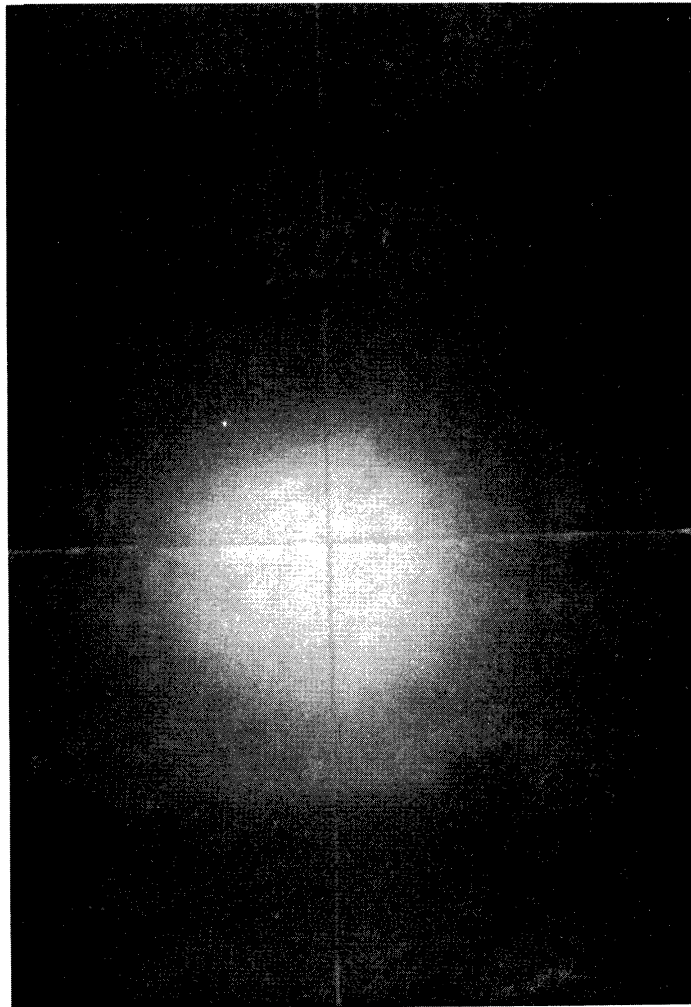
(b)

Fig. 6   Beam Exposures of Polaroids
         (a) Collimator Exit
         (b) Back Wall
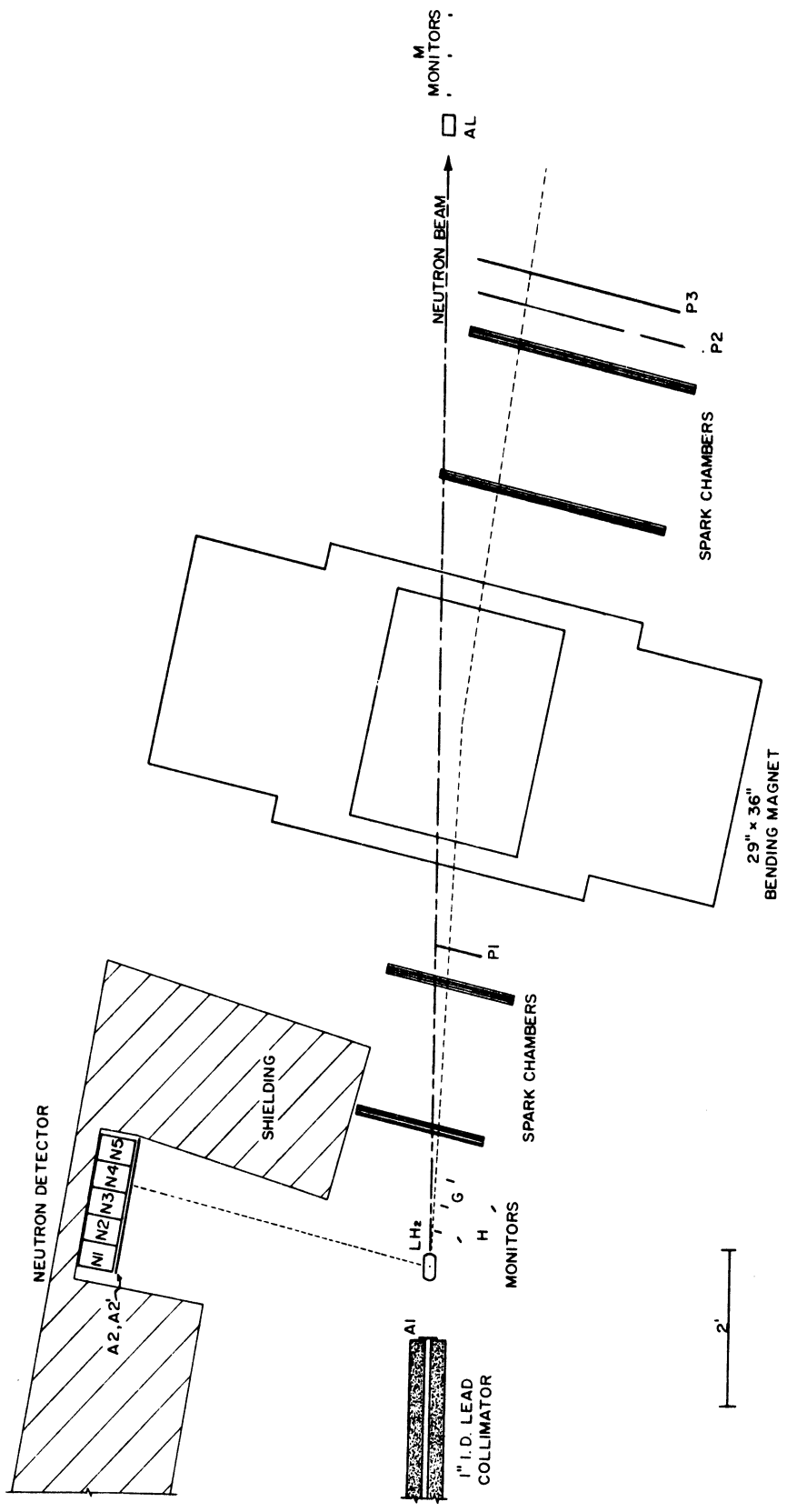
PLAN VIEW OF EXPERIMENT

Fig. 7 A Plan View of the Experiment
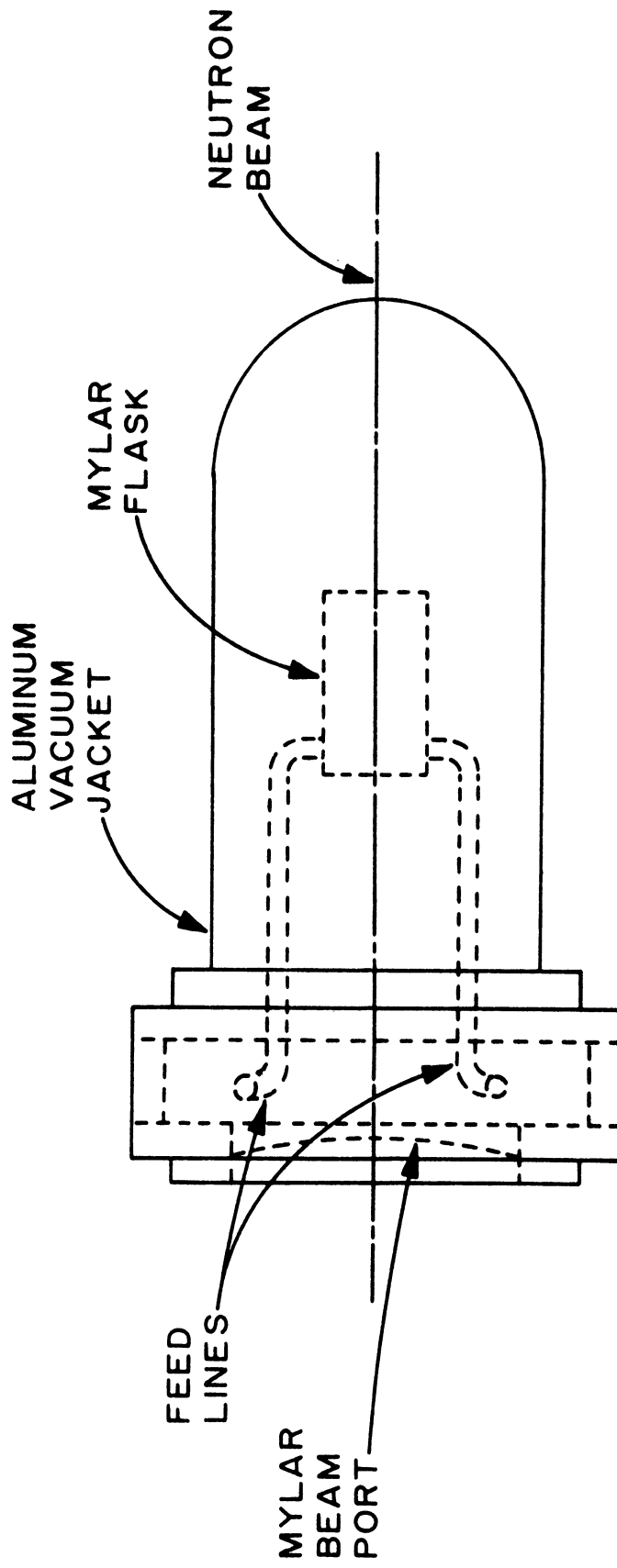
LIQUID HYDROGEN TARGET ASSEMBLY

Fig. 8   The Liquid Hydrogen Target Assembly

exit dome was made of 0.020 inch aluminum. Liquid hydrogen was supplied from a nearby reservoir and allowed to boil off at atmospheric pressure. The flask could be readily emptied to make "target empty" runs.

The liquid hydrogen target was viewed by three monitor telescopes: G, H, and M. The G and M telescopes consisted of three small counters in coincidence, while the H telescope consisted of two counters. The G and H telescopes were about 1 foot from the target and viewed it from below. The M telescope was in the neutron beam line and about 184 inches downstream from the target. A three-inch thick block of aluminum was placed just in front of the M telescope to increase its counting rate and decrease its dependence on the charged beam contaminants which were generated during passage of the neutron beam through the system.

C. Proton Spectrometer

A charge exchange collision in the target volume resulted in a neutron with kinetic energy from 1 to 250 MeV coming off at nearly $90°$ in the lab, while the proton moved forward with nearly all of the energy of the incident particle. Two thin-foil spark chambers immediately following the target gave the proton recoil angle and established its direction as it entered the momentum analyzing magnet. Two more thin-foil chambers after the magnet provided the remaining parameters needed for the

momentum determination. Scintillation counters P_1, P_2, and P_3 indicated the passage of a charged particle through the system. The slow neutron was detected in an array of thick scintillation counters.

The front spark chambers had an active area of 22 inches in the horizontal direction by 6 inches in the vertical direction; while the corresponding dimensions for the back chambers were 39 inches by 11 inches. Each chamber had four active 3/8-inch gaps. The plate material was 0.001 inch aluminum foil. The frames were made of Plexiglas. In general, it is desirable to have the Plexiglas as thin as possible in order to minimize displacement of the track images due to misalignment of the frames. For this reason the frames on the short sides (through which one viewed the length of the chambers) were made 3/4 inch thick; however, the long frames at the top and the bottom of the chambers were made 1.5 inches thick in order to provide extra strength. Mylar windows which were 0.005 inch thick were glued to an extra frame which, in turn, was connected to the spark chamber proper by a Mylar diaphragm, or hinge as we labeled it, which went all the way around the frames. A cross sectional view of the hinge is given in Fig. 9. The chambers were filled with a 90% neon-10% helium mixture at a pressure slightly greater than atmospheric. The excess pressure ballooned the Mylar windows outward. The hinges isolated the foil plates from the stresses due to the ballooning so that the foils did not wrinkle.
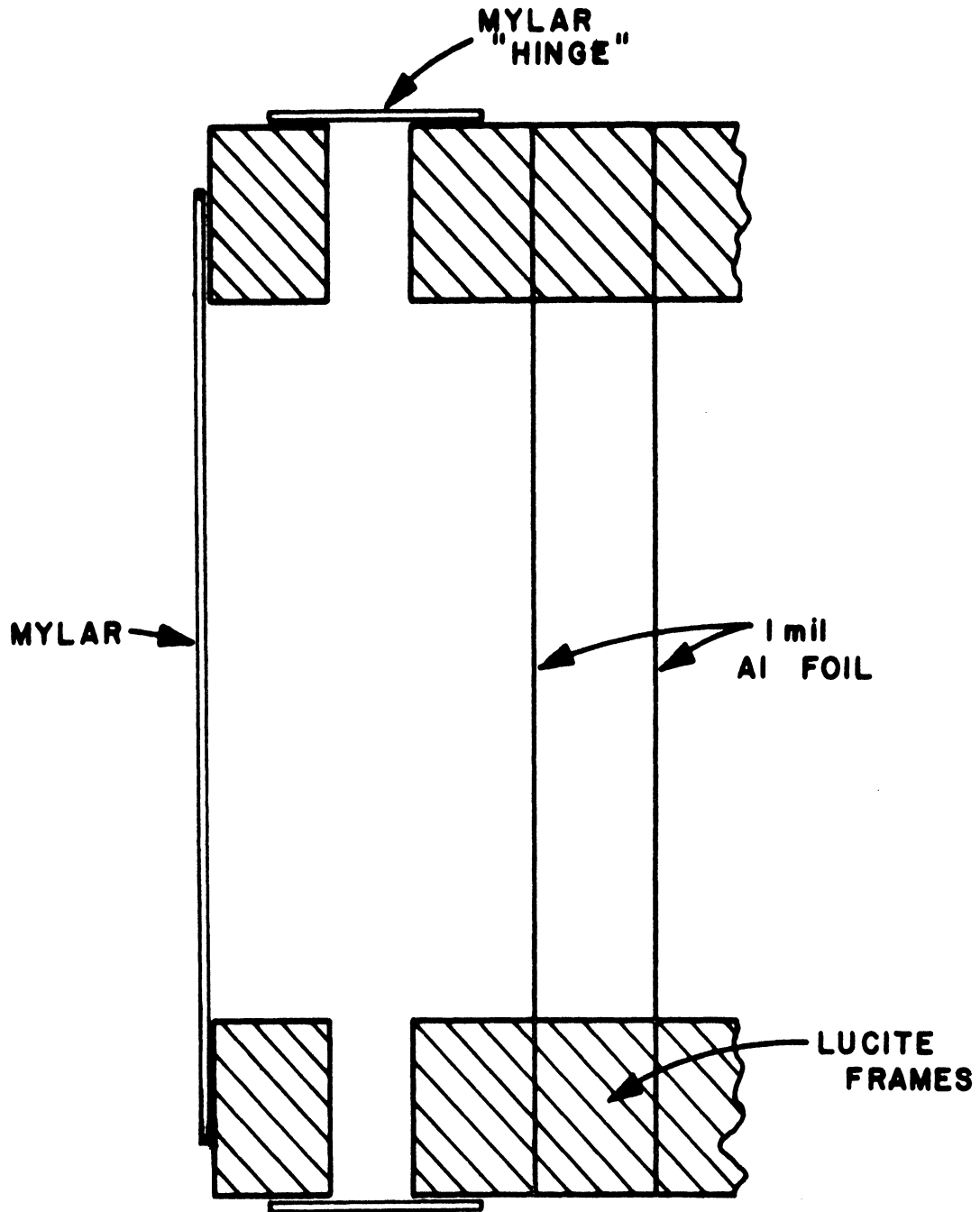
Fig. 9   The Hinge Construction of the Spark Chambers

The chambers were constructed in a $48°$ F environment and were operated at about $70°$ F. Plexiglas has a larger coefficient of expansion than does aluminum. Therefore, the aluminum foil was stretched taut when the chambers were warmed to operating temperatures. The aluminum foil was glued to the frames with Silastic RTV 891.[33]

Three counters in triple coincidence were used to detect the passage of a proton through the system. The first of these, P1, was placed between the front pair of chambers and the magnet. Because of its proximity to the magnet the photomultiplier for this counter was protected by a 3/8-inch thick steel tube in addition to the standard mu-metal shield. Counter P1 was 1/8 inch thick and 8 inches long. It was tapered from 1.75 inches near the beam to 3.6 inches at the light pipe. Counters P2 and P3 were placed immediately downstream from the last spark chamber. Both counters were 1/2 inch thick. P2 was 9-1/8 inches high and 39 inches long, while in an effort to cut down on accidentals, P3 was made 35 inches long and tapered. It was 2.5 inches high at the beam end and 11.5 inches high at the light pipe.

Note that the neutron beam traversed the proton spectrometer. Therefore, special precautions had to be taken in order to minimize the material in the beam's path and, consequently, in order to minimize the accidental rate. Counter P1, for instance, was made thinner

than the other counters in the system. Further, counters
P1 and P3 were shaped to give a coplanarity restriction
in the trigger.

The analyzing magnet, Bev II, had an 8.25-inch gap
with pole tips which were 36 inches long and 29 inches
wide. The Lawrence Radiation Laboratory Magnet Test Group
produced a series of maps of the vertical component of the
magnetic fields.[34] In particular, maps were obtained for
each of six currents (392,588,855,960,1084, and 1203
amperes). A map consisted of 7 elevations (0., ±2., ±2.8,
and ±3. inches about the gap midplane). At each elevation
there were 2800 measurements distributed over an inch grid.
The field was measured at each point to ±0.2%. For the
charge exchange experiment the magnet was operated at 523
amperes which provided a nominal field integral of 4.77×10^5
gauss-inches. The current was monitored using a 33 micro-ohm
shunt and a potentiometer. A 2 GeV/c particle was bent
about 10 degrees and a 7 GeV/c particle was bent about
3 degrees.

D. <u>Optics</u>

Front-surface mirrors were used to view all chambers.
Figure 10 shows the placement of the mirrors and the complex
foldings of the light path required to reduce the images to
a single 35 mm frame and to equalize the optical path lengths
from all chambers to about 400 inches. Two views of each
chamber, a "direct" view and a "stereo" view, were obtained.

MIRROR FOLDINGS
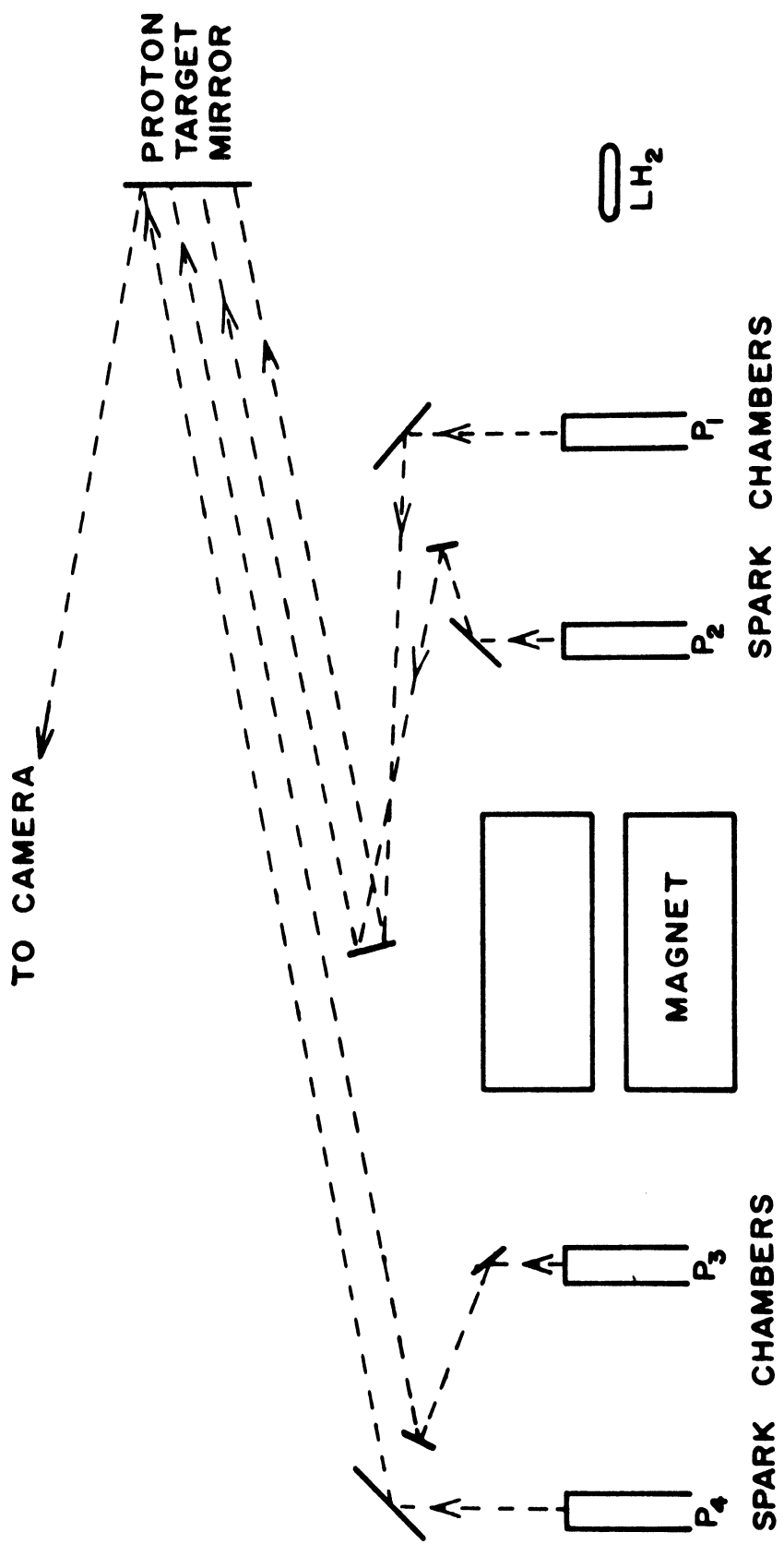
Fig. 10 The Mirror Foldings

Each view of each spark chamber was delimited by fiducials which were made by masking plastic electro-luminescent panels[35] with a machined aluminum plate. The panels were driven by a 500 volt, 5 khz square wave of 10 msec duration.[36] In addition to the fiducials described above, "see-through" fiducials were provided for each view. These fiducials, powered with ordinary 110 volt ac, were turned on for a few frames at the beginning of each roll. Because they were viewed through the entire chamber and the Plexiglas frames, the "see-through" fiducials aided in mirror alignment and were particularly useful in later analysis.

The camera also viewed a supplementary information bank which contained several important elements. First of these was a pair of large fiducials designed primarily to aid in automatically scanning the film. There was also a mechanical decimal frame counter and a neon flash-lamp binary frame counter. Neon lights also indicated which neutron counter fired for that event.

The camera used was a fast, pulsed camera which could take up to 5 pictures during the 300 msec beam spill.[37] A 240 mm lens was used at an f/8 aperture. The demagnification was about forty.

E. Neutron Detector

In contrast to the high energies of the recoil protons, the scattered neutrons had energies in the MeV range,

that is, from 1 MeV to 250 MeV. Because of these very
different energies and because of the neutral charge of the
neutron, very different techniques were employed for the
detection of the neutrons. The heart of the system was an
array of five thick scintillation counters. In order to be
detected a neutron had to scatter in the scintillator and
transfer enough energy to a charged particle (or particles)
that it might produce sufficient light.

Each plastic scintillator was 4 inches wide, 6 inches
thick, and 12 inches high. The light pipes were mounted on
the tops of the counters as shown in Fig. 11. The front
face of the array was about 53 inches from the center of the
hydrogen target, and a line drawn from the center of the
array to the center of the target made an angle of 80.1
degrees with respect to the beam line. Thus the array
extended beyond the 90 degree limit for neutrons and down to
angles of about 67 degrees. Kinematics restricted inelastic
neutrons to counters 4 and 5 (those nearest 67 degrees).
However, gammas which resulted from π° decay could count in
all of the counters.

The photomultipliers used were RCA 6810A's. They were
operated at approximately -2100 volts. The threshold for
neutron detection, that is, the discriminator levels and the
tube voltages for each counter, was set by using a 49 micro-
curie Tl^{204} source. The discriminators were set to a thres-
hold of 0.5 volt. In order to set the tube voltage for a
counter the thallium source was centrally attached to the

NEUTRON COUNTER

UVT Lucite Light Pipe

Scintillator

12"

4"

5 $\frac{7}{8}$"
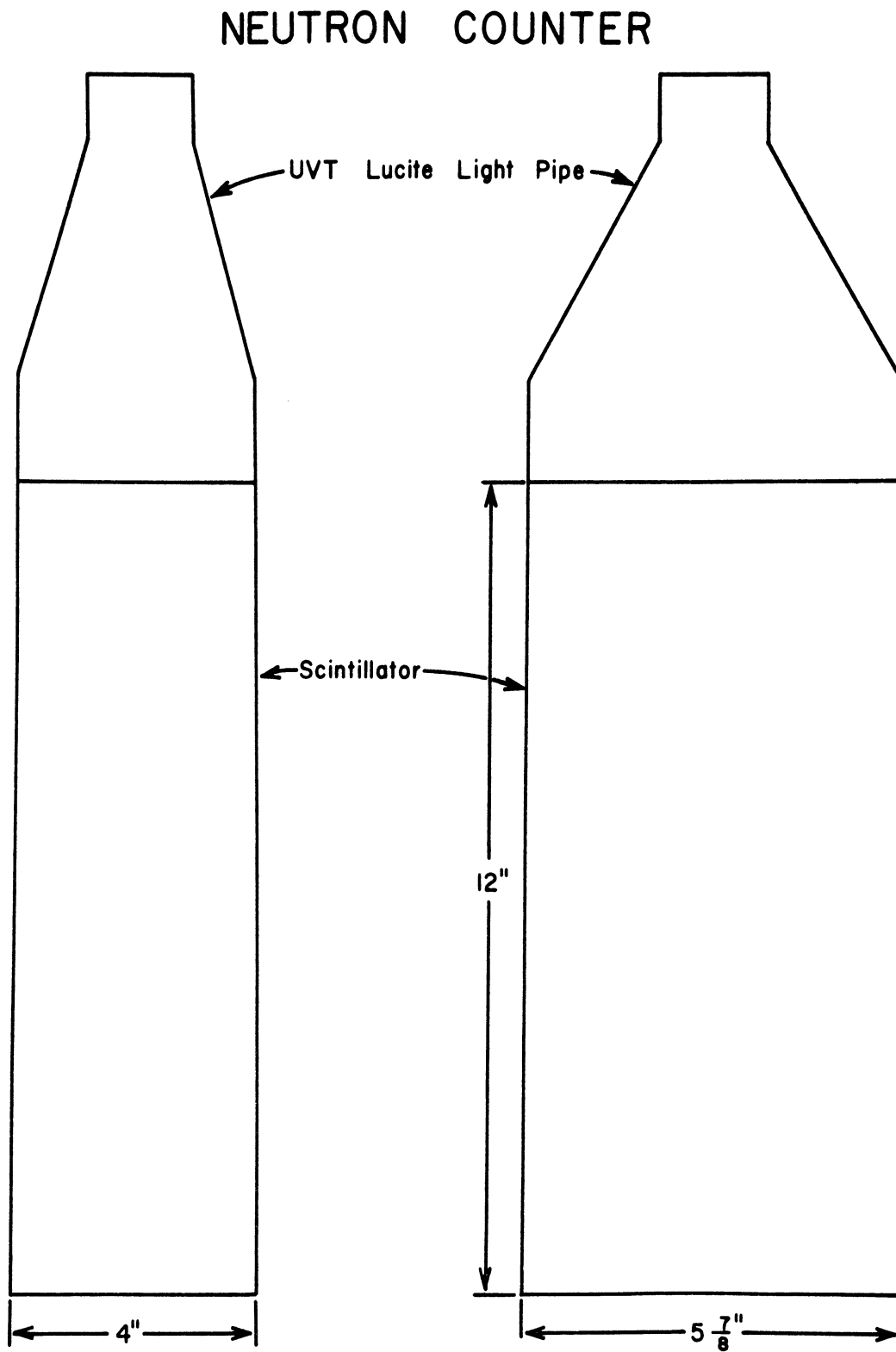
Fig. 11 A Diagram of a Neutron Counter

counter at which spot the light-tight wrapping was held to a minimum. The tube voltage was adjusted until the system counted 5000 triggers per second. This trigger rate was far above noise levels and at the same time, was far below the thallium decay rate. Thus we felt we were counting only the upper portion of the beta energy spectrum. In other words we set the threshold for each counter to detect 0.76 MeV betas, which was the maximum energy of the betas produced by the thallium. Because of saturation effects in the scintillator the 0.76 MeV betas simulated 2 MeV protons. The threshold settings were frequently checked by the same procedure.

As noted above, information denoting the counter or counters which detected a neutron was displayed in the main experimental area and photographed along with the spark chamber tracks for each event. In addition, timing signals were displayed on a Tektronix 517 oscilloscope and photographed with a separate camera.

Two anticounters, A2 and A2', were used to insure that the particle entering the neutron counters (or their light pipes) was neutral. Counter A2 was 13 inches high, 21 inches long, and 1/2 inch thick. Counter A2', which shielded the neutron counters' light pipes, was also 21 inches long, but was only 6 inches high and 3/8 inch thick. The light pipes for A2 and A2' were placed as far as possible from the neutron beam in order to minimize the number of particles which scattered into them.

The neutron counters were shielded from the accelerator background and from particles scattered out of the neutron beam by an arrangement of paraffin, boron, and lead which surrounded the counters on the top and bottom and all sides save that facing the target. Boxed paraffin formed the bulk of and outer perimeter of the shielding. Three-inch borax bricks served as the second ring of defense. Boron has a high cross section for thermal neutrons and gives off a low energy gamma. Three-inch lead bricks formed the innermost ring of shielding.

F. Electronics

The fast electronics logic is shown in block form in Fig. 12. The 100 megahertz circuitry was composed, in the main, of commercially available modules from General Applied Science Laboratories.

At the start of the beam spill the circuitry was gated on by a timing pulse from the accelerator. The neutral charge of the beam was assured by the anticounter Al. Counters P1, P2, and P3 recorded the passage of a charged particle through the proton spectrometer. A null signal from anticounters A2 and A2' plus a signal from any one of or any combination of the neutron counters indicated the presence of an associated neutral particle. An event trigger, then, was defined as

$$\overline{A1}\ P1\ P2\ P3\ \overline{A2}\ \overline{A2'}\ N_i \qquad (i=1,\ldots,5).$$
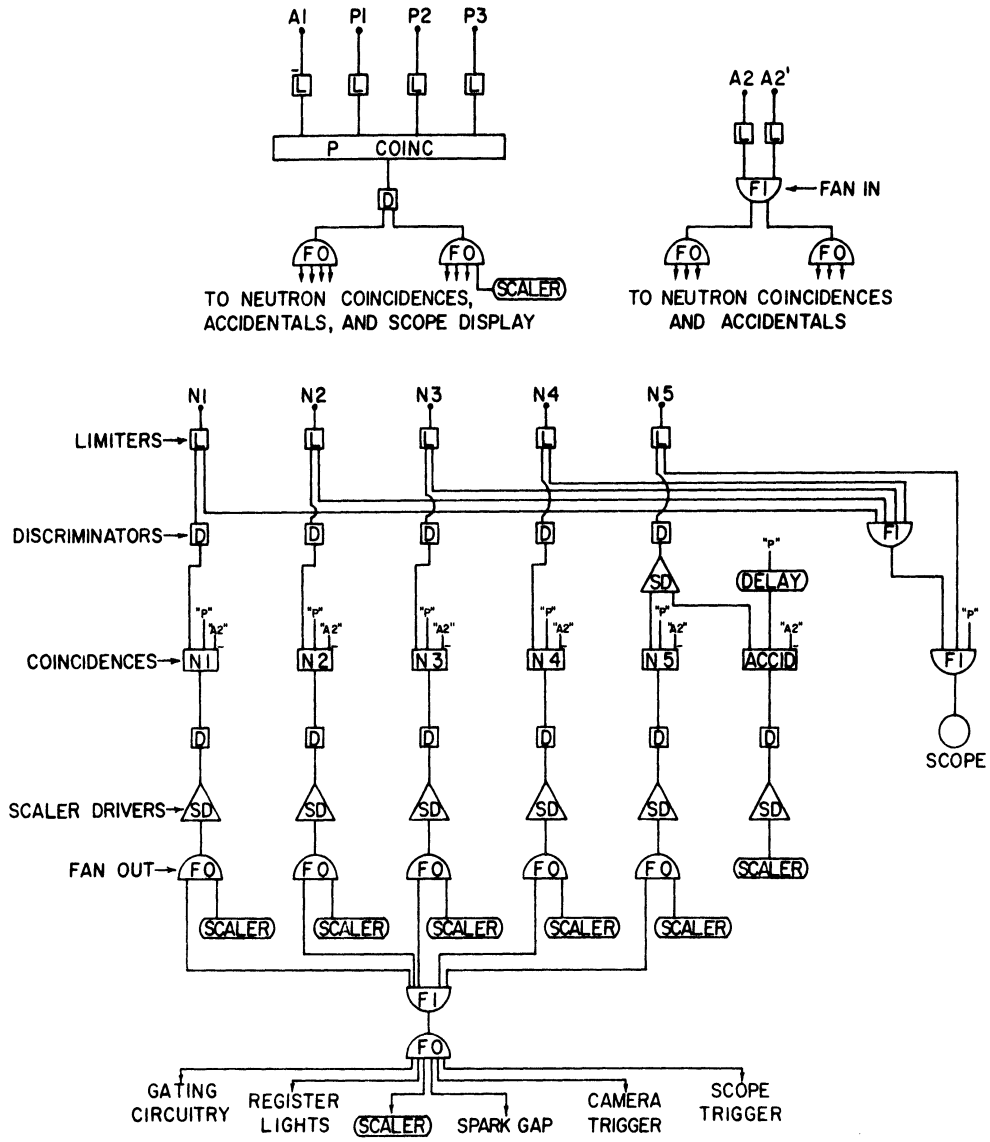
BLOCK DIAGRAM OF ELECTRONIC LOGIC

Fig. 12 A Block Diagram of the Electronic Logic

A sub-coincidence, here called the P-coincidence, was formed by placing the proton spectrometer counters, P1, P2, and P3, in coincidence; and by placing the counter at the collimator exit, A1, in anticoincidence. The P-coincidence signal was split for use in other logic units. The P-coincidence signals, with the proper delays, were fed into a coincidence module for each of the five neutron counters along with the signal from the appropriate neutron counter. The signals from the two counters, A2 and A2', in front of the neutron detecter array were combined and placed in anticoincidence with each neutron counter. The coincidence widths were separately set for each neutron counter. They were calculated to be wide enough for each counter to accept all of the charge exchange events which could physically reach that counter with energies above threshold. The outputs of the five N coincidences defined above were added so that a signal from any one (or any combination of counters) defined an event.

Once an event had been defined the signal was split to initiate several actions. The first of these was to gate off all coincidences including the beam monitors for 60 msec to allow time to record the event, advance the camera, etc. before the advent of a new event. During that time interval a spark gap was triggered to pulse the spark chambers. The fiducials were flashed, as were the frame and pulse counters and the neutron counter display. Then

the film in the fast camera was advanced.

In the meantime, the 517 oscilloscope trace was also triggered so that the timing information might be recorded. If the event were the first of the several that might be detected during a beam pulse, a delay gate was triggered. The delay gate triggered a push-pull amplifier that was connected to the vertical deflection plates of the oscilloscope. This had the effect that the timing information for the first event of a beam pulse was recorded at the top of the film; while subsequent events had their timing information displaced downward on the same frame. The reason for placing on a single frame the timing information for all events which occured during a beam spill was that the oscilloscope camera had a slow advance mechanism. After about 1/2 second delay, that is, after the 300 msec beam spill was surely over, the delay gate reset the push-pull amplifier, advanced the film in the oscilloscope camera, and flashed the binary frame counter for the next beam pulse. The timing information consisted of signals from the P-coincidence and from each of the neutron counters.

Scalers recorded the number of events, as well as the P- and N-coincidence counts, and the counts from the monitor telescopes B, G, H, and M. Accidentals rates were also recorded. The accidentals rate was monitored by forming two coincidences with neutron counter 5. One coincidence had the proper delays while the other, N_{acc},

had the P-coincidence signal delayed an extra 100 nano-
seconds.

The lengths of the various timing delay cables were
set by using a system of corona lamps.[38] A lamp was
centrally attached to each scintillator required to define
an event. All lamps were driven by a common source, but
calculated relative delays were inserted to simulate the
time sequence of a real event. The photomultiplier outputs
were viewed on an oscilloscope and delays were inserted in
the fast logic to properly align the signals forming each
coincidence. The light pulsers were also used to frequently
monitor the performance of the electronics.

G. Data Collection

Approximately $5-7 \times 10^{10}$ protons struck the beryllium
target during each 300 msec beam spill. Two to three
pictures were taken during each beam spill for a total
of about 66000 pictures with liquid hydrogen in the target.
Periodically the target was emptied and a "target empty"
run was made. Over 7500 pictures were taken in this mode.
The "target empty" trigger rate was about 1/3 of the
"target full" rate.

The Lawrence Radiation Laboratory Photographic
Services Group developed each roll of film within an hour
or two after exposure. A quick check could then be made
of the performance of the spark chambers, the fiducials,

and the other components of the system.

A number of pictures were taken with the magnet turned off. The purpose of these pictures was to establish a straight line through the system. A number of pictures were taken with the B monitor telescope serving as the sole trigger. Presumably these pictures had nothing to do with real events in the target, so these pictures were used to determine the frequency of spurious tracks in the spark chambers.

Periodically the thresholds of the neutron counters were checked and were reset with the thallium beta source. The fast electronics logic was checked by pulsing the corona lamps. The light pulser timing was recorded on the oscilloscope film as an aid to later analysis. A 50 megahertz sine wave was recorded on the same film to provide sweep calibration.

During the run the accidentals counting rate averaged about 15% of the neutron counter N5 rate. Presumably the accidental events did not reconstruct as elastic events and therefore, their only effect was on the data collection rate.

IV. ANALYSIS

A. Spark Chamber Film

A typical frame of the spark chamber film is shown in Fig. 13 and the various elements of the scene are labeled in Fig. 14. The condensing and folding effects of the mirrors make it somewhat difficult to follow the path of the proton except in the stereo views.

The spark chamber film was prescanned to determine which events should be measured. Events were rejected for any of the following reasons.

a) There were no tracks in any one view. About 7% of the frames fell into this category.

b) There were multiple tracks in any one view. About 42% of the frames were rejected for this reason.

c) More than two neutron counters were triggered or two non-adjacent counters were triggered. Approximately 2% of the frames were rejected by this criterion.

d) The proton obviously scattered off the magnet pole tips (as seen in the stereo views), or the sparks were of very poor quality. Only 2% of the frames fell into this category.

A missing track would have introduced large errors in the

43
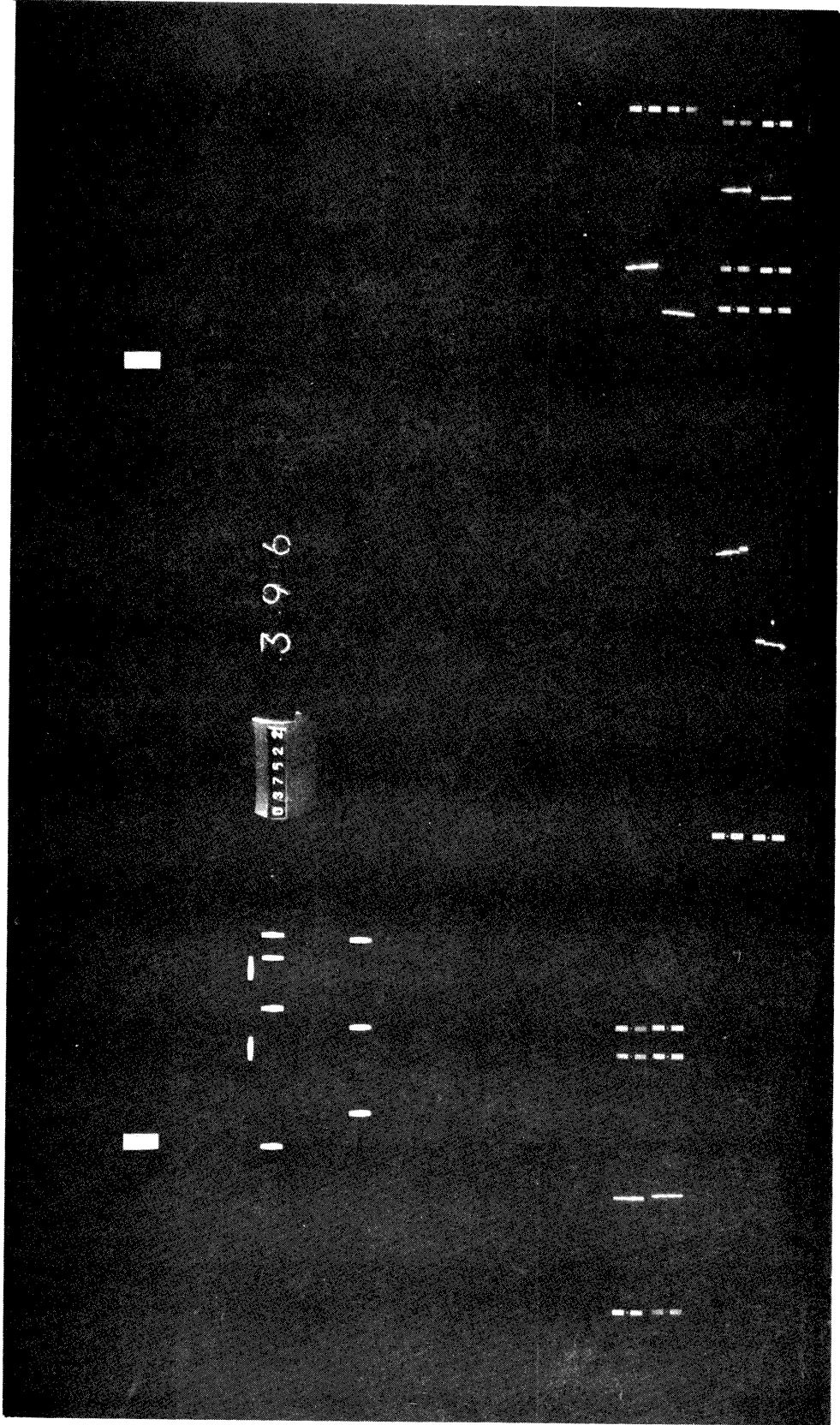
Fig. 13   A Frame of the Spark Chamber Film Showing a Typical Event

Fig. 14 The Legend for Figure 13

solutions for the proton momentum and the scattering angle,
if indeed, solutions would have been possible. Similarly,
criterion c) limited the errors allowed in the scattered
neutron angle and in the timing. A scattering of the proton
in the magnet would have obviously destroyed the credibility
of the event reconstruction.

Approximately 80% of the frames rejected were rejected
due to the presence of extra tracks. Multiple track events
were rejected because of the difficulties in correlating
tracks and because we felt most of these events were
inelastic. This feeling was based on a scan of the film
taken by triggering on the B monitor telescope which looked
at the beryllium target in the proton beam. Since such a
coincidence should have been uncorrelated with events,
elastic or inelastic, which occured in the liquid hydrogen
target, the spark chambers should not have shown tracks. The
paucity of tracks observed in the test run confirmed the
idea that most of the multiple tracks observed in the regular
runs were associated with inelastic processes and were not
random in nature. In any case, no u-dependent biases
should have been introduced by ignoring multiple track
frames. About 22000 frames were measured for further
analysis.

The film was measured on a semiautomatic scanning
machine. The film was placed on a moveable stage and
projected onto a glass viewing screen. The film was
magnified about twenty times. The stage could be moved

to align the point of interest with a cross hair on the viewing screen. Encoders translated the position of the stage into a form which was automatically punched onto IBM cards. The least count of the device was 1.25×10^{-4} inch on the film which was 0.005 inch in event space.

A master fiducial set was measured at the beginning of each roll. Twenty-eight fiducial points were measured several times on a single frame to obtain an excellent master fiducial set. Four widely spaced fiducials were chosen from this set and measured for the other frames of interest on that roll of film. Three of the fiducials were used to solve, via a least-squares technique, for the translation, rotation, and magnification parameters required to fit each frame to the master fiducial set. The fourth fiducial was used to check on measuring errors. Events with excessive measuring errors were discarded.

The point in the middle of each track in each of the eight views was measured. Punched onto cards along with the fiducial and spark locations, were the frame number, the neutron counter (or counters) number which fired, and a code indicating the person performing the measurements. The cards were read onto magnetic tape for computer processing.

Each event was mapped onto the master fiducial set and then the real-space positions of the sparks were determined. Figure 15 is an example of the special fiducial pictures taken at the beginning of each roll of film. It shows the "direct" fiducials which were flashed for
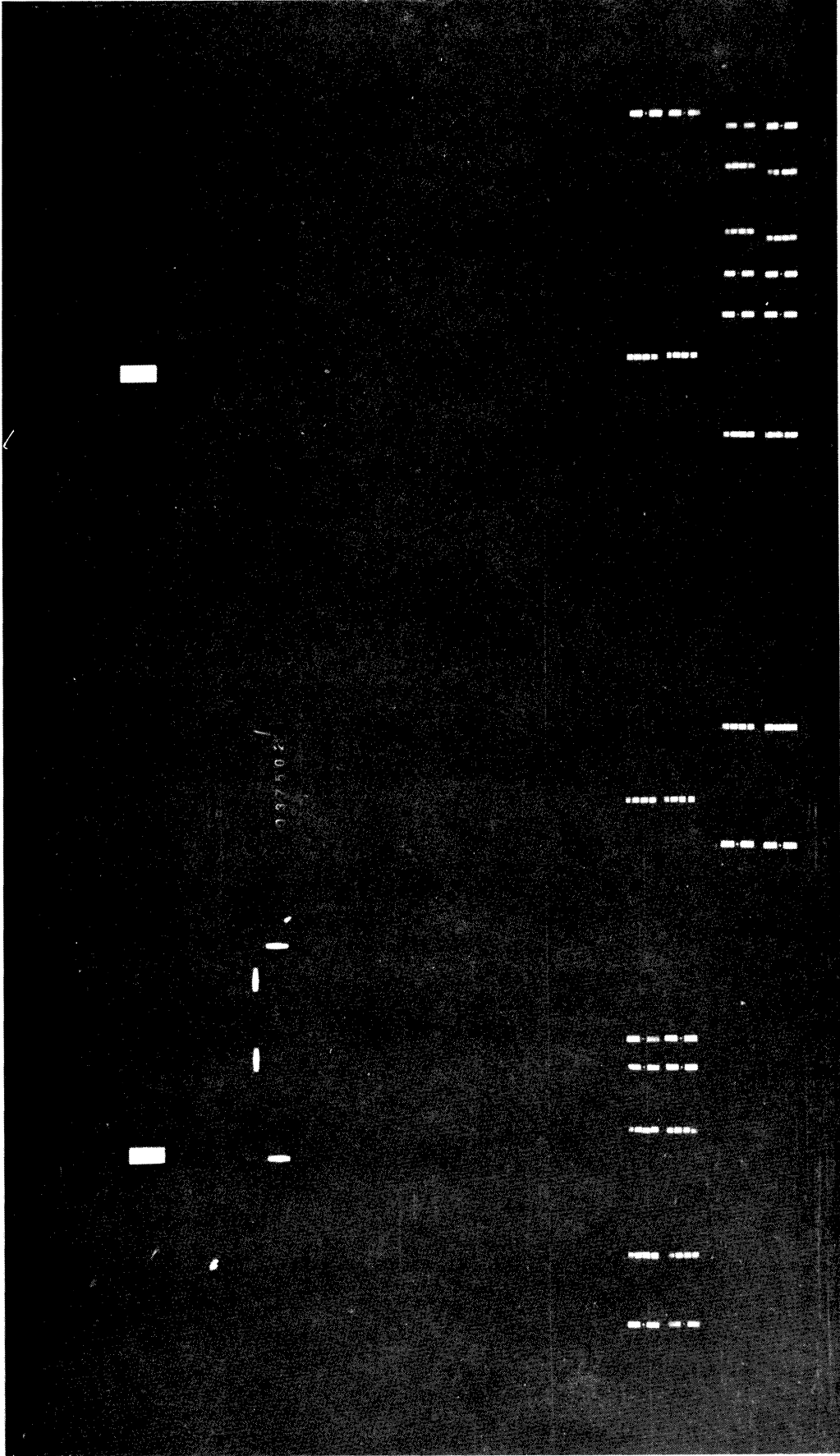
Fig. 15 A Special Fiducial Exposure

every picture taken and the "see-through" fiducials which were illuminated only for the special exposures. By using both sets of fiducials one could determine the position of the optic axis for each view. Figure 16 shows that simple projection revealed the real-space coordinates of the sparks. Corrections were made for the passage of the light through the Plexiglas frames.

Minor adjustments were made in the real-space coordinates of the tracks. The first of these was obtained by projecting small angle tracks from the front chambers to the hydrogen target centerface. We considered only tracks which made a small angle (with tangents ≤ 0.05) with respect to the neutron beam line; thus, the actual interaction point could be disregarded and a good beam profile at the target center-face could be obtained. Slight adjustments (≈ 0.050 inch) had to be made in the solutions for the spark positions in the front chambers in order to center the beam profile in the known beam position. Figure 17 is a scattergram of the adjusted beam profile. The dashed circle outlines the expected beam position. Events were expected at a radius 0.1 inch larger than the beam radius because of the projection angles of the events. However, about 6% of the events fell out of this region and were persumably due to interactions in material other than the hydorgen. The data cuts described in Sect. IV-E reduced the fraction of events which originated outside of the beam area to less than 1%.
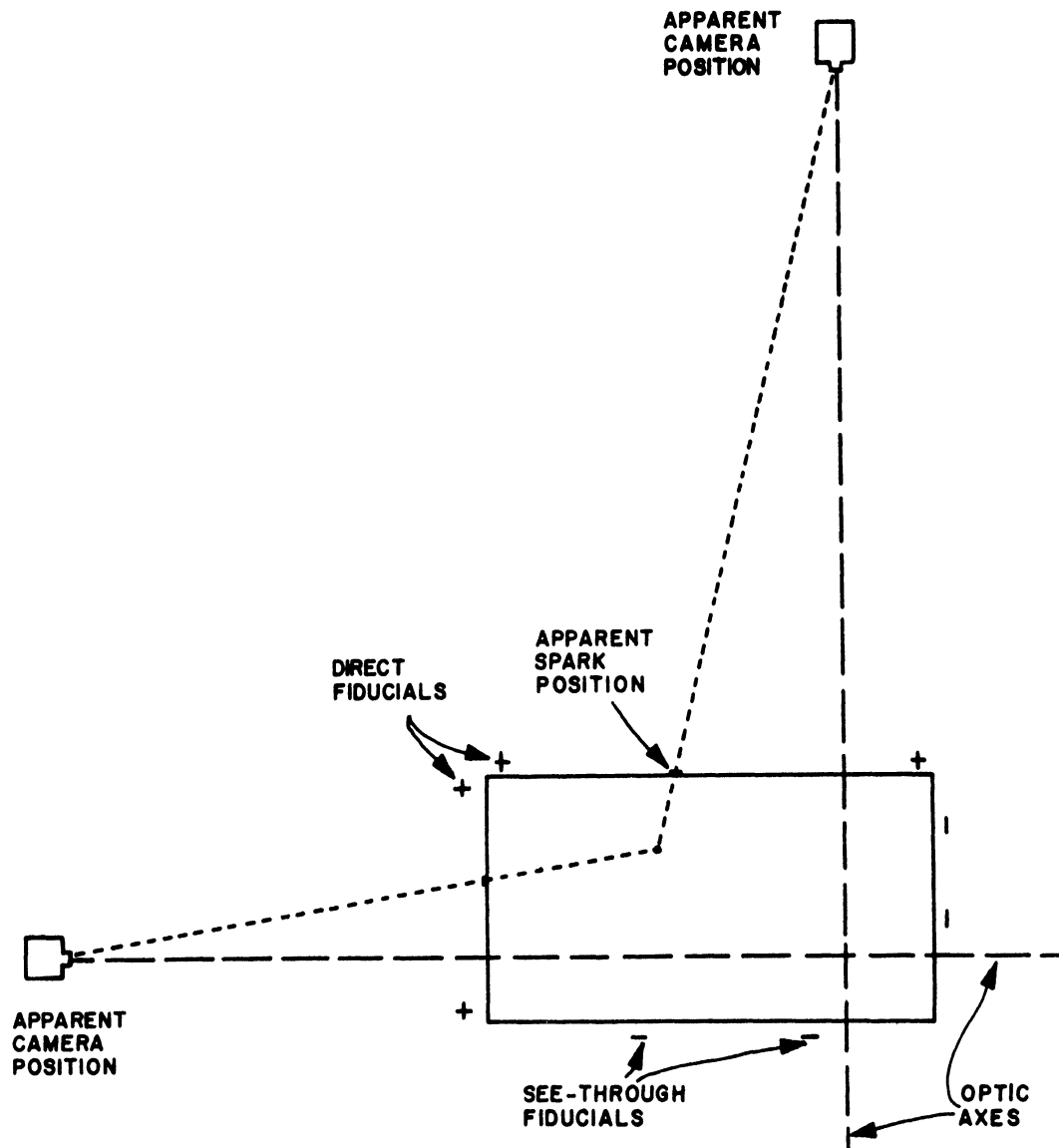
Fig. 16   The Projection Used to Determine the
          Real-Space Position of the Sparks
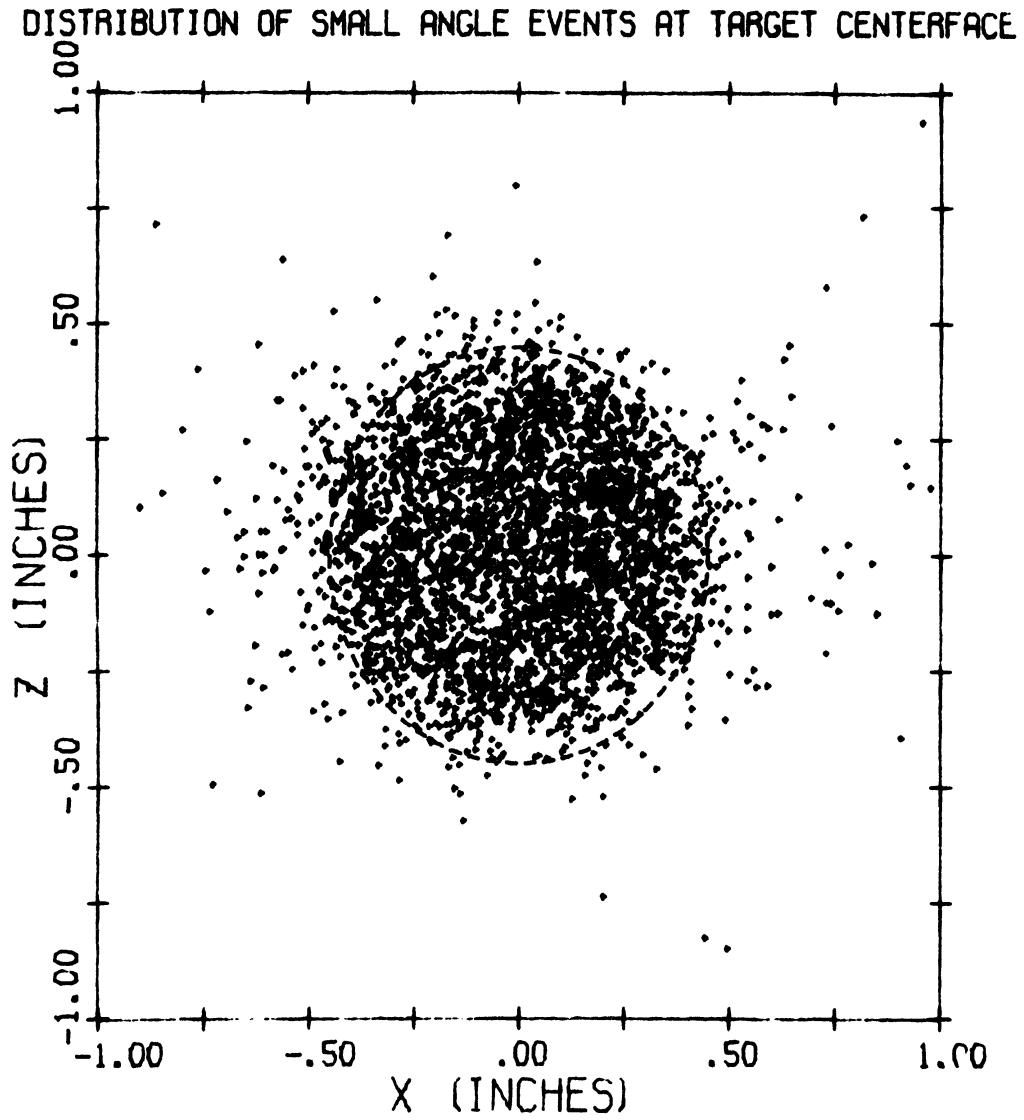
Fig. 17 A Scatterplot of the Neutron Beam Profile at
the Liquid Hydrogen Target Centerface

A second correction involved the relative positions of the front and back spark chambers. A number of pictures were taken with the magnet turned off, thereby producing "straight-throughs". These tracks defined a set of straight lines through the system. These pictures were measured and the real-space track coordinates were determined in the usual manner. Then the tracks in the front two chambers were connected by a straight line which was extended into the regions of the back chambers. The positions of the sparks in the back chambers were compared to the position of the extended line. Figure 18 shows the horizontal component of the error in the third chamber. The positions of the sparks in the back chambers were adjusted accordingly. The cause of the large shift was unknown, but after the adjustment no significant error in the measured angles is thought to occur. One of the reasons for thinking that no significant track positioning errors remained, was that the distribution of the differences between the calculated and measured times-of-flight for the neutrons which triggered counter N1 was centered at zero. The calculated time-of-flight was a function of the proton scattering angle and the proton momentum. An investigation of the width of the peak in Fig. 18 indicates the measurement errors in each spark chamber were slightly less than 0.030 inch in the horizontal plane. Similar errors were made in the vertical plane measurements.

Figure 19 is a scattergram of tracks projected from

PROJECTED MINUS MEASURED X P3
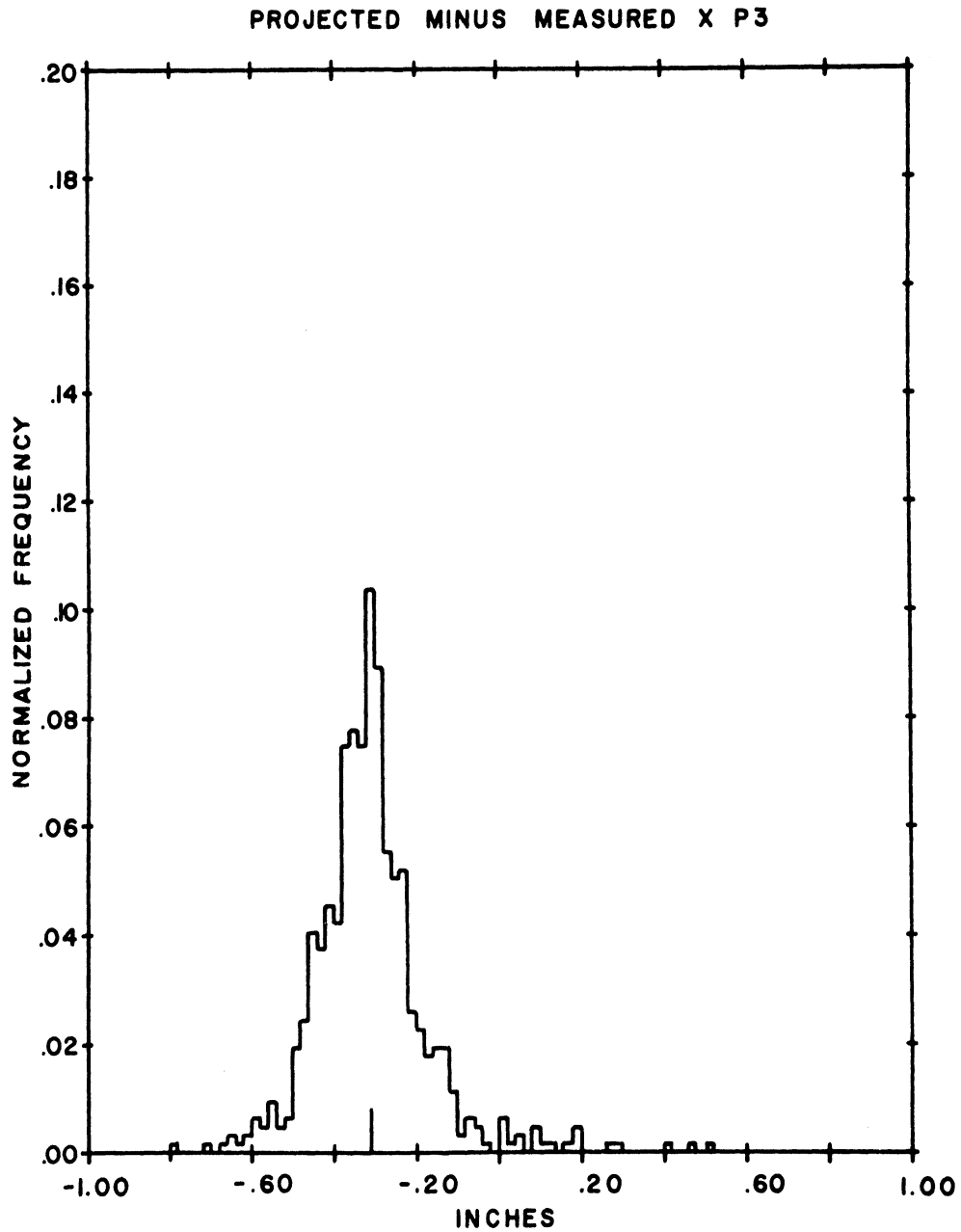
Fig. 18 The Difference between the Projected and
the Measured Spark Positions in the Third
Spark Chamber
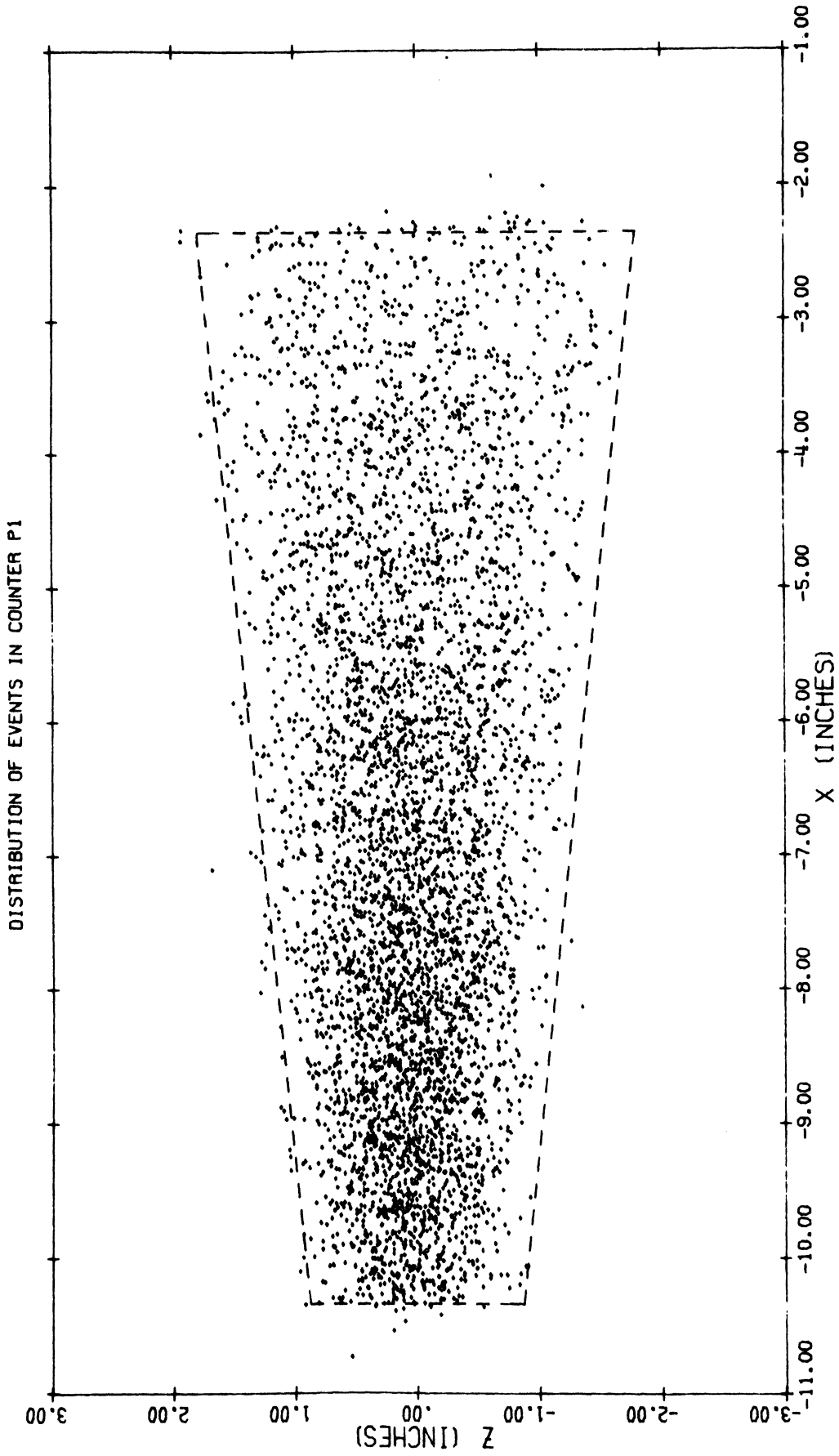
Fig. 19 A Scatterplot of Events in Counter P1

the front two spark chambers into counter P1. The outline
of the counter is shown by the dashed line. The counter was
designed to be slightly oversize. Such scattergrams serve
as good checks on the measurements and corrections used.

B. Timing Film

Figure 20 shows a picture of the oscilloscope screen
which displayed the timing information. In fact, the top
trace belongs to the event for which the spark chamber film
is shown in Fig. 13. The other traces correspond to events
which occured later during the same beam pulse. They were
displaced downward with the push-pull arrangement described
in the section on electronics. The neutron pulses are the
smaller pulses which occur to the left of the frame, and the
proton pulses are the larger pulses near the right-hand side.
Because of the manner in which the oscilloscope was triggered,
faster neutrons produce longer distances between the neutron-
proton pulses. The blobs at the base of the picture are
the binary lights.

All of the measurements were made by projecting the film
onto a glass screen. A special centimeter rule was aligned
with the trace base line and the measurements were made from
the leading edge of the neutron pulse to the leading edge of
the proton pulse at about 2/3 the height of the pulses.
(The velocities of the protons were essentially the velocity
of light. Therefore, the measured timing was directly
related to the neutron time-of-flight.) The measuring
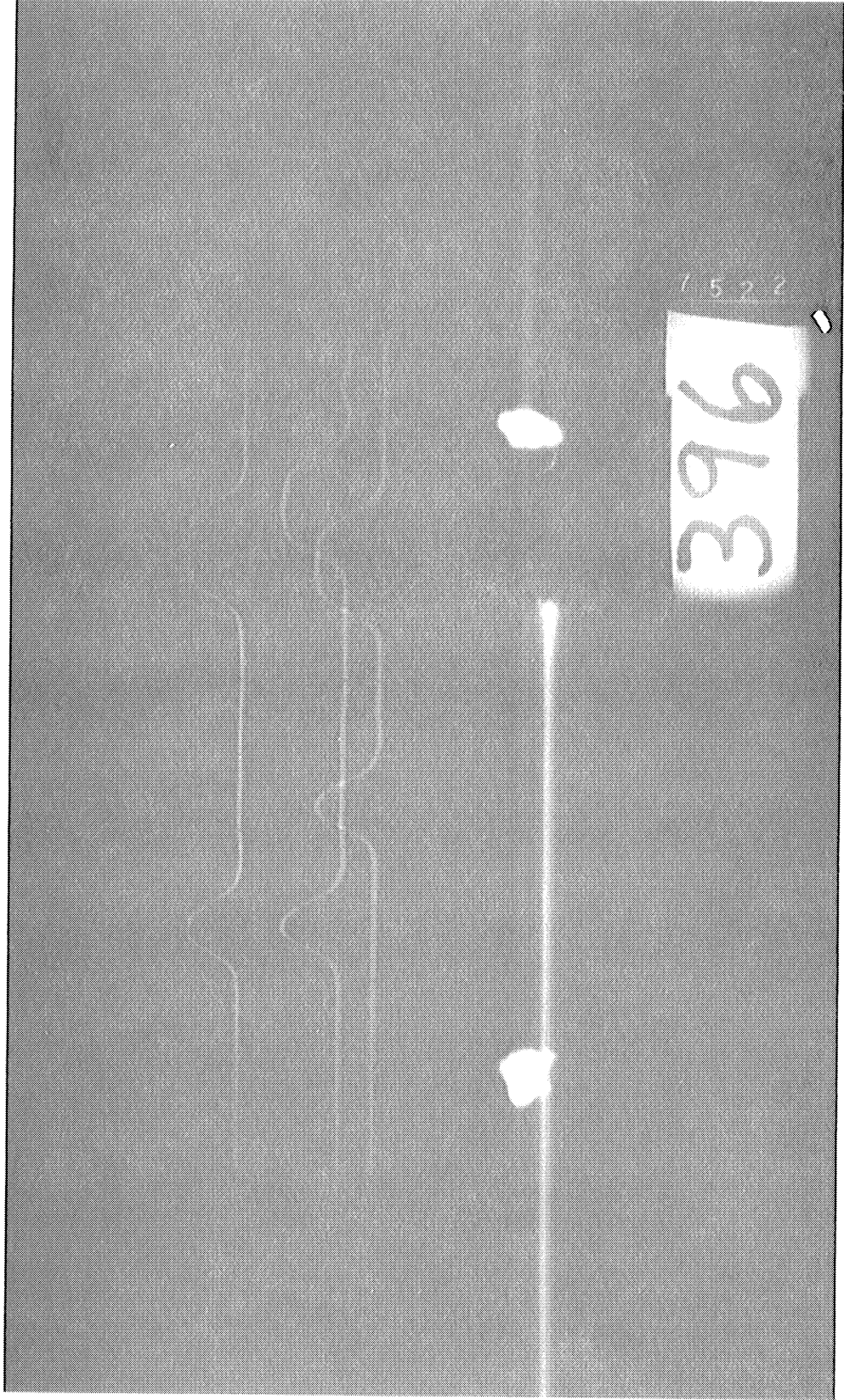
Fig. 20 A Frame of the Timing Film

system was calibrated and the uniformity of the sweep rate
was checked by similarly measuring the signal from a 50 mHz
sine wave generator. The sweep rate was found to be uniform.
The distance-to-time conversion factor was found to be 5.01
nanoseconds per centimeter. The errors on the distance
measurement resulted in errors of about ±3 nsec in the
timing. An additional error of perhaps ±4 nsec was intro-
duced because the N signal came from a discriminator rather
than directly from the photomultiplier. Large pulses from
the photomultiplier would appear to arrive at the discrimin-
ator earlier than small pulses.

Each neutron counter was exposed to neutrons with a large
range of energies. Light pulsers were attached to each
counter and were timed to simulate events with energies
corresponding to the middle of the energy acceptance of each
counter. Timing pictures were made of the signals generated
by the light pulsers as shown in Fig. 21. From the left,
counter N5 is represented by the first pulse, and so on to
counter N1, and finally at the far right is the broad pulse
from the P-coincidence. The light pulser timing was measured
for each counter. Since the light pulser delays were arranged
to simulate events in the middle of the timing range for each
neutron counter, it was possible to calculate a real time-of-
flight and associate it with the proper light pulser. The
target to counter time-of-flight for an event was then
calculated by using the following formula.

$$T = (T_{central} + T_{pulser})_i - T_{scope} \qquad (10)$$
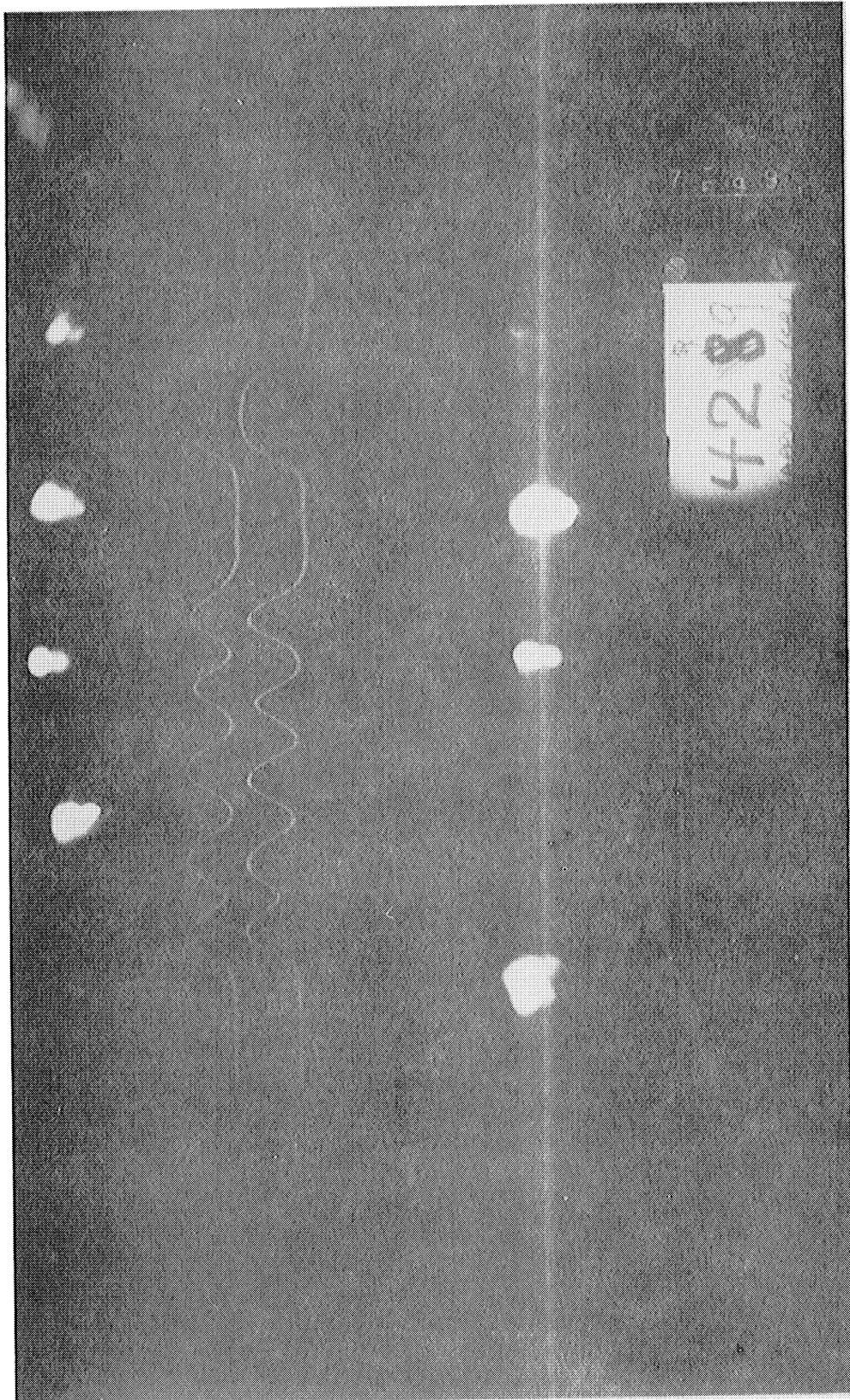
Fig. 21 A Light Pulser Exposure of the Timing Film

$T_{central}$ is the time-of-flight associated with the light
pulser. T_{pulser} is the light pulser timing as measured from
the oscilloscope trace. The subscript, i, indicates which
neutron counter fired. T_{scope} is the timing measured for
the particular event under consideration.

The proton scattering angle and momentum completely
determined the kinematics of the scattering if one assumed
that the scattering were n-p elastic. Therefore, the time-
of-flight of the neutron could also be calculated and
compared to the measured value. Distributions of the differ-
ences between measured and calculated times-of-flight were
plotted for each neutron counter. In some cases the distri-
butions did not center on zero so small empirical corrections
were made to the above formula. These corrections varied from
-4 to +1 nsec. Figure 22 shows these difference distributions
for each of the neutron counters after the corrections have
been made. Figure 23 shows the measured time-of-flight
distributions for the counters. In the difference plots a
neutron which was faster than calculated would give a positive
point on the graph. In Fig. 23 photons should give a peak
centered at 5 nsec. This can be seen clearly in the distri-
butions for counters 2 and 3. Photons were timed out for
counter 1, and the photon peak merges with the neutrons for
counters 4 and 5.

C. Proton Momentum Determination

The momentum of the proton was determined through the
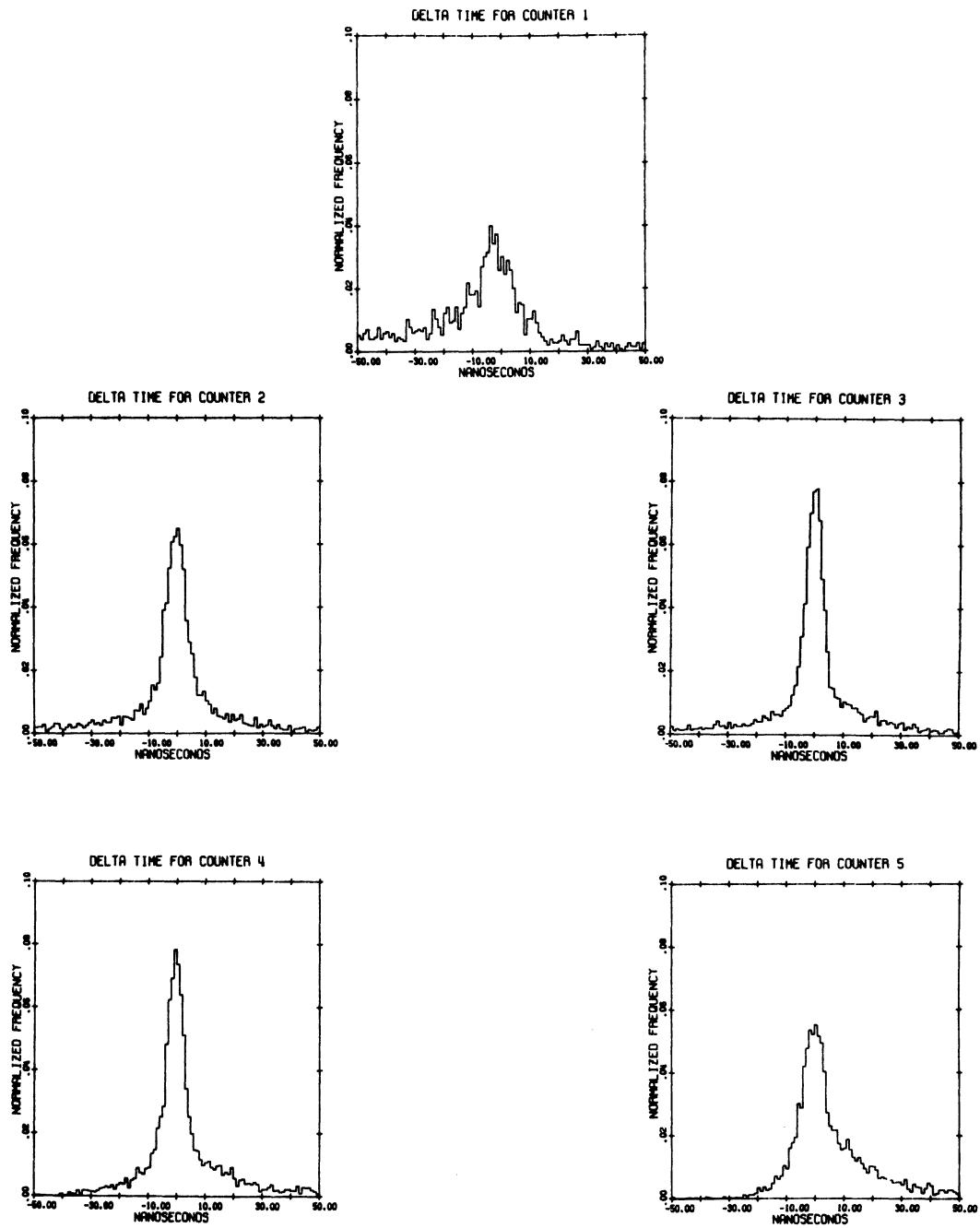
Fig. 22   The Difference between the Measured and the
           Calculated Timing as a Function of Neutron
           Counter

TIME-OF-FLIGHT DISTRIBUTION FOR COUNTER 1

TIME-OF-FLIGHT DISTRIBUTION FOR COUNTER 2

TIME-OF-FLIGHT DISTRIBUTION FOR COUNTER 3

TIME-OF-FLIGHT DISTRIBUTION FOR COUNTER 4

TIME-OF-FLIGHT DISTRIBUTION FOR COUNTER 5
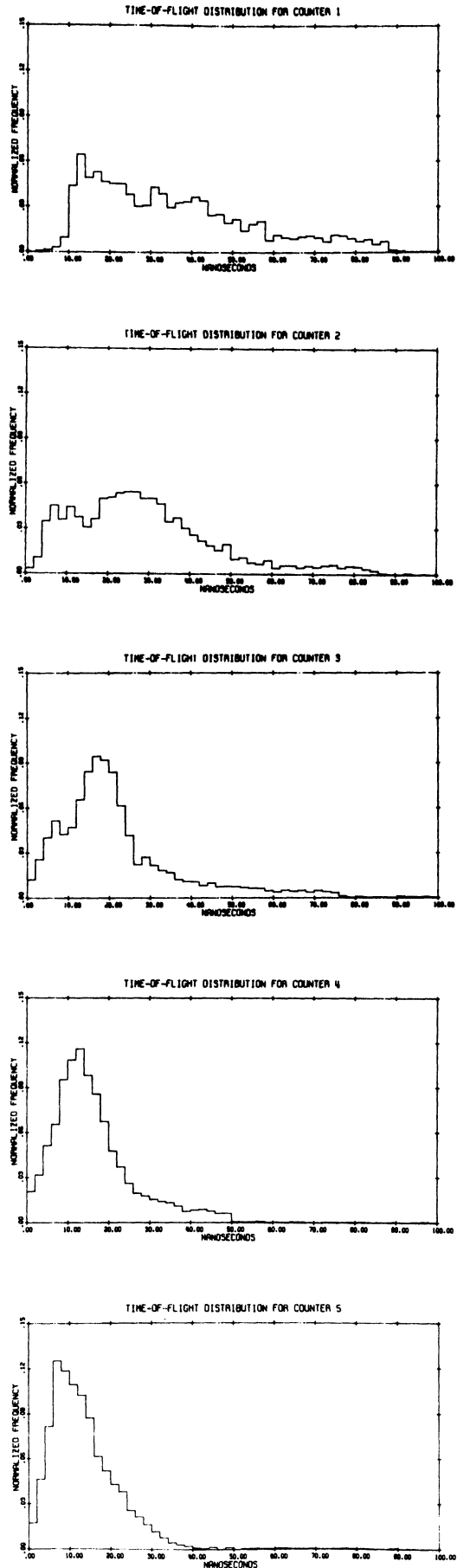
Fig. 23   The Time-of-Flight Distributions as a
Function of Neutron Counter

usual equation p=eBr/c. For a uniform field B of length L

this can be written in the form

$$p = \frac{B \cdot L}{(1.31 \times 10^6)(2 \sin \theta/2)} \tag{11}$$

in which the momentum, p, is given in GeV/c and B·L is given

in gauss-inches. Figure 24 illustrates the derivation of the

above formula. The uniform field approximation was used as

a starting point to determine the proton momentum by a method

of iteration. As mentioned, the Magnet Test Group provided

maps of the vertical component of the magnetic field for

various currents. (The horizontal components of the magnetic

field were neglected in this experiment since these provided

only a small vertical focusing.) Since at these currents

the magnetic field varied linearly with the current, a map

was generated for the operating current, 523 amperes, by

using the following formula

$$B_{523} = \left(\frac{523}{392}\right) B_{392} \tag{12}$$

for which a map was provided at 392 amperes. This new map

was folded about the three orthogonal planes which inter-

sected at the center of the magnet gap and averaged. This

procedure yielded a map containing only 1/8 as many points as

in the original, and thus was of a size more easily handled

by computers. No errors were introduced by this procedure

since the magnetic field was symmetric (within a few tenths

of a percent) about the gap center.

The actual calculation of the proton momentum proceeded

$$p = \frac{eB}{c} R$$

$$p = \frac{eB}{c} \frac{L}{2 \sin(\Theta/2)}$$
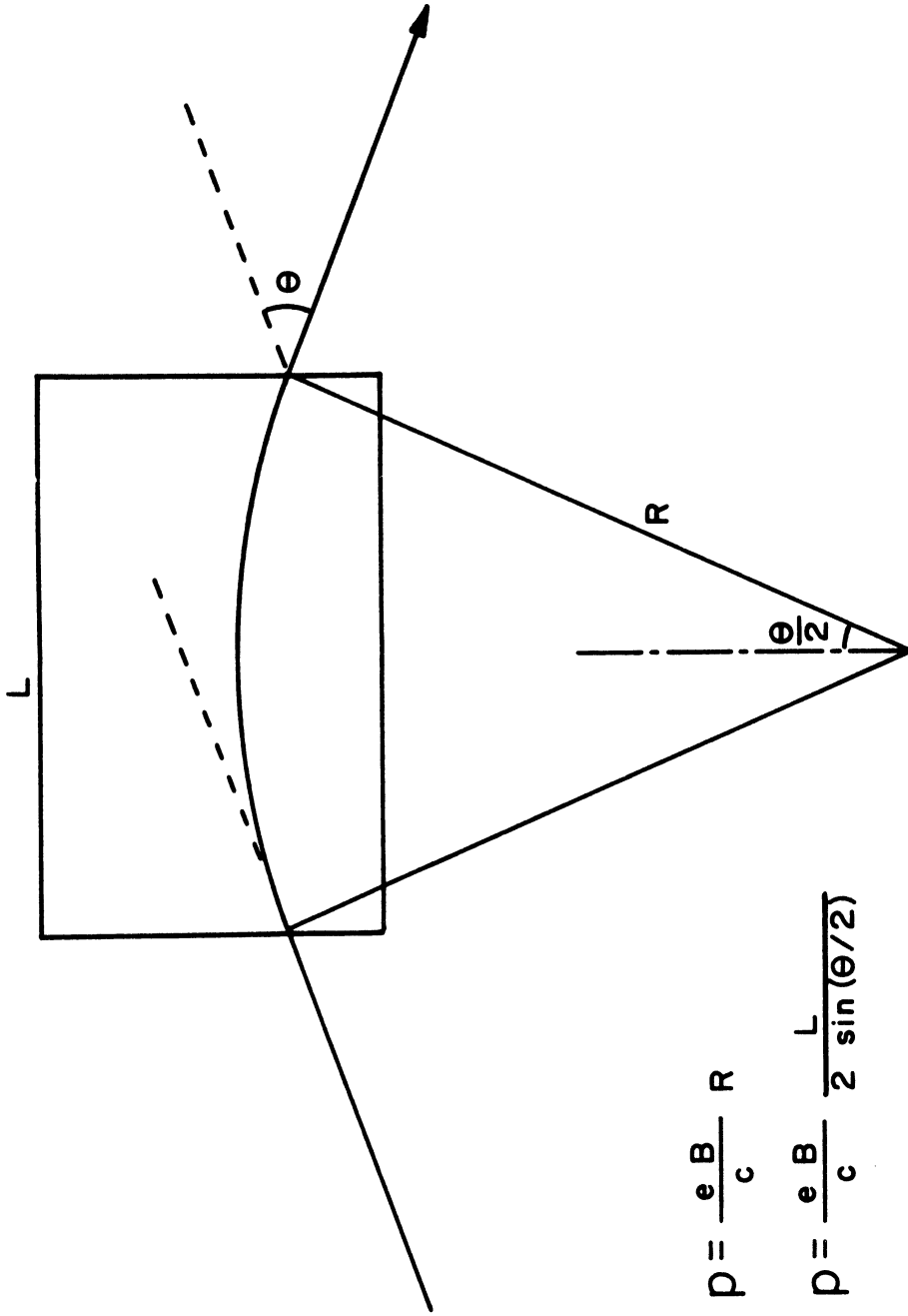
Fig. 24 The Path of a Charged Particle in a Uniform
Magnetic Field

by the following steps. A first guess of the momentum was
made using Equation (11) where B·L was replaced by the
integral $\int$B·dl through the center of the magnet. The integral
was 4.77×10^5 gauss-inches. The angle, θ, was the angle
between a straight line drawn through the sparks in the front
chambers and a line drawn similarly in the back chambers.
The initial parameters for the computer stepping procedure
were the first approximation to the momentum, the angle θ,
and a position which was the spark location in chamber three.
The proton was stepped from the back to the front through
the magnetic field in 1.7-inch steps. The direction of the
steps was parallel to the 36-inch sides of the gap. At each
step position the magnetic field was calculated by interpo-
lating from the known fields at the nearest eight points
which defined a surrounding box. The proton was then
projected along a straight line to the next step position
and a new angle determined with the aid of Eq. (11). This
procedure gave a series of chords to the real curved trajec-
tory.

In this way the proton was projected from the back
chambers to each of the front chambers and an aiming error
obtained for each. Using the aiming error in one of the
chambers, the computer performed an appropriate modification
to the first approximation value of the momentum and repeated
the stepping procedure with the new momentum. This procedure
was repeated until two values of the momentum were
obtained—corresponding to momenta which gave 0.005 inch,

or less, position errors in each of the front chambers. The
two momenta were averaged and corrected for the finite step
size. The correction for the step size was determined in
test calculations by varying the step size from 1.7 inches
to 0.085 inch. Typical results are presented in Fig. 25.
The top line represents the momentum found by projecting into
the front chamber; the bottom line is the similar thing for
the second chamber, and the dotted line represents the
average. Presumably the fact that all three lines do not
coincide can be traced to the effects of measurement errors.
The value of the momentum for zero step size could be found
by multiplying the 1.7-inch value of the momentum by 1.018.
This factor was found to be independent of the momentum. An
insignificant correction was made for energy loss in the
liquid hydrogen and other material through which the proton
passed before entering the magnetic field.

The error in the proton momentum determination was due,
in the main, to spark measurement errors. Coulomb scattering
effects were less significant. The proton momentum errors
ranged from about 2% to about 7% as shown in Fig. 26. Actually
the errors varied slightly with angle.

D. Kinematics

If one assumes that the interaction were n-p elastic,
then the proton momentum and scattering angle completely
determine the collision kinematics. This can be seen if we
restrict the discussion to the plane of the interaction.
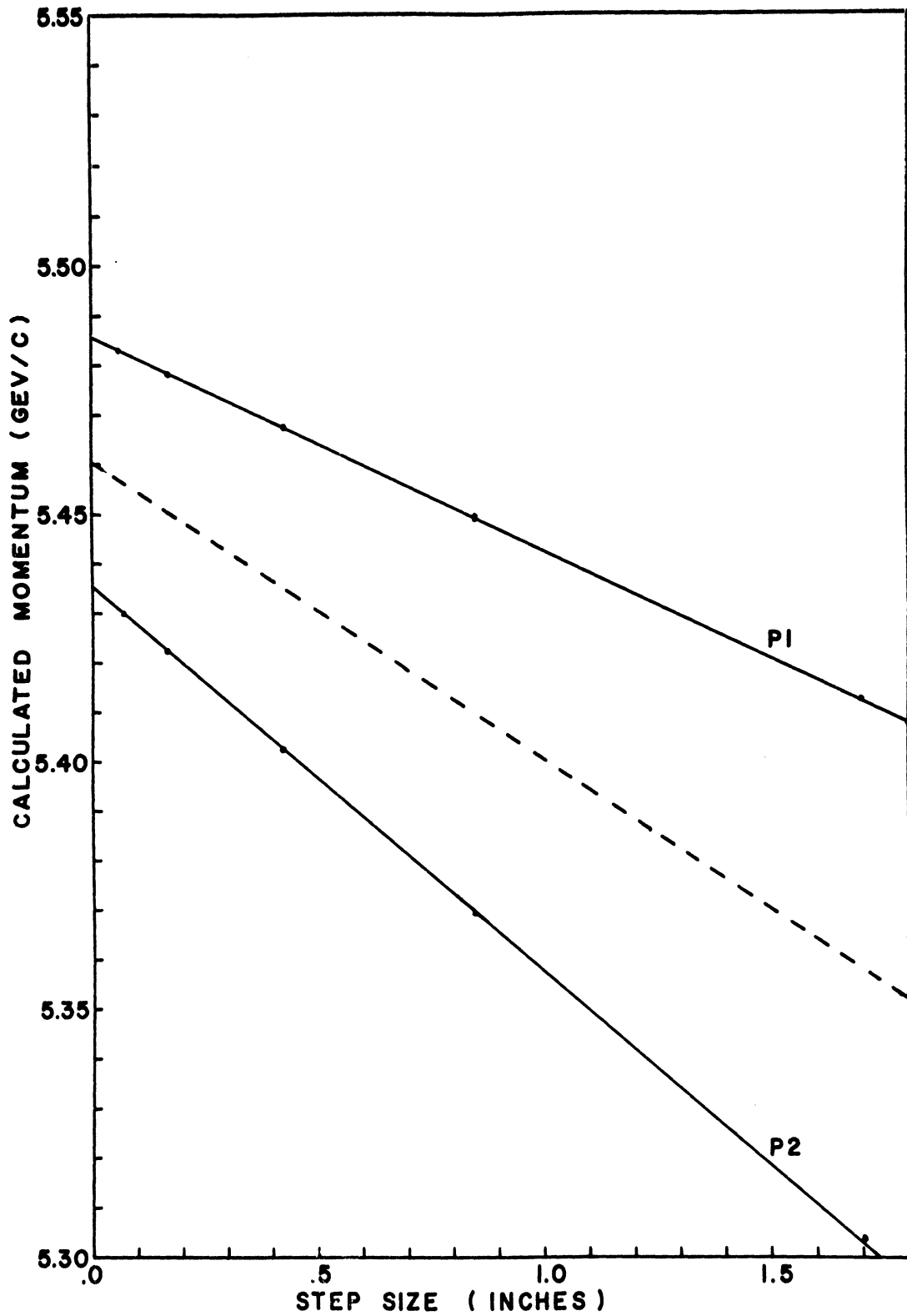
Fig. 25 The Step-Size Correction to the Proton Momentum

ERROR IN PROTON MOMENTUM DETERMINATION
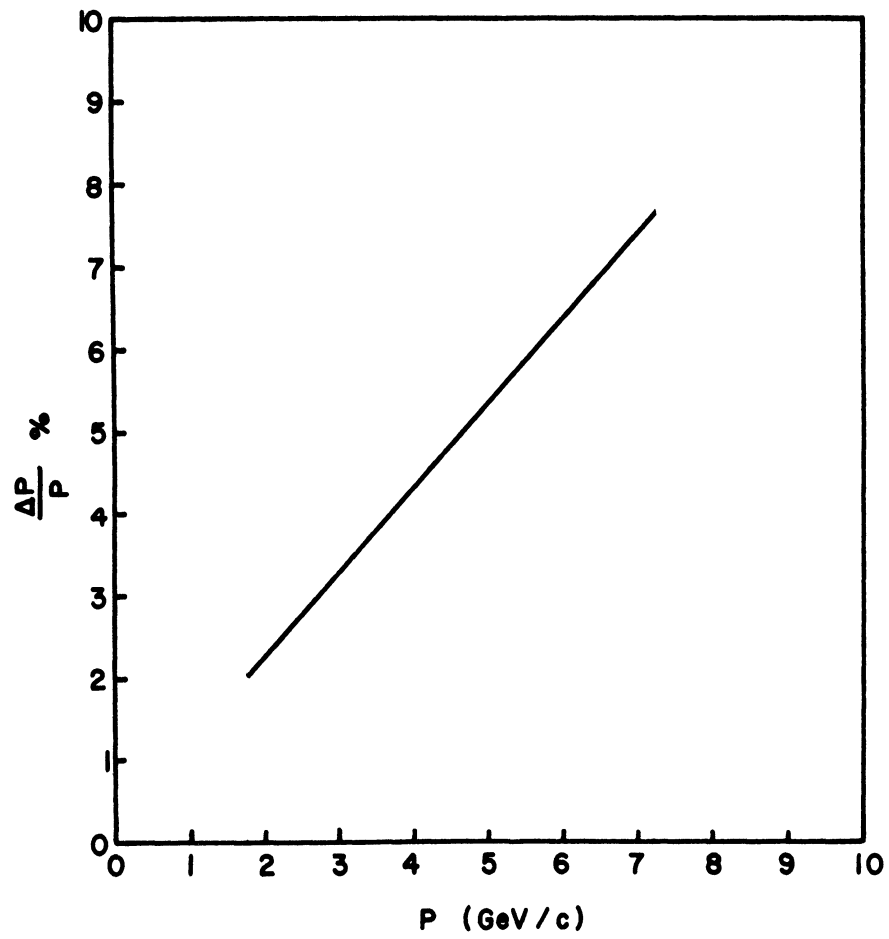
Fig. 26 The Error in the Determination of the Proton
Momentum

Then the conservation of energy and momentum supplies three
equations for which there are three unknowns: the incoming
neutron momentum, the scattered neutron momentum, and the
angle of scatter for the neutron. The three equations
were cast as

$$\sqrt{p_{beam}^2 + m_n^2} + m_p = \sqrt{p_n^2 + m_n^2} + \sqrt{p_p^2 + m_p^2} \,,$$

$$p_{beam} = p_n \cos\theta_n + p_p \cos\theta_p \,, \tag{13}$$

$$p_n \sin\theta_n = p_p \sin\theta_p \,.$$

Once these equations were solved all other quantities of
interest could be calculated. In particular, the
four-momentum transfer squared, u, could be calculated as a
function of p_p and θ_p.

The incoming neutron momentum was essentially the same
as the scattered proton momentum, and so the errors were
identical for the two. The errors for the four-momentum
transfer were a function of the beam momentum. Representative
errors are shown in Fig. 27. For beam momenta above 5 GeV/c
and for four-momentum transfers less than 0.03 $(GeV/c)^2$
the four-momentum transfer was recalculated from the neutron
time-of-flight. The errors for this procedure are given by
the dotted lines.

E. Data Cuts and Subtractions

Three cuts were independently made on the data in order
to weed out inelastic events. The cuts were a coplanarity
cut, a counter cut, and a timing cut.
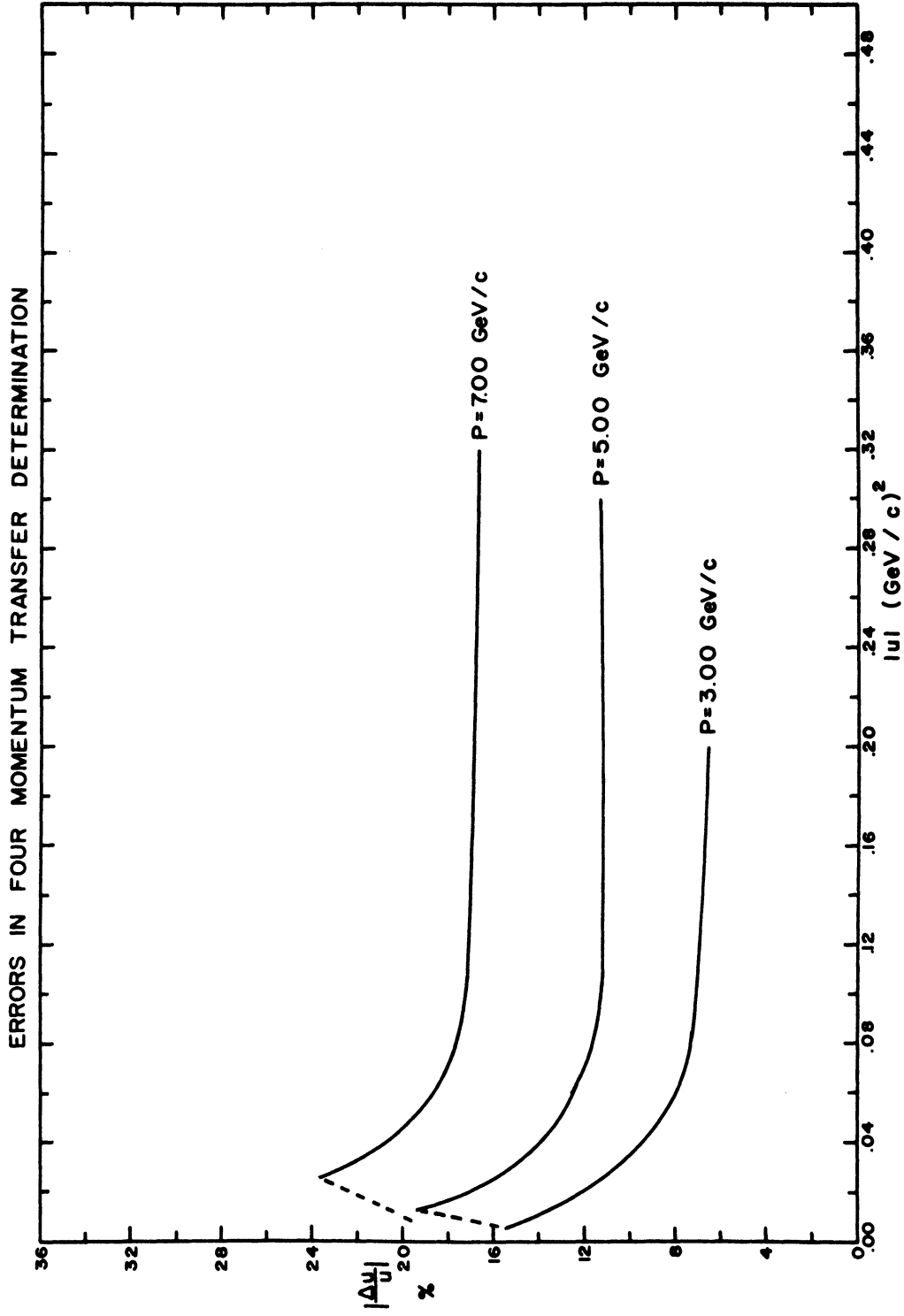
Fig. 27 The Error in the Determination of the
Four-Momentum Transfer

The size of the neutron counters and their placement, together with the size of the beam, combined to give the system a ±7.5 degree maximum planar acceptance about the horizontal plane. No coplanarity information other than the trigger requirement was available from the neutron counters. A coplanarity "chi square" term was calculated according to

$$\chi_\varphi^2 = \begin{cases} 0 & \text{if } |\varphi| \le 7.5^\circ = 0.1325 \text{ radians} \\ \\ \left(\dfrac{|\varphi| - 0.1325}{\sigma}\right)^2 & \text{if } |\varphi| > 0.1325 \text{ radians} \end{cases} \qquad (14)$$

where φ was determined from the tracks in the two front proton spark chambers. The expected error, σ, was a function of the proton momentum and angle. It contains the effects of Coulomb scattering of the proton and measuring errors in the spark locations. Events were kept for which χ_φ^2 was less than or equal to one.

Each counter had a certain angular acceptance due to the counter size and the target length. If upon solving the kinematics, the angle of the scattered neutron did not lie within the range of acceptance of the neutron counter which had been triggered, the event was thrown out. If two adjacent neutron counters fired the angular limits were taken for the counter for which the difference between the measured and the calculated times-of-flight were a minimum.

A final cut was made by constructing a "chi square" term for the timing information as follows

$$\chi^2_{timing} = \left(\frac{measured\ timing\ -\ calculated\ timing}{\sigma_t}\right)^2 \quad (15)$$

As was explained in an above section, the measured timing was taken from the oscilloscope trace and the calculated timing was obtained from the kinematical reconstruction of the event. The expected error, σ_t, contained terms which reflected timing measurement errors, pulse height effects, and the neutron counter traversal time. Only events were kept for which χ^2_{timing} was less than or equal to one.

From an analysis of the data generated by the Monte Carlo program which is discussed in Sect. IV-F, it was estimated that about 25% of the elastic events were removed by the data cuts described above. The fraction of elastic events cut was found to be independent of beam momentum and of four-momentum transfer.

Figure 28 demonstrates the effect of these cuts. It shows the distribution of the difference between the measured and the calculated timing for events with $|u| \leq 0.025$ $(GeV/c)^2$. Each event is represented by a number which indicates which neutron counter was triggered. As can be seen, each of the three cuts independently discriminated strongly against the obviously inelastic events under the secondary peak. The inelastic events were presumably gammas from π° decay. However, two points should be made. First, the efficacy of the timing cut is reduced in the larger $|u|$ bins as can be

72
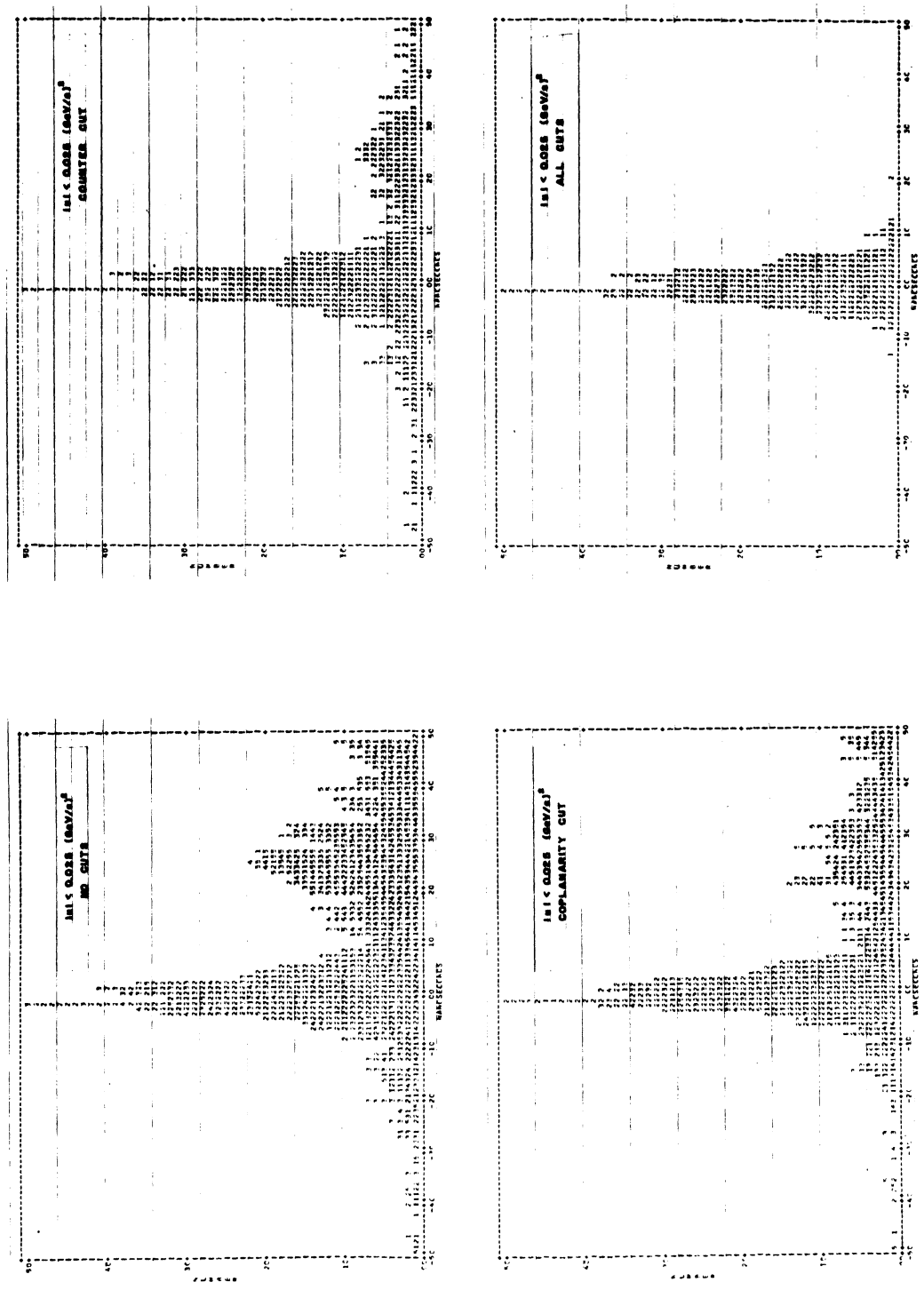
Fig. 28 The Effect of the Data Cuts on the Timing Differences

seen in the uncut distributions in Fig. 29. As $|u|$ increases, the inelastic peak moves under the elastic peak. Thus, for large $|u|$ we are forced to rely on the counter and the coplanarity cuts to reduce the inelastic background. Secondly, in all $|u|$ bins after the counter and coplanarity cuts were made, a background persisted which extended under the elastic peak. Consequently, a background subtraction was made to the data.

The cuts described above throw out individual events. The subtraction was made to the cross sections as a whole, but as a function of beam momentum and four-momentum transfer. The subtraction was determined by binning the data—after the coplanarity and counter cuts had been made—in bins of incident momentum and four-momentum transfer as shown in Fig. 30. An effort was made to extend the tails of the background distribution under the peak by drawing a smooth line as shown. The events under that line and within the limits of the timing cut were counted and then the appropriate fraction subtracted from the cross section. The subtractions ranged from about 5% for the highest momentum bins to 15% for most of the rest of the data. As the statistical errors in the data were $\geqslant 10\%$, uncertainties in the subtractions were not considered significant.

F.   Geometric Detection Efficiency

In order to determine cross sections from the numbers of events it was necessary to know the detection efficiency
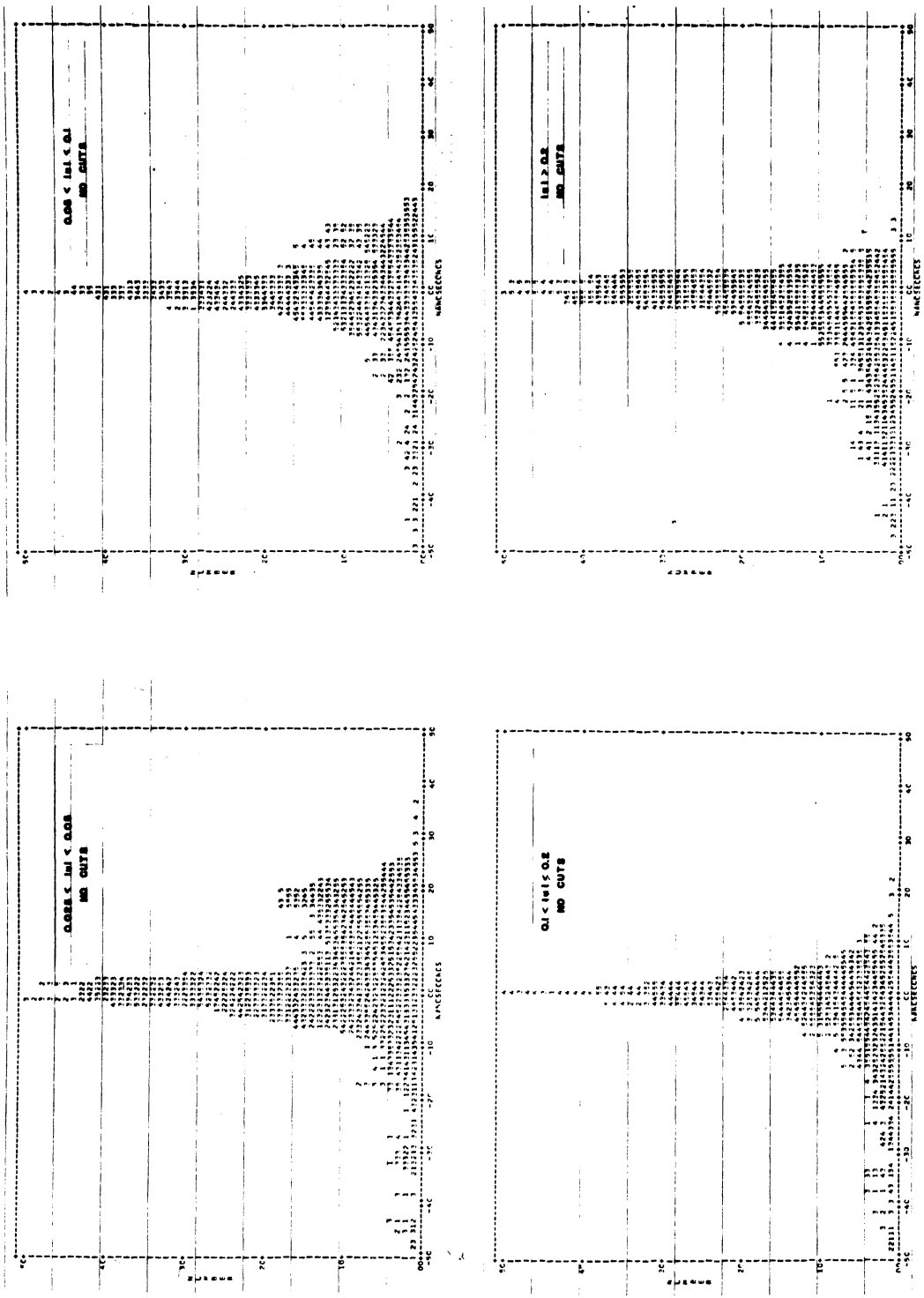
Fig. 29 The Difference between the Measured and the
Calculated Timing as a Function of u
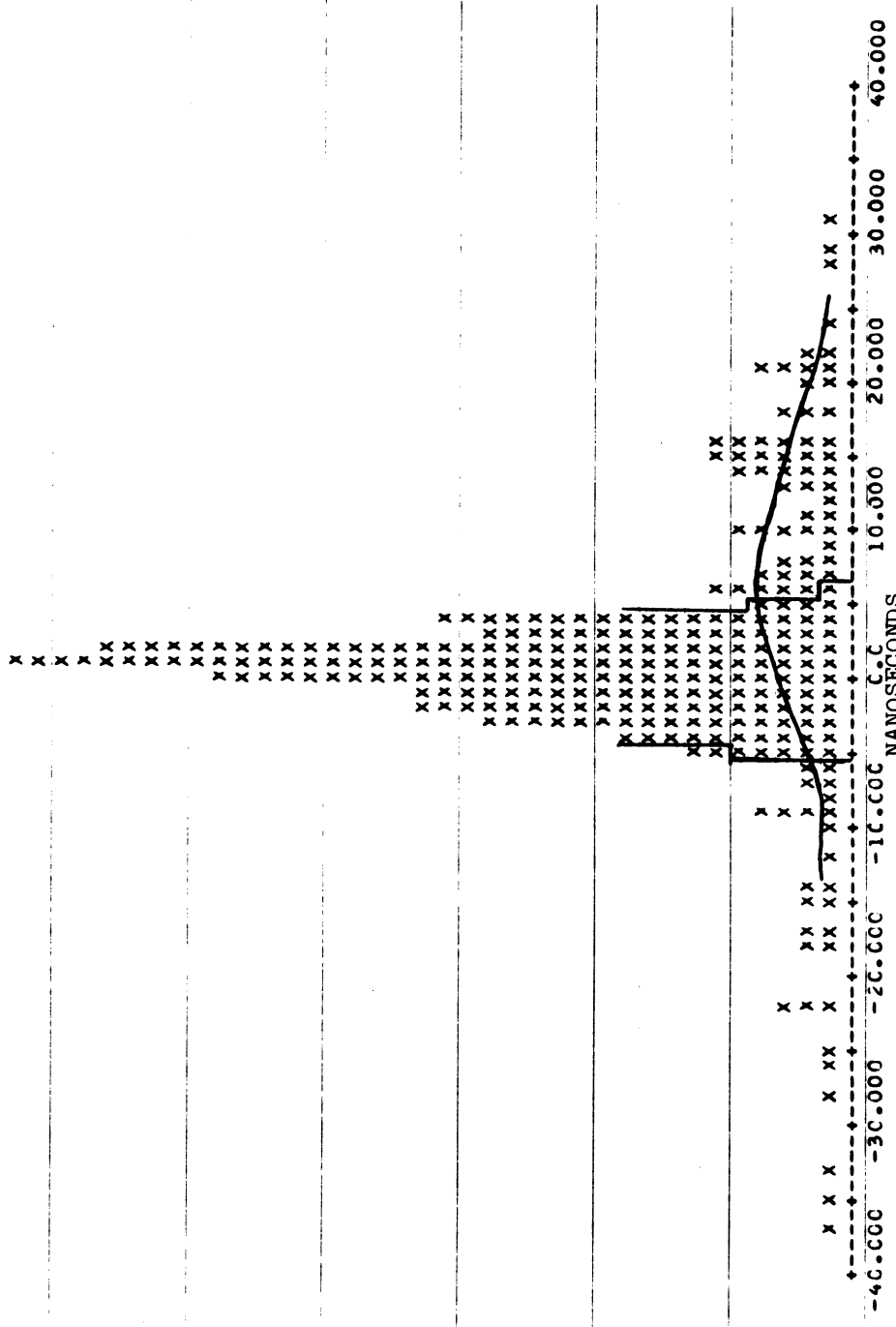
Fig. 30 A Sample Background Subtraction

of the neutron counters and the solid angle of the system.

The neutron detection efficiency will be discussed in another

section. The solid angle, or geometric efficiency, of the

experiment was investigated via Monte Carlo techniques.

Appropriate random number generators were used to simulate

the experiment. For a given computer run, the incident

neutron momentum and the center of mass scattering angle,

or four-momentum transfer, were fixed. With these quantities

fixed, many events were generated with randomly chosen

planar angles, random secondary scatterings, and so forth.

All important features of the experiment were simulated on

the computer. The ratio of accepted events to generated events

was calculated for each range of u and of beam momentum.

This fraction was then used to correct the data. A descrip-

tion of the salient features of the Monte Carlo program

follows.

The beam size, the beam divergence, and the beam

attentuation in the liquid hydrogen target were simulated.

The plane of the scattering was randomly chosen with the

restriction that the neutron always be scattered to the side

on which the neutron counters stood. (Restricting the planar

angle to an hemisphere saved valuable computer time as a

little investigation had shown that no events were accepted

from the other hemisphere. The detection efficiency found

in this way had to be divided by two when computing the

absolute cross sections.) Once the interaction point and

plane had been set the directions of the scattered neutron

and proton were determined.

The fate of the scattered neutron was investigated next. Random rescattering of the neutrons in the liquid hydrogen were generated according to a parameterization of the low energy n-p cross sections prepared by Clements and Winsberg.[39] Most of the rescattered events did not strike the neutron counters. Further attenuation in the target dome, the air, and the anticounter Al were simulated. In an effort to save computation time, scattered neutrons with kinetic energies ≤ 1 MeV were rejected. This could be done since the neutron detection efficiency of the neutron counters was zero for such low energy neutrons. If the neutron did not strike a counter a new event was generated; otherwise, the counter which was struck was recorded and the fate of the proton was then investigated.

Coulomb scattering effects and energy loss effects for the proton were simulated in the liquid hydrogen, the target flask, the target dome, the spark chambers, and the scintillators. The proton was stepped through the magnet in 0.097-inch steps. The coordinates of the proton in each of the spark chambers were recorded. Tests were made to insure that the proton passed through each of the three scintillators in the proton spectrometer. If not, a new event was generated. If the neutron went into a neutron counter and the proton passed properly through the spectrometer, the event was considered as having been recorded on film.

From this point on the Monte Carlo program simulated the

analysis of the real data. That is, measurement errors were randomly generated and were tacked onto the spark chamber coordinates. The kinematics of the event were then reconstructed as for the actual data. Further, the counter, coplanarity, and timing cuts were made. If the event survived all of these it was considered accepted and was properly binned. At the end of the run the ratio of accepted events to generated events was calculated. This ratio, called the "geometric detection efficiency", is presented in Fig. 31 for two beam energies and as a function of four-momentum transfer. The errors are based on the statistics on the number of Monte Carlo accepted events. The dashed line is a smooth curve drawn through the data.

G. Neutron Detection Efficiency

The thick plastic scintillator, the photomultiplier, and the associated circuitry constituted a system whose detection efficiency had to be calculated. That is to say, only a fraction of the neutrons striking a scintillator scattered in such a way as to produce charged particles with enough energy to produce pulses above the threshold of the system. The ratio of detected neutrons to neutrons striking the counter is called the neutron detection efficiency and was calculated with the aid of a FORTRAN program developed by Kurz.[40]

Kurz's program treats both initial and secondary scattering effects on both hydrogen and carbon in the
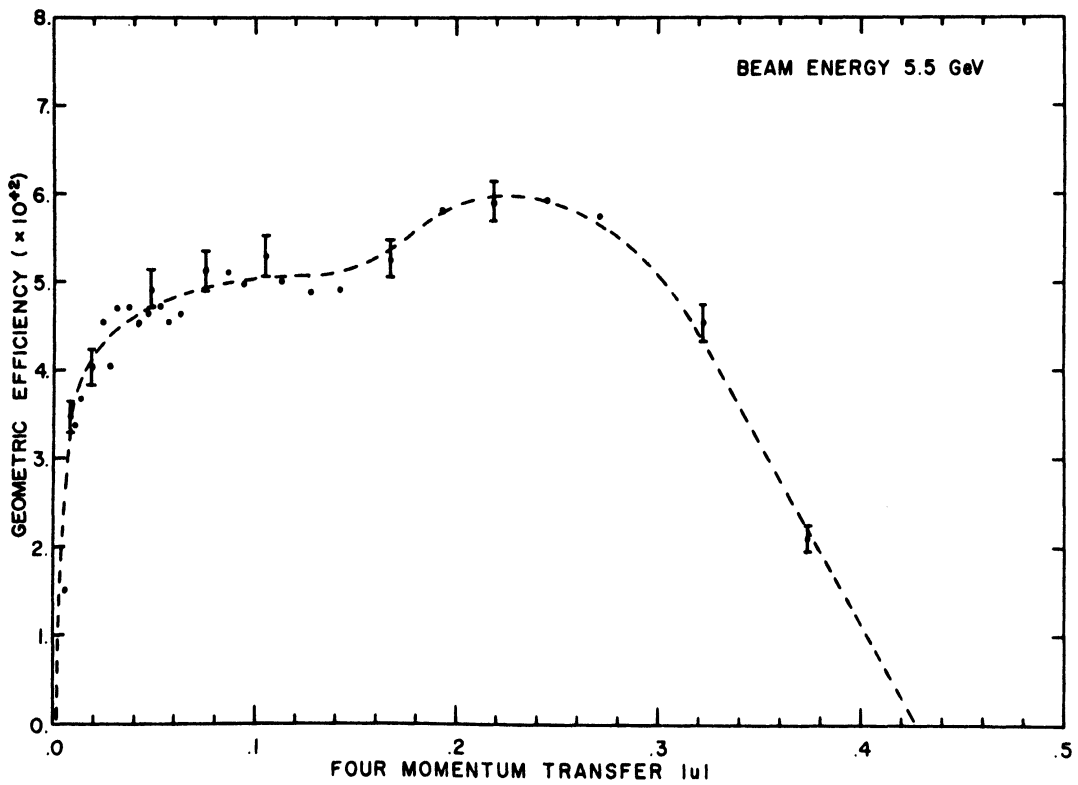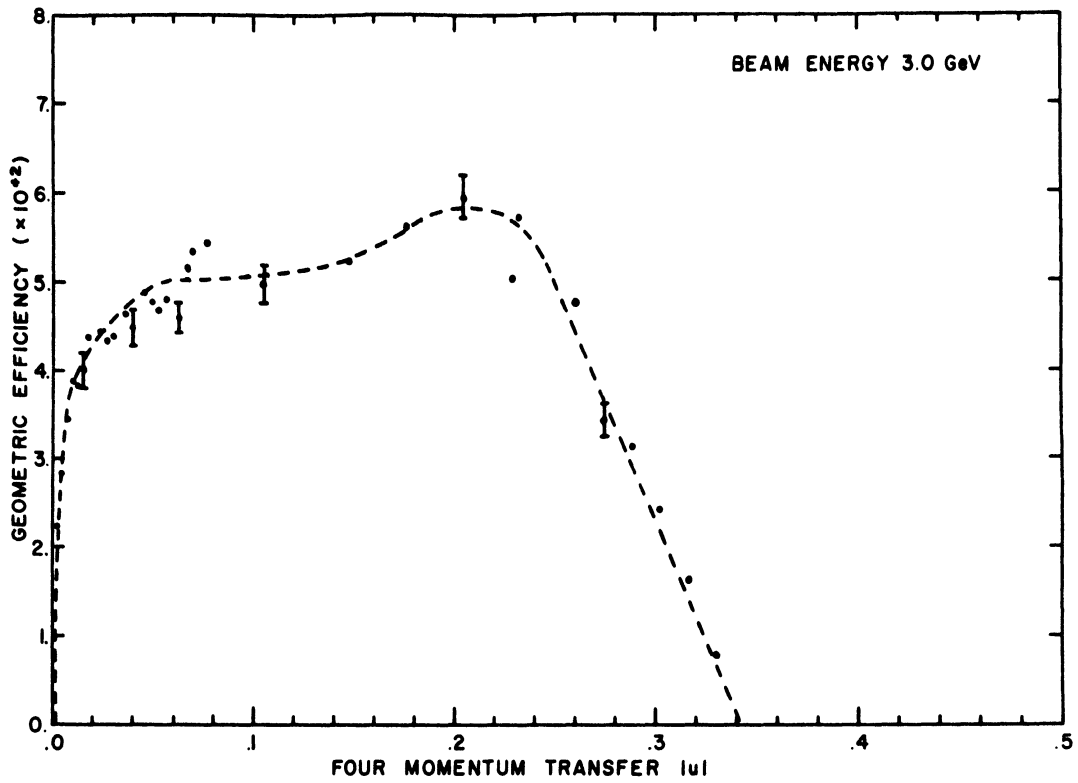
Fig. 31 The Geometric Efficiencies for Two Beam
Momenta

scintillator. Saturation effects in the production of scintillation light are considered as well. The program assumes a cylindrical shape for the scintillator with the neutrons uniformly and normally illuminating the circular face. The results of the program have been experimentally verified for several counter systems.[40-41]

Our counters were each 15 cm long and, for the purposes of the calculation, were assumed to be 9.2 cm in radius. This value for the radius gives the area of the face of each counter. As the detection efficiency was a weak function of the counter radius, no significant errors were introduced by assuming a circular cross section for each counter. The detection threshold was taken to be 0.7 MeV for electrons. The threshold energy was taken to be slightly lower than the 0.76 MeV maximum energy carried by the betas produced by Tl^{204} decay in order to reflect the actual beta energy spectrum and the counting rates at which the thresholds were set. Because of saturation effects these electrons simulated 2 MeV protons.

The results of the calculation are presented in Fig. 32. The first peak is due to the rise from threshold and to the falling n-p cross sections, while the second peak is due to the onset of n-C interactions. Errors in the detection efficiency of ±10% of the calculated value are associated with the uncertainties in the cross sections used in the calculations. Somewhat smaller errors are involved in determining the threshold and in neglecting edge effects.
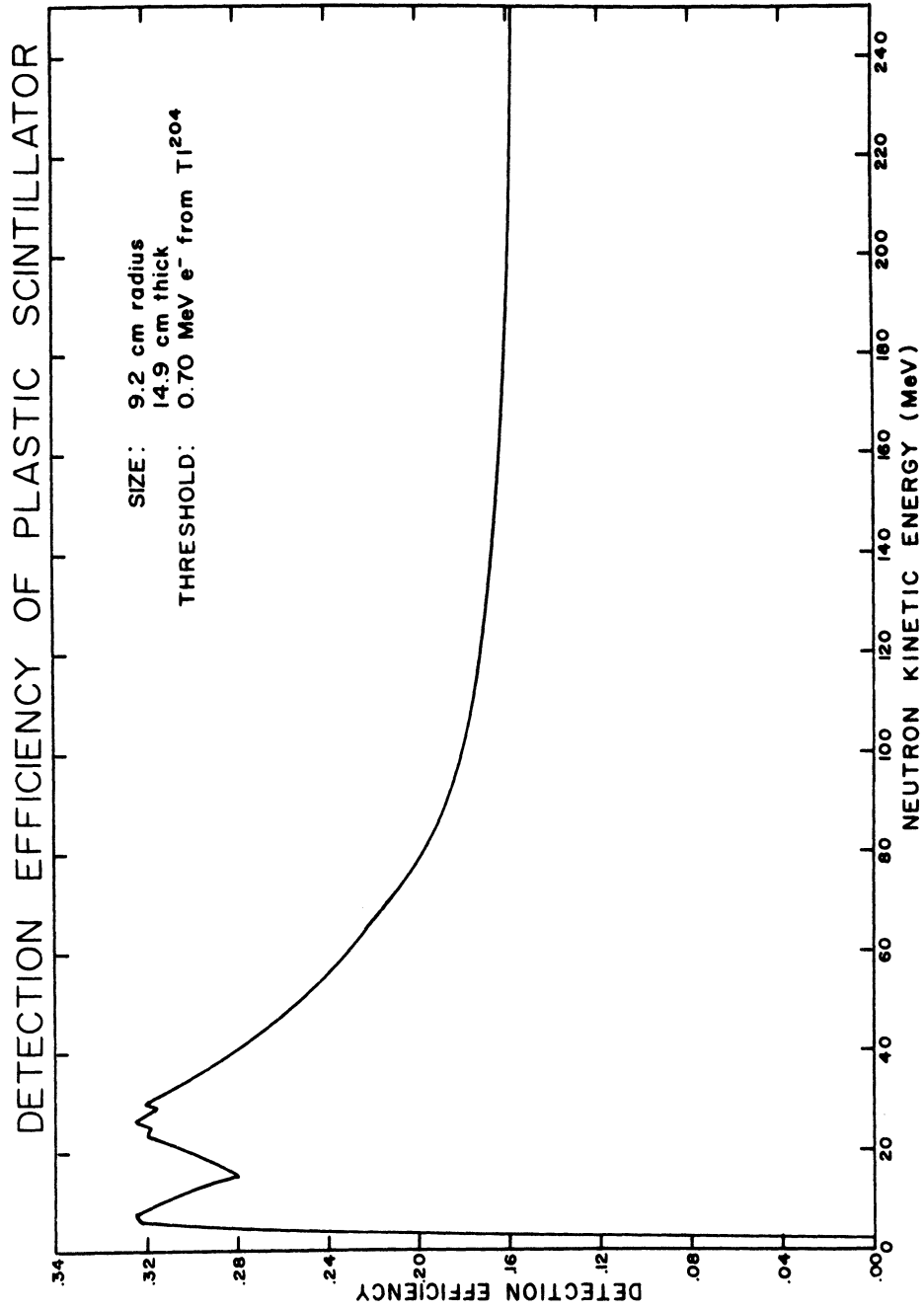
Fig. 32 The Detection Efficiency of the Neutron Counters

It is important to note that all of the counters were set at the same threshold, and therefore, the detection efficiency was the same for all counters. Since the neutron energy is related to u by Eq. (6), errors in the efficiency would cause u-dependent errors, but these would be independent of the beam momentum. The statistical errors in our measured cross sections are typically >10% so the uncertainties in the neutron detection efficiency are not expected to be important.

H. <u>Data Contaminants</u>

Contamination of the data from inelastic collisions was investigated via Mont Carlo techniques. The program which was used to calculate the geometric detection efficiency was modified for these calculations. The three processes in this category that were investigated were

$$n + p \rightarrow \Delta^+(1236) + n$$
$$\Delta^+ \rightarrow p + \pi^0$$
$$\pi^0 \rightarrow \gamma + \gamma,$$

$$n + p \rightarrow p + \Delta^0(1236)$$
$$\Delta^0 \rightarrow n + \pi^0$$
$$\pi^0 \rightarrow \gamma + \gamma,$$

and

$$n + p \rightarrow d + \pi^0$$
$$\pi^0 \rightarrow \gamma + \gamma.$$
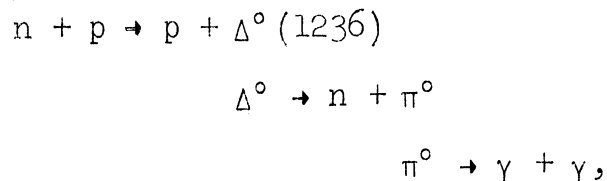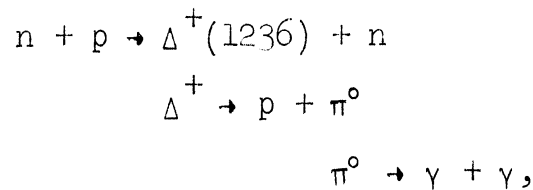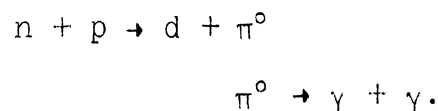
The total cross section for each of the above processes was assumed to be about ten times as large as the elastic charge exchange cross section. No energy dependence was considered.

The total cross sections did not enter in the Monte Carlo program directly, but were used in estimating the absolute background. The four-momentum transfer dependence of the production was taken to be e^{10u}.[42] The incident neutron momentum was randomly chosen, but was constrained to reflect the distribution shown in Fig. 33.[2] This beam spectrum was obtained from an analysis of the data from the other phase of this experiment. The width of the resonance was taken to be 160 MeV rather than 120 MeV in an attempt to include the background under the resonance peak. In the same vein, isotropic decay of the resonance was simulated. Isotropic decay of the pion into two gammas was required. The gammas, as well as the neutrons, were tracked to the neutron counters. Events which triggered both the neutron counters and the proton counters, i.e., simulated events for which pictures were taken during data collection, gave distributions in four-momentum transfer which tended to peak at u=0. However, the three cuts made on the data eliminated the peaking and reduced the background to a level that was estimated to be $\approx 20\%$ of the elastic events. This was further justification for the background subtraction which was discussed in Sect. E above. The process $n + p \rightarrow \Delta^+ + n$ was found to be the most serious source of contamination. It accounted for about 75% of the background.

Processes involving beam contaminants were investigated and found not to contribute to the background. The reactions considered were
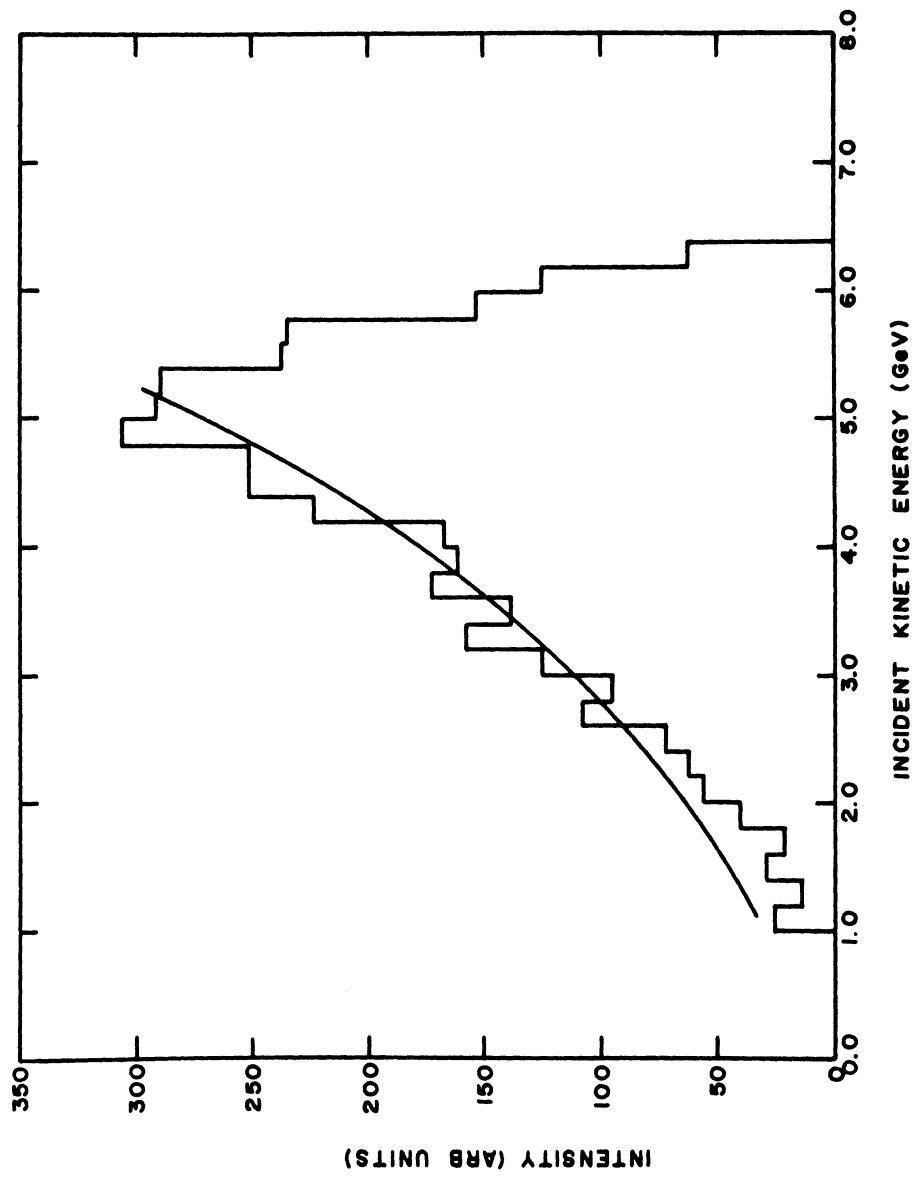
Fig. 33 The Neutron Beam Spectrum

$$K^0 + p \rightarrow K^0 + p$$

and

$$\gamma + p \rightarrow \gamma + p.$$

I. Target Empty Correction

Finally, the target empty events were investigated. The target empty trigger rate was 1/3 of the target full trigger rate. However, the cuts made on the data discriminated more heavily against the target empty events. The few remaining target empty events assumed the appearance of a broad background when examined as a function of incident momentum and four-momentum transfer. They represented something under 10% of the cross section under the elastic peak. Therefore, it was assumed that the background subtraction described above removed the target empty contribution to the cross sections.

V. RESULTS AND CONCLUSIONS

A. Differential Cross Section Formula

The formula which was used to calculate the differential cross sections is

$$\frac{d\sigma}{du} = \frac{X\,Y\,Z}{(\rho l N/M)\,(IB)} \sum_i \frac{A}{(\epsilon_g/2)\,(\epsilon_n)\,(F/\delta p)\,\Delta p\,\Delta u} \qquad (16)$$

in which the sum is over all events and in which

$\frac{d\sigma}{du} = \frac{d\sigma}{du}(p,u)$ = the differential cross section as a function of beam momentum and of four-momentum transfer squared.

X = film scanning efficiency correction = 1.12

Y = correction for events not measured due to the presence of extra tracks = 1.2

Z = Z(p,u) = background subtraction factor

ρ = density of liquid hydrogen = 7.08×10^{-2} g/cm^3

l = length of liquid hydrogen target = 10.2 cm

N = Avogadro's number = 6.02×10^{23} protons/mole

M = molecular weight of hydrogen = 1.008 g/mole

$\rho l N/M$ = 4.33×10^{-4} protons/millibarn

A = A(p,u) = correction for (p,u) bins for which the ranges of p or u are restricted by kinematics or detection efficiencies to be less than the bin sizes. A = 0 or from 1 to 2.

$\epsilon_g/2$ = solid angle or geometric detection efficiency.

86

The factor 2 comes from the fact that the Monte Carlo calculation was restricted to one hemisphere.

ϵ_n = neutron detection efficiency. Events were not considered for which the product $(\epsilon_g/2)(\epsilon_n)$ was less than half the maximum value.

$F/\delta p$ = $F(p)/\delta p$ = fraction of the beam spectrum per momentum bin. The beam spectrum was determined in the forward scattering portion of the experiment. The results are presented in Fig. 33.

Δp = incident momentum bin size for which the cross section was being calculated.

Δu = four-momentum transfer bin size for which the cross section was being calculated.

B = number of counts on monitor B.

I = neutrons in beam per count on monitor B. The determination of this number is discussed in the next section.

B. Normalization

Normalization refers to the process of determining the numbers in the above formula or of fixing absolutely the scale of the differential cross section in some other way. In practice the difficult quantity to determine is usually the beam flux. It is always difficult to determine

the flux of a neutron beam. It is especially so when the beam spectrum encompasses a wide range of energies as in this experiment. Consequently, no effort was made to directly determine the flux. Instead, the forward-scattered data were normalized to the n-p total cross sections via the optical theorem.[2] The plan was to normalize the charge exchane data to the forward data.

The original hope was to make the connection between the forward data and the charge exchange data in one of two ways. One possibility was that the ranges of the four-momentum transfer for the two phases of the experiment would overlap so that the differential cross sections could be smoothly joined. The detection efficiencies were such that no overlap existed. The second method involved a convoluted calculation which depended on the target sizes, the monitor rates, the detection efficiencies, and other physical parameters of the two experiments. This method also did not work.

We felt that it was not appropriate to normalize the data to the data of Friedes et al.[4] or that of Manning et al.[5] since their normalizations are not certain. Therefore, our data are not normalized. However, the relative normalizations between incident momentum bins are fixed since the neutron beam spectrum was known. Again the reader is referred to Fig. 33. Above 6 GeV/c, uncertainties in our beam spectrum introduce errors in the relative normalizations of about ±50%. Similar errors are introduced in the

relative normalizations of the data for momenta below

2.5 GeV/c.

C. Results and Conclusions

The differential cross sections are given in tabular

form in Tables II-XI and in graphical form in Figs. 34-41.

The cross sections were not plotted for 1.75 GeV/c to

2.25 GeV/c as they did not possess enough points to present

interesting plots. The errors quoted are statistical

errors only.

Several points should be made about the data. First

of all, the normalization is not determined; however, that

fact in no way effects the u dependence of the data.

Secondly, the neutron detection efficiency limits the

range in four-momentum transfer to $|u| > 0.01$ $(GeV/c)^2$

which is outside most of the sharp backward peak seen in

other data. Evidence for a sharp backward peak does

exist in the data however. Thirdly, the data from 2.25

GeV/c to 3.00 GeV/c show a strong energy dependence in

the shape of the cross sections. The data from 2.25 GeV/c

to 2.50 GeV/c and from 2.75 GeV/c to 3.00 GeV/c show

backward peaks, while the data in the 2.50 GeV/c to 2.75

GeV/c bin show a dip. Fourthly, the data above 3.25 GeV/c

indicate the existence of a plateau in the differential

cross sections at a four-momentum transfer of about 0.08

$(GeV/c)^2$. And finally, the data for large $|u|$ may be

characterized as

$$\frac{d\sigma}{du} \propto e^{5u}. \tag{17}$$

The strange energy dependence of the differential cross

sections between 2.25 GeV/c and 3.00 GeV/c, and the

existence of a plateau in the differential cross sections

at $|u| = 0.08$ $(GeV/c)^2$ are the most striking features of

the data. Future experiments should carefully investigate

the n-p charge exchange differential cross sections in

these regions.

Our data, together with that of Mischke et al.[7] show

that the behavior of the charge exchange cross section

between 1 and 7 GeV/c is much more complicated than

previously realized. Not only does the slope of the sharp

peak vary rapidly with energy, but the shape of the cross

section just outside of the peak varies in an apparently

complicated way.

In conclusion, we offer a critique of the techniques

employed in this experiment. The advantages of this

technique are given below.

1) This technique offers a higher data taking rate.
   The data were taken in 100 hours of running time.

2) The ratio of events to triggers is much better. Our
   ratio was $\sim 10^{-1}$, while the ratio for Manning et al.[5]
   was 10^{-3}.

3) The technique can be easily extended to higher
   energies. Experiments employing this technique
   are currently being performed at the AGS and at the

ZGS.

4) With some refinements of the technique a recent experiment used this technique to study polarization in n-p charge exchange.

5) This technique measures simultaneously the cross sections for a large range of neutron energies.

There are two principle disadvantages to the technique.

1) The neutron counter detection efficiency must be known.

2) It is difficult to measure the cross sections for small u. In particular, the u=0 values of the differential cross sections cannot be measured.

CROSS SECTIONS FOR 1.75 GEV/C TO 2.00 GEV/C

ABS U BINS			NUMBER	ABSU $\|u\|\ (GeV/c)^2$	SIGMA $\frac{d\sigma}{du}$	ERROR	COSINE $\cos\Theta_{cm}$	SIGMA $\frac{d\sigma}{d\Omega}$	ERROR
0.0	TO	0.01000	0	0.0	0.0	0.0	0.0	0.0	0.0
0.01000	TO	0.02000	45	1.5135E-02	3.6497E 01	5.4407E 00	-9.8618E-01	6.3792E 00	9.5095E-01
0.02000	TO	0.03000	50	2.4981E-02	3.8402E 01	5.4308E 00	-9.7690E-01	6.6415E 00	9.3925E-01
0.03000	TO	0.04000	28	3.4148E-02	2.5774E 01	4.8708E 00	-9.6916E-01	4.5516E 00	8.6016E-01
0.04000	TO	0.05000	42	4.5571E-02	3.1580E 01	4.8730E 00	-9.5819E-01	5.4945E 00	8.4783E-01
0.05000	TO	0.07000	41	5.5537E-02	3.5658E 01	5.5688E 00	-9.4964E-01	6.2747E 00	9.7994E-01
0.07000	TO	0.09000	0	0.0	0.0	0.0	0.0	0.0	0.0
0.09000	TO	0.11000	0	0.0	0.0	0.0	0.0	0.0	0.0
0.11000	TO	0.13000	0	0.0	0.0	0.0	0.0	0.0	0.0
0.13000	TO	0.15000	0	0.0	0.0	0.0	0.0	0.0	0.0
0.15000	TO	0.17000	0	0.0	0.0	0.0	0.0	0.0	0.0
0.17000	TO	0.19000	0	0.0	0.0	0.0	0.0	0.0	0.0
0.19000	TO	0.21000	0	0.0	0.0	0.0	0.0	0.0	0.0
0.21000	TO	0.23000	0	0.0	0.0	0.0	0.0	0.0	0.0
0.23000	TO	0.25000	0	0.0	0.0	0.0	0.0	0.0	0.0
0.25000	TO	0.27000	0	0.0	0.0	0.0	0.0	0.0	0.0
0.27000	TO	0.29000	0	0.0	0.0	0.0	0.0	0.0	0.0
0.29000	TO	0.31000	0	0.0	0.0	0.0	0.0	0.0	0.0
0.31000	TO	0.33000	0	0.0	0.0	0.0	0.0	0.0	0.0
0.33000	TO	0.35000	0	0.0	0.0	0.0	0.0	0.0	0.0
0.35000	TO	0.37000	0	0.0	0.0	0.0	0.0	0.0	0.0
0.37000	TO	0.39000	0	0.0	0.0	0.0	0.0	0.0	0.0
0.39000	TO	0.41000	0	0.0	0.0	0.0	0.0	0.0	0.0
0.41000	TO	0.43000	0	0.0	0.0	0.0	0.0	0.0	0.0

206

WEIGHTED AVERAGE MOMENTUM = 1.889 GEV/C

BEAM KINETIC ENERGY = 1.170 GEV

S = 5.721 (GEV)**2

Table II   The Differential Cross Sections for 1.75 GeV/c
< p < 2.00 GeV/c

CROSS SECTIONS FOR 2.00 GEV/C TO 2.25 GEV/C

ABS U BINS	NUMBER	ABSU $\|u\|\,(GeV/c)^2$	SIGMA $\frac{d\sigma}{du}$	ERROR	COSINE $\cos\Theta_{cm}$	SIGMA $\frac{d\sigma}{d\Omega}$	ERROR
0.0 TO 0.01000	0	0.0	0.0	0.0	0.0	0.0	0.0
0.01000 TO 0.02000	29	1.5881E-02	2.5851E 01	4.8004E 00	-9.8742E-01	5.2110E 00	9.6766E-01
0.02000 TO 0.03000	57	2.5185E-02	3.0147E 01	4.9562E 00	-9.8034E-01	6.1549E 00	1.0119E 00
0.03000 TO 0.04000	33	3.5563E-02	2.6899E 01	4.6826E 00	-9.7193E-01	5.4378E 00	9.4659E-01
0.04000 TO 0.05000	18	4.5037E-02	1.6100E 01	3.7947E 00	-9.6422E-01	3.2327E 00	7.6195E-01
0.05000 TO 0.07000	34	5.5344E-02	2.1541E 01	3.6942E 00	-9.5712E-01	4.4371E 00	7.6096E-01
0.07000 TO 0.09000	0	0.0	0.0	0.0	0.0	0.0	0.0
0.09000 TO 0.11000	0	0.0	0.0	0.0	0.0	0.0	0.0
0.11000 TO 0.13000	0	0.0	0.0	0.0	0.0	0.0	0.0
0.13000 TO 0.15000	0	0.0	0.0	0.0	0.0	0.0	0.0
0.15000 TO 0.17000	0	0.0	0.0	0.0	0.0	0.0	0.0
0.17000 TO 0.19000	0	0.0	0.0	0.0	0.0	0.0	0.0
0.19000 TO 0.21000	0	0.0	0.0	0.0	0.0	0.0	0.0
0.21000 TO 0.23000	0	0.0	0.0	0.0	0.0	0.0	0.0
0.23000 TO 0.25000	0	0.0	0.0	0.0	0.0	0.0	0.0
0.25000 TO 0.27000	0	0.0	0.0	0.0	0.0	0.0	0.0
0.27000 TO 0.29000	0	0.0	0.0	0.0	0.0	0.0	0.0
0.29000 TO 0.31000	0	0.0	0.0	0.0	0.0	0.0	0.0
0.31000 TO 0.33000	0	0.0	0.0	0.0	0.0	0.0	0.0
0.33000 TO 0.35000	0	0.0	0.0	0.0	0.0	0.0	0.0
0.35000 TO 0.37000	0	0.0	0.0	0.0	0.0	0.0	0.0
0.37000 TO 0.39000	0	0.0	0.0	0.0	0.0	0.0	0.0
0.39000 TO 0.41000	0	0.0	0.0	0.0	0.0	0.0	0.0
0.41000 TO 0.43000	0	0.0	0.0	0.0	0.0	0.0	0.0

151

WEIGHTED AVERAGE MOMENTUM = 2.098 GEV/C

BEAM KINETIC ENERGY = 1.359 GEV

S = 6.077 (GEV)**2

Table III   The Differential Cross Sections for 2.00 GeV/c < p < 2.25 GeV/c

CROSS SECTIONS FOR 2.25 GEV/C TO 2.50 GEV/C

ABS U BINS	NUMBER	ABSU $\|u\|\ (GeV/c)^2$	SIGMA $\frac{d\sigma}{du}$	ERROR	COSINE $\cos\theta_{cm}$	SIGMA $\frac{d\sigma}{d\Omega}$	ERROR
0.0 TO 0.01000	0	0.0	0.0	0.0	0.0	0.0	0.0
0.01000 TO 0.02000	31	1.4630E-02	2.1392E 01	3.8421E 00	-9.9038E-01	5.1813E 00	9.3058E-01
0.02000 TO 0.03000	27	2.5261E-02	1.7679E 01	3.4023E 00	-9.8313E-01	4.2227E 00	8.1266E-01
0.03000 TO 0.04000	23	3.4886E-02	1.5557E 01	3.2438E 00	-9.7708E-01	3.7789E 00	7.8796E-01
0.04000 TO 0.05000	18	4.4242E-02	1.1368E 01	2.6794E 00	-9.7067E-01	2.7316E 00	6.4384E-01
0.05000 TO 0.07000	51	6.0881E-02	1.5731E 01	2.2027E 00	-9.5957E-01	3.7761E 00	5.2876E-01
0.07000 TO 0.09000	34	7.9129E-02	1.1137E 01	1.9099E 00	-9.4731E-01	2.6701E 00	4.5792E-01
0.09000 TO 0.11000	34	9.9903E-02	1.2695E 01	2.1772E 00	-9.3420E-01	3.0727E 00	5.2696E-01
0.11000 TO 0.13000	25	1.2120E-01	1.0876E 01	2.1352E 00	-9.2015E-01	2.5838E 00	5.1676E-01
0.13000 TO 0.15000	0	0.0	0.0	0.0	0.0	0.0	0.0
0.15000 TO 0.17000	0	0.0	0.0	0.0	0.0	0.0	0.0
0.17000 TO 0.19000	0	0.0	0.0	0.0	0.0	0.0	0.0
0.19000 TO 0.21000	0	0.0	0.0	0.0	0.0	0.0	0.0
0.21000 TO 0.23000	0	0.0	0.0	0.0	0.0	0.0	0.0
0.23000 TO 0.25000	0	0.0	0.0	0.0	0.0	0.0	0.0
0.25000 TO 0.27000	0	0.0	0.0	0.0	0.0	0.0	0.0
0.27000 TO 0.29000	0	0.0	0.0	0.0	0.0	0.0	0.0
0.29000 TO 0.31000	0	0.0	0.0	0.0	0.0	0.0	0.0
0.31000 TO 0.33000	0	0.0	0.0	0.0	0.0	0.0	0.0
0.33000 TO 0.35000	0	0.0	0.0	0.0	0.0	0.0	0.0
0.35000 TO 0.37000	0	0.0	0.0	0.0	0.0	0.0	0.0
0.37000 TO 0.39000	0	0.0	0.0	0.0	0.0	0.0	0.0
0.39000 TO 0.41000	0	0.0	0.0	0.0	0.0	0.0	0.0
0.41000 TO 0.43000	0	0.0	0.0	0.0	0.0	0.0	0.0

WEIGHTED AVERAGE MOMENTUM = 2.374 GEV/C

BEAM KINETIC ENERGY = 1.614 GEV

S = 6.555 (GEV)**2

243

Table IV The Differential Cross Sections for 2.25 GeV/c < p < 2.50 GeV/c

Fig. 34 The Differential Cross Sections for 2.25 GeV/c
< p < 2.50 GeV/c

CROSS SECTIONS FOR 2.50 GEV/C TO 2.75 GEV/C

ABS U BINS	NUMBER	ABSU $|u|\ (GeV/c)^2$	SIGMA $\frac{d\sigma}{du}$	ERROR	COSINE $\cos\theta_{cm}$	SIGMA $\frac{d\sigma}{d\Omega}$	ERROR
0.0 TO 0.01000	0	0.0	0.0	0.0	0.0	0.0	0.0
0.01000 TO 0.02000	25	1.4620E-02	9.6193E 00	1.9239E 00	-9.9164E-01	2.6822E 00	5.3643E-01
0.02000 TO 0.03000	16	2.4339E-02	6.2032E 00	1.5508E 00	-9.8583E-01	1.6961E 00	4.2403E-01
0.03000 TO 0.04000	18	3.5785E-02	6.8966E 00	1.6253E 00	-9.7915E-01	1.8852E 00	4.4435E-01
0.04000 TO 0.05000	22	4.5988E-02	8.1731E 00	1.7425E 00	-9.7308E-01	2.2255E 00	4.7448E-01
0.05000 TO 0.07000	49	5.9081E-02	9.0985E 00	1.2998E 00	-9.6554E-01	2.4883E 00	3.5547E-01
0.07000 TO 0.09000	47	7.8667E-02	9.8452E 00	1.4361E 00	-9.5425E-01	2.6989E 00	3.9368E-01
0.09000 TO 0.11000	39	1.0039E-01	9.3892E 00	1.5035E 00	-9.4107E-01	2.5503E 00	4.0837E-01
0.11000 TO 0.13000	37	1.2012E-01	9.0645E 00	1.4902E 00	-9.3004E-01	2.4806E 00	4.0781E-01
0.13000 TO 0.15000	11	1.3573E-01	5.2470E 00	1.5820E 00	-9.2127E-01	1.4416E 00	4.3465E-01
0.15000 TO 0.17000	0	0.0	0.0	0.0	0.0	0.0	0.0
0.17000 TO 0.19000	0	0.0	0.0	0.0	0.0	0.0	0.0
0.19000 TO 0.21000	0	0.0	0.0	0.0	0.0	0.0	0.0
0.21000 TO 0.23000	0	0.0	0.0	0.0	0.0	0.0	0.0
0.23000 TO 0.25000	0	0.0	0.0	0.0	0.0	0.0	0.0
0.25000 TO 0.27000	0	0.0	0.0	0.0	0.0	0.0	0.0
0.27000 TO 0.29000	0	0.0	0.0	0.0	0.0	0.0	0.0
0.29000 TO 0.31000	0	0.0	0.0	0.0	0.0	0.0	0.0
0.31000 TO 0.33000	0	0.0	0.0	0.0	0.0	0.0	0.0
0.33000 TO 0.35000	0	0.0	0.0	0.0	0.0	0.0	0.0
0.35000 TO 0.37000	0	0.0	0.0	0.0	0.0	0.0	0.0
0.37000 TO 0.39000	0	0.0	0.0	0.0	0.0	0.0	0.0
0.39000 TO 0.41000	0	0.0	0.0	0.0	0.0	0.0	0.0
0.41000 TO 0.43000	0	0.0	0.0	0.0	0.0	0.0	0.0

WEIGHTED AVERAGE MOMENTUM = 2.610 GEV/C

BEAM KINETIC ENERGY = 1.835 GEV

S = 6.969 (GEV)**2

264

Table V The Differential Cross Sections for 2.50 GeV/c < p < 2.75 GeV/c

Fig. 35 The Differential Cross Sections for 2.50 GeV/c
< p < 2.75 GeV/c

CROSS SECTIONS FOR 2.75 GEV/C TO 3.00 GEV/C

ABS U BINS		NUMBER	ABSU $\|u\|$ $(GeV/c)^2$	SIGMA $\frac{d\sigma}{du}$	ERROR	COSINE $\cos\theta_{cm}$	SIGMA $\frac{d\sigma}{d\Omega}$	ERROR
0.0	TO 0.01000	0	0.0	0.0	0.0	0.0	0.0	0.0
0.01000	TO 0.02000	34	1.5261E-02	9.7543E 00	1.6728E 00	-9.9222E-01	3.0484E 00	5.2279E-01
0.02000	TO 0.03000	26	2.5396E-02	7.4527E 00	1.4616E 00	-9.8704E-01	2.3253E 00	4.5603E-01
0.03000	TO 0.04000	18	3.4500E-02	4.5185E 00	1.0650E 00	-9.8255E-01	1.4225E 00	3.3529E-01
0.04000	TO 0.05000	21	4.5064E-02	4.7658E 00	1.0400E 00	-9.7686E-01	1.4790E 00	3.2274E-01
0.05000	TO 0.07000	36	6.2109E-02	4.1785E 00	6.9642E-01	-9.6833E-01	1.3047E 00	2.1745E-01
0.07000	TO 0.09000	36	8.0092E-02	4.6080E 00	7.6800E-01	-9.5899E-01	1.4327E 00	2.3878E-01
0.09000	TO 0.11000	31	1.0124E-01	4.3501E 00	7.8130E-01	-9.4791E-01	1.3481E 00	2.4213E-01
0.11000	TO 0.13000	20	1.1941E-01	2.9298E 00	6.5513E-01	-9.3937E-01	9.1917E-01	2.0553E-01
0.13000	TO 0.15000	22	1.3758E-01	3.7488E 00	7.9925E-01	-9.2914E-01	1.1595E 00	2.4721E-01
0.15000	TO 0.17000	19	1.6112E-01	3.9780E 00	9.1261E-01	-9.1788E-01	1.2430E 00	2.8518E-01
0.17000	TO 0.19000	11	1.7926E-01	2.6201E 00	7.9000E-01	-9.0808E-01	8.1381E-01	2.4537E-01
0.19000	TO 0.21000	0	0.0	0.0	0.0	0.0	0.0	0.0
0.21000	TO 0.23000	0	0.0	0.0	0.0	0.0	0.0	0.0
0.23000	TO 0.25000	0	0.0	0.0	0.0	0.0	0.0	0.0
0.25000	TO 0.27000	0	0.0	0.0	0.0	0.0	0.0	0.0
0.27000	TO 0.29000	0	0.0	0.0	0.0	0.0	0.0	0.0
0.29000	TO 0.31000	0	0.0	0.0	0.0	0.0	0.0	0.0
0.31000	TO 0.33000	0	0.0	0.0	0.0	0.0	0.0	0.0
0.33000	TO 0.35000	0	0.0	0.0	0.0	0.0	0.0	0.0
0.35000	TO 0.37000	0	0.0	0.0	0.0	0.0	0.0	0.0
0.37000	TO 0.39000	0	0.0	0.0	0.0	0.0	0.0	0.0
0.39000	TO 0.41000	0	0.0	0.0	0.0	0.0	0.0	0.0
0.41000	TO 0.43000	0	0.0	0.0	0.0	0.0	0.0	0.0

274

WEIGHTED AVERAGE MOMENTUM = 2.878 GEV/C

BEAM KINETIC ENERGY = 2.088 GEV

S = 7.444 (GEV)**2

Table VI The Differential Cross Sections for 2.75 GeV/c < p < 3.00 GeV/c
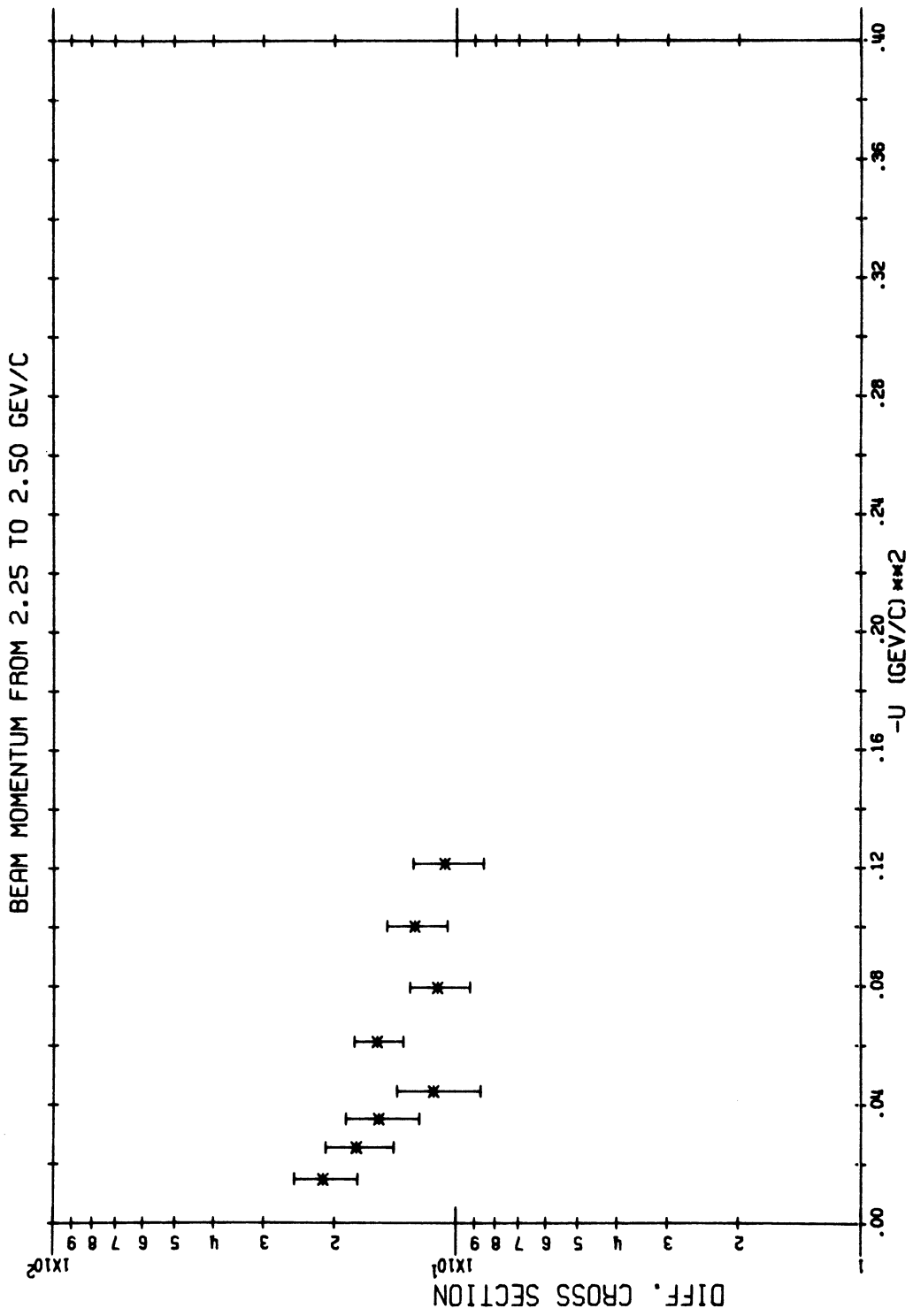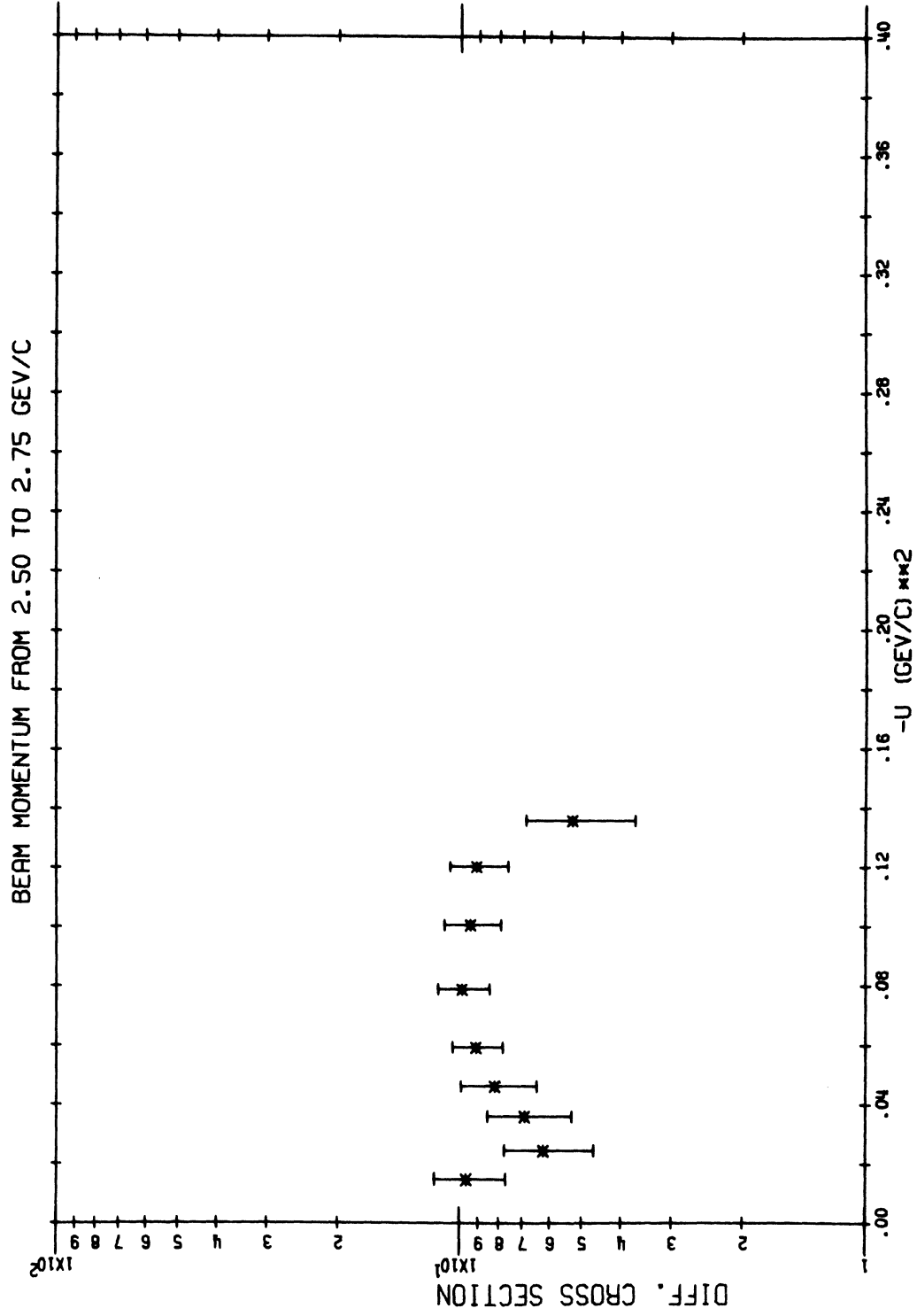
Fig. 36 The Differential Cross Sections for 2.75 GeV/c
< p < 3.00 GeV/c

CROSS SECTIONS FOR 3.00 GEV/C TO 3.25 GEV/C

ABS U BINS	NUMBER	ABSU $\|u\|(GeV/c)^2$	SIGMA $\frac{d\sigma}{du}$	ERROR	COSINE $\cos\theta_{cm}$	SIGMA $\frac{d\sigma}{d\Omega}$	ERROR
0.0 TO 0.01000	0	0.0	0.0	0.0	0.0	0.0	0.0
0.01000 TO 0.02000	23	1.4315E-02	6.0243E 00	1.2562E 00	-9.9332E-01	2.0630E 00	4.3017E-01
0.02000 TO 0.03000	20	2.5319E-02	5.0345E 00	1.1257E 00	-9.8835E-01	1.7430E 00	3.8975E-01
0.03000 TO 0.04000	16	3.5533E-02	3.4238E 00	8.5595E-01	-9.8382E-01	1.1983E 00	2.9958E-01
0.04000 TO 0.05000	23	4.4789E-02	4.6456E 00	9.6868E-01	-9.7952E-01	1.6183E 00	3.3743E-01
0.05000 TO 0.07000	38	5.9665E-02	3.9003E 00	6.3270E-01	-9.7228E-01	1.3381E 00	2.1707E-01
0.07000 TO 0.09000	32	8.0712E-02	3.5586E 00	6.3085E-01	-9.6310E-01	1.2434E 00	2.1981E-01
0.09000 TO 0.11000	31	9.9658E-02	3.7956E 00	6.8172E-01	-9.5442E-01	1.3216E 00	2.3736E-01
0.11000 TO 0.13000	35	1.2000E-01	4.5538E 00	7.6974E-01	-9.4471E-01	1.5743E 00	2.6611E-01
0.13000 TO 0.15000	18	1.3855E-01	2.5108E 00	5.9180E-01	-9.3610E-01	8.6699E-01	2.0435E-01
0.15000 TO 0.17000	18	1.5904E-01	2.5844E 00	6.0914E-01	-9.2681E-01	8.9440E-01	2.1081E-01
0.17000 TO 0.19000	13	1.8077E-01	1.9543E 00	5.4202E-01	-9.1758E-01	6.8260E-01	1.8932E-01
0.19000 TO 0.21000	16	1.9976E-01	3.7734E 00	9.4336E-01	-9.0833E-01	1.3094E 00	3.2735E-01
0.21000 TO 0.23000	0	0.0	0.0	0.0	0.0	0.0	0.0
0.23000 TO 0.25000	0	0.0	0.0	0.0	0.0	0.0	0.0
0.25000 TO 0.27000	0	0.0	0.0	0.0	0.0	0.0	0.0
0.27000 TO 0.29000	0	0.0	0.0	0.0	0.0	0.0	0.0
0.29000 TO 0.31000	0	0.0	0.0	0.0	0.0	0.0	0.0
0.31000 TO 0.33000	0	0.0	0.0	0.0	0.0	0.0	0.0
0.33000 TO 0.35000	0	0.0	0.0	0.0	0.0	0.0	0.0
0.35000 TO 0.37000	0	0.0	0.0	0.0	0.0	0.0	0.0
0.37000 TO 0.39000	0	0.0	0.0	0.0	0.0	0.0	0.0
0.39000 TO 0.41000	0	0.0	0.0	0.0	0.0	0.0	0.0
0.41000 TO 0.43000	0	0.0	0.0	0.0	0.0	0.0	0.0

283

WEIGHTED AVERAGE MOMENTUM = 3.121 GEV/C

BEAM KINETIC ENERGY = 2.320 GEV

S = 7.879 (GEV)**2

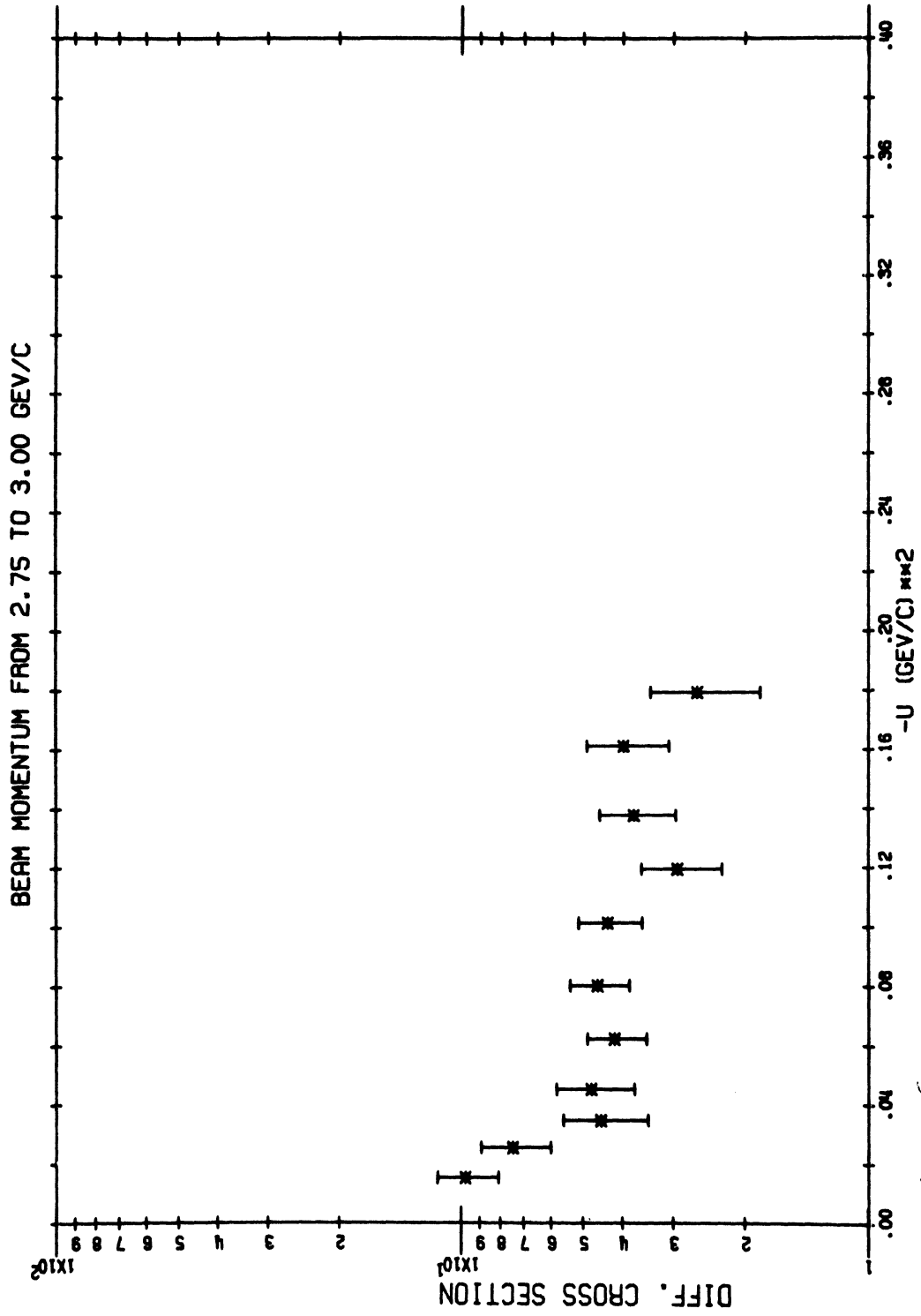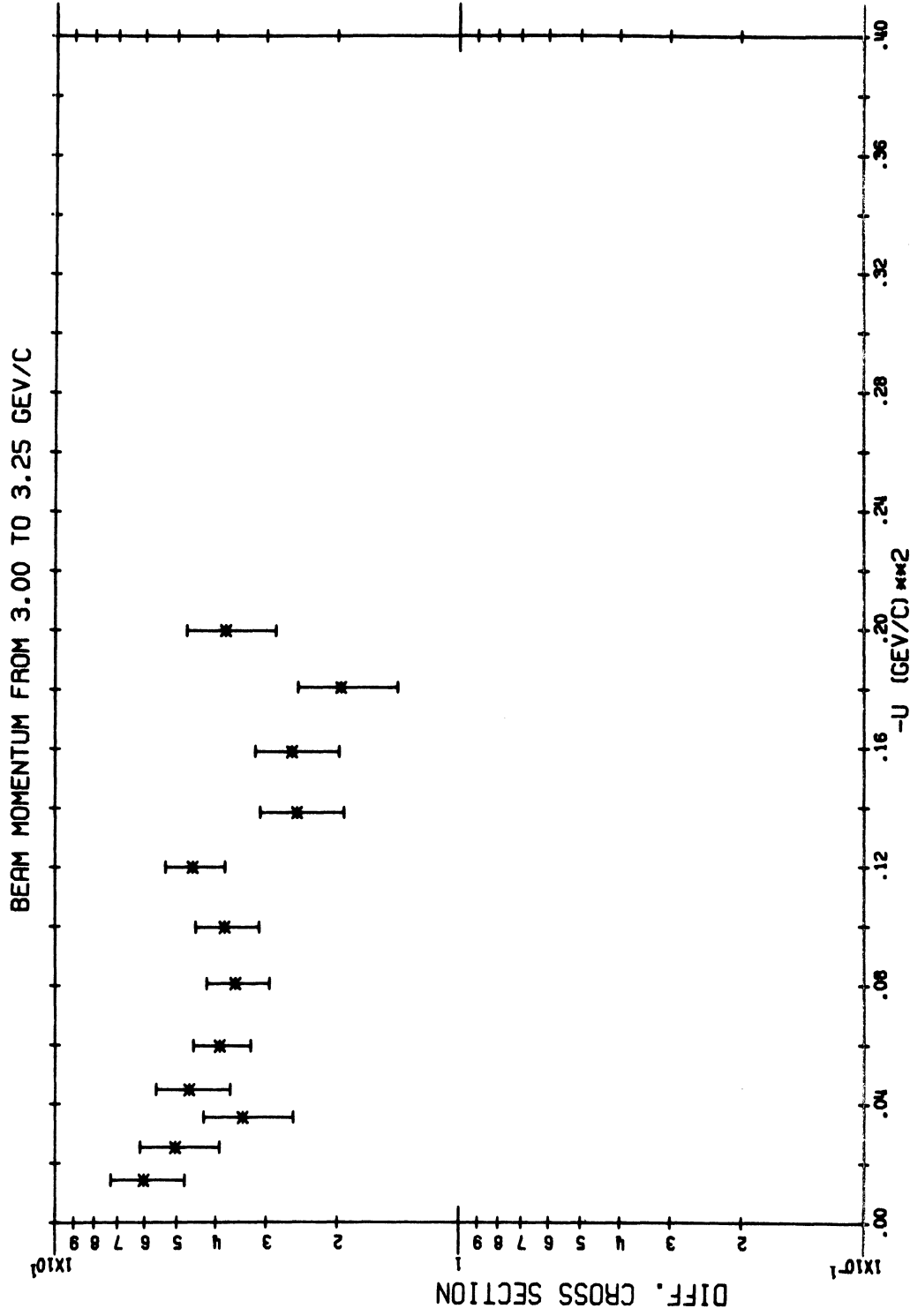Table VII The Differential Cross Sections for 3.00 GeV/c < p < 3.25 GeV/c

Fig. 37 The Differential Cross Sections for 3.00 GeV/c < p < 3.25 GeV/c

CROSS SECTIONS FOR 3.25 GEV/C TO 4.25 GEV/C

ABS U BINS		NUMBER	ABSU $\|u\|$ $(GeV/c)^2$	SIGMA $\frac{d\sigma}{du}$	ERROR	COSINE $\cos\theta_{cm}$	SIGMA $\frac{d\sigma}{d\Omega}$	ERROR
0.0	TO 0.01000	0	0.0	0.0	0.0	0.0	0.0	0.0
0.01000	TO 0.02000	88	1.4843E-02	3.3580E 00	3.5803E-01	-9.9445E-01	1.4416E 00	1.5368E-01
0.02000	TO 0.03000	88	2.4913E-02	3.3892E 00	3.6129E-01	-9.9064E-01	1.4420E 00	1.5372E-01
0.03000	TO 0.04000	81	3.4751E-02	2.8158E 00	3.1287E-01	-9.8691E-01	1.2004E 00	1.3338E-01
0.04000	TO 0.05000	96	4.4818E-02	2.8683E 00	2.9275E-01	-9.8307E-01	1.2192E 00	1.2443E-01
0.05000	TO 0.07000	142	5.9905E-02	2.1908E 00	1.8384E-01	-9.7735E-01	9.3069E-01	7.8102E-02
0.07000	TO 0.09000	121	7.9910E-02	1.9518E 00	1.7743E-01	-9.7048E-01	8.4903E-01	7.7185E-02
0.09000	TO 0.11000	124	1.0033E-01	2.4253E 00	2.1780E-01	-9.6211E-01	1.0298E 00	9.2483E-02
0.11000	TO 0.13000	85	1.1989E-01	1.7146E 00	1.8597E-01	-9.5485E-01	7.3354E-01	7.9564E-02
0.13000	TO 0.15000	69	1.4004E-01	1.4157E 00	1.7043E-01	-9.4715E-01	6.0338E-01	7.2638E-02
0.15000	TO 0.17000	84	1.6021E-01	1.3957E 00	1.7447E-01	-9.3964E-01	5.9589E-01	7.4486E-02
0.17000	TO 0.19000	62	1.8058E-01	1.4423E 00	1.8317E-01	-9.3133E-01	6.0908E-01	7.7354E-02
0.19000	TO 0.21000	45	1.9959E-01	9.9714E-01	1.4864E-01	-9.2509E-01	4.2592E-01	6.3493E-02
0.21000	TO 0.23000	39	2.1927E-01	8.3243E-01	1.3330E-01	-9.1981E-01	3.6483E-01	5.8419E-02
0.23000	TO 0.25000	22	2.3820E-01	5.5488E-01	1.3962E-01	-9.1202E-01	2.8425E-01	6.0603E-02
0.25000	TO 0.27000	0	0.0	0.0	0.0	0.0	0.0	0.0
0.27000	TO 0.29000	0	0.0	0.0	0.0	0.0	0.0	0.0
0.29000	TO 0.31000	0	0.0	0.0	0.0	0.0	0.0	0.0
0.31000	TO 0.33000	0	0.0	0.0	0.0	0.0	0.0	0.0
0.33000	TO 0.35000	0	0.0	0.0	0.0	0.0	0.0	0.0
0.35000	TO 0.37000	0	0.0	0.0	0.0	0.0	0.0	0.0
0.37000	TO 0.39000	0	0.0	0.0	0.0	0.0	0.0	0.0
0.39000	TO 0.41000	0	0.0	0.0	0.0	0.0	0.0	0.0
0.41000	TO 0.43000	0	0.0	0.0	0.0	0.0	0.0	0.0

1126

WEIGHTED AVERAGE MOMENTUM = 3.682 GEV/C

BEAM KINETIC ENERGY = 2.861 GEV

S = 8.894 (GEV)**2

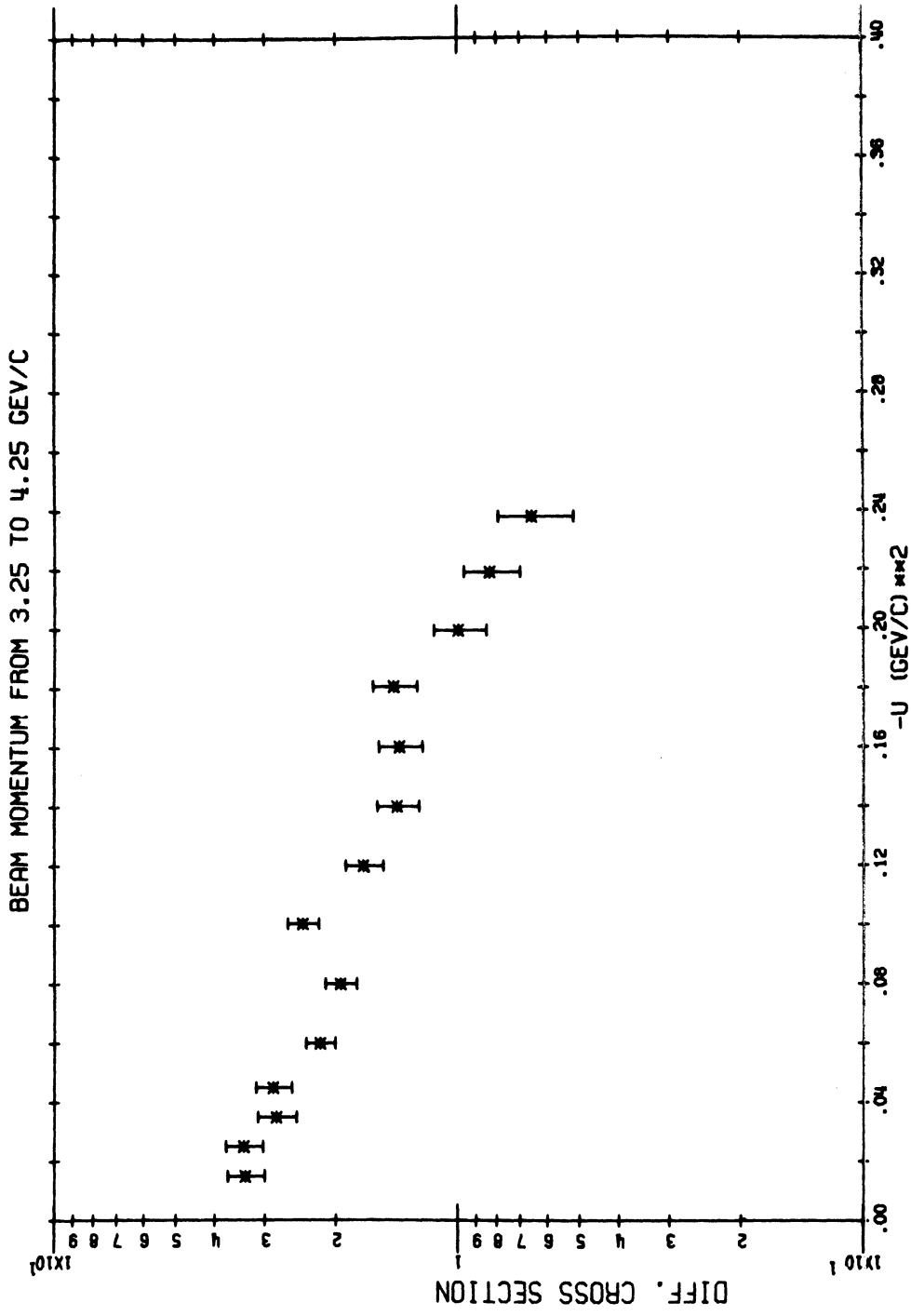Table VIII   The Differential Cross Sections for 3.25 GeV/c
$< p <$ 4.25 GeV/c

Fig. 38 The Differential Cross Sections for 3.25 GeV/c
< p < 4.25 GeV/c

CROSS SECTIONS FOR 4.25 GEV/C TO 5.25 GEV/C

ABS U BINS	NUMBER	ABSU $\|u\|\ (GeV/c)^2$	SIGMA $\frac{d\sigma}{du}$	ERROR	COSINE $\cos\theta_{cm}$	SIGMA $\frac{d\sigma}{d\Omega}$	ERROR
0.0 TO 0.01000	0	0.0	0.0	0.0	0.0	0.0	0.0
0.01000 TO 0.02000	101	1.4872E-02	2.6516E 00	2.6385E-01	-9.9597E-01	1.5499E 00	1.5422E-01
0.02000 TO 0.03000	87	2.5406E-02	2.1744E 00	2.3312E-01	-9.9305E-01	1.2692E 00	1.3608E-01
0.03000 TO 0.04000	80	3.5344E-02	1.7426E 00	1.9483E-01	-9.9012E-01	9.9759E-01	1.1153E-01
0.04000 TO 0.05000	84	4.5050E-02	1.5999E 00	1.7457E-01	-9.8746E-01	9.1956E-01	1.0033E-01
0.05000 TO 0.07000	154	5.9878E-02	1.5292E 00	1.2322E-01	-9.8354E-01	8.9002E-01	7.1720E-02
0.07000 TO 0.09000	148	7.9611E-02	1.6433E 00	1.3508E-01	-9.7805E-01	9.5389E-01	7.8409E-02
0.09000 TO 0.11000	93	9.9887E-02	1.1471E 00	1.1895E-01	-9.7247E-01	6.6652E-01	6.9115E-02
0.11000 TO 0.13000	80	1.1992E-01	9.8995E-01	1.1068E-01	-9.6755E-01	5.8473E-01	6.5375E-02
0.13000 TO 0.15000	62	1.3960E-01	7.8621E-01	9.9849E-02	-9.6181E-01	4.6032E-01	5.8461E-02
0.15000 TO 0.17000	82	1.5981E-01	1.1238E 00	1.2410E-01	-9.5550E-01	6.4535E-01	7.1267E-02
0.17000 TO 0.19000	63	1.8041E-01	8.6380E-01	1.0883E-01	-9.5028E-01	5.0147E-01	6.3179E-02
0.19000 TO 0.21000	65	1.9992E-01	8.8407E-01	1.0965E-01	-9.4501E-01	5.1416E-01	6.3774E-02
0.21000 TO 0.23000	50	2.1966E-01	7.0698E-01	9.9982E-02	-9.3961E-01	4.1098E-01	5.8122E-02
0.23000 TO 0.25000	34	2.3937E-01	4.8519E-01	8.3210E-02	-9.3432E-01	2.8280E-01	4.8499E-02
0.25000 TO 0.27000	42	2.5992E-01	6.6652E-01	1.0285E-01	-9.2769E-01	3.8296E-01	5.9092E-02
0.27000 TO 0.29000	31	2.8108E-01	5.7320E-01	1.0295E-01	-9.2524E-01	3.4407E-01	6.1797E-02
0.29000 TO 0.31000	0	0.0	0.0	0.0	0.0	0.0	0.0
0.31000 TO 0.33000	0	0.0	0.0	0.0	0.0	0.0	0.0
0.33000 TO 0.35000	0	0.0	0.0	0.0	0.0	0.0	0.0
0.35000 TO 0.37000	0	0.0	0.0	0.0	0.0	0.0	0.0
0.37000 TO 0.39000	0	0.0	0.0	0.0	0.0	0.0	0.0
0.39000 TO 0.41000	0	0.0	0.0	0.0	0.0	0.0	0.0
0.41000 TO 0.43000	0	0.0	0.0	0.0	0.0	0.0	0.0

1256

WEIGHTED AVERAGE MOMENTUM = 4.739 GEV/C

BEAM KINETIC ENERGY = 3.891 GEV

S = 10.828 (GEV)**2

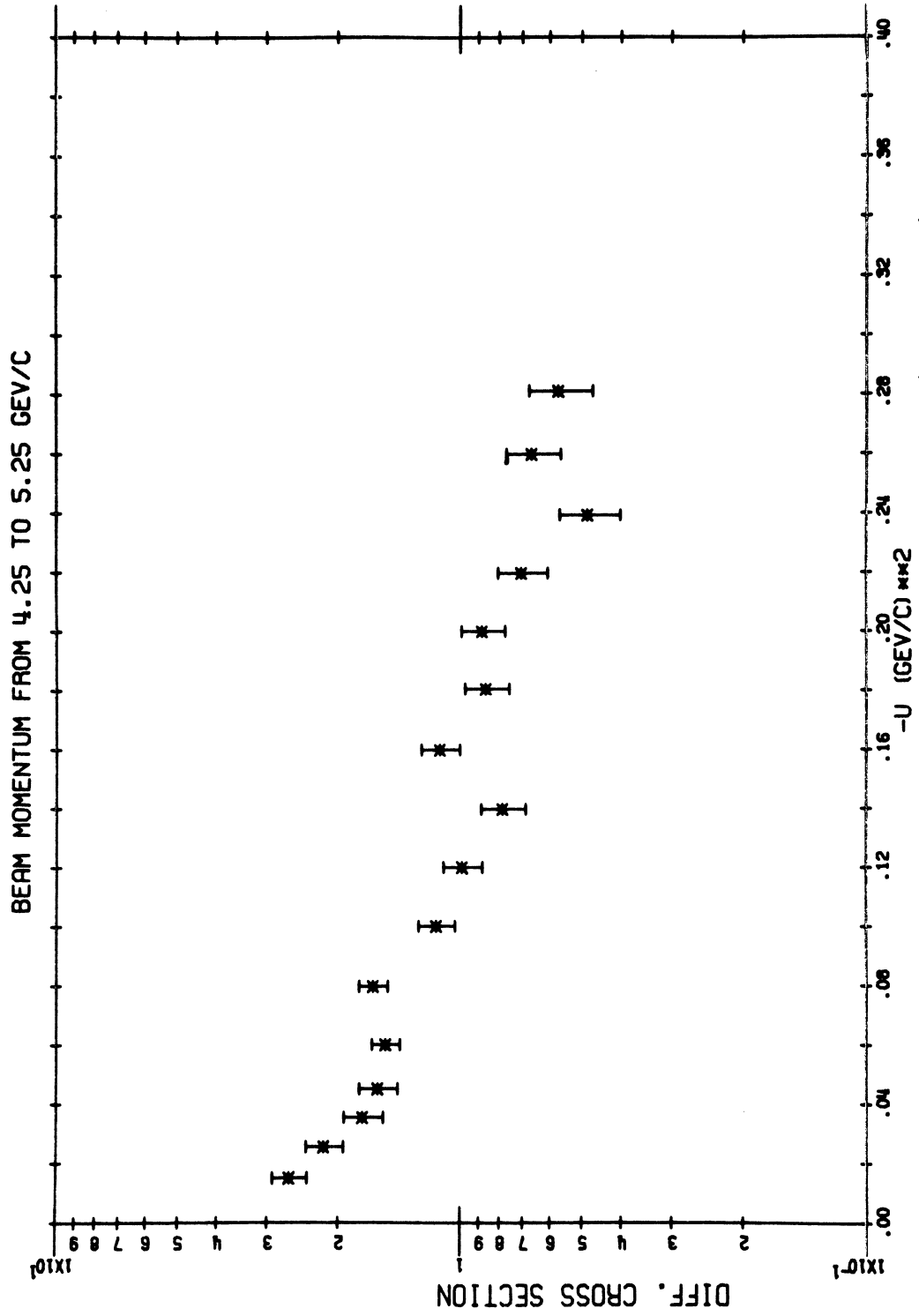Table IX   The Differential Cross Sections for 4.25 GeV/c < p < 5.25 GeV/c

Fig. 39 The Differential Cross Sections for 4.25 GeV/c
< p < 5.25 GeV/c

CROSS SECTIONS FOR 5.25 GEV/C TO 6.25 GEV/C

ABS U BINS	NUMBER	ABSU $\mid u \mid$ (GeV/c)²	SIGMA $\frac{d\sigma}{du}$	ERROR	COSINE $\cos\theta_{cm}$	SIGMA $\frac{d\sigma}{d\Omega}$	ERROR
0.0 TO 0.01000	0	0.0	0.0	0.0	0.0	0.0	0.0
0.01000 TO 0.02000	113	1.4777E-02	1.6662E 00	1.5674E-01	-9.9695E-01	1.2157E 00	1.1436E-01
0.02000 TO 0.03000	106	2.4323E-02	1.5096E 00	1.4662E-01	-9.9469E-01	1.0954E 00	1.0639E-01
0.03000 TO 0.04000	90	3.5220E-02	1.2203E 00	1.2864E-01	-9.9227E-01	8.8790E-01	9.3593E-02
0.04000 TO 0.05000	84	4.4571E-02	1.0265E 00	1.1200E-01	-9.9024E-01	7.4879E-01	8.1699E-02
0.05000 TO 0.07000	162	6.0035E-02	1.0248E 00	8.0518E-02	-9.8676E-01	7.4164E-01	5.8269E-02
0.07000 TO 0.09000	158	8.0063E-02	1.0907E 00	8.6768E-02	-9.8251E-01	7.9725E-01	6.3426E-02
0.09000 TO 0.11000	112	9.9490E-02	8.7118E-01	8.2319E-02	-9.7805E-01	6.3020E-01	5.9549E-02
0.11000 TO 0.13000	91	1.1977E-01	7.7280E-01	8.1011E-02	-9.7373E-01	5.6256E-01	5.8972E-02
0.13000 TO 0.15000	73	1.4023E-01	6.7148E-01	7.8590E-02	-9.6908E-01	4.8657E-01	5.6948E-02
0.15000 TO 0.17000	77	1.5990E-01	7.4100E-01	8.4445E-02	-9.6448E-01	5.3278E-01	6.0716E-02
0.17000 TO 0.19000	60	1.8031E-01	5.6772E-01	7.3292E-02	-9.6041E-01	4.1311E-01	5.3332E-02
0.19000 TO 0.21000	42	1.9876E-01	3.8193E-01	5.8933E-02	-9.5720E-01	2.8311E-01	4.3685E-02
0.21000 TO 0.23000	58	2.1902E-01	5.4119E-01	7.1062E-02	-9.5223E-01	3.9619E-01	5.2022E-02
0.23000 TO 0.25000	46	2.4066E-01	4.5047E-01	6.6418E-02	-9.4646E-01	3.2331E-01	4.7670E-02
0.25000 TO 0.27000	44	2.5831E-01	4.3230E-01	6.5171E-02	-9.4391E-01	3.1785E-01	4.7918E-02
0.27000 TO 0.29000	38	2.8066E-01	4.0816E-01	6.6212E-02	-9.3801E-01	2.9517E-01	4.7883E-02
0.29000 TO 0.31000	15	2.9823E-01	1.8956E-01	4.8945E-02	-9.3547E-01	1.3988E-01	3.6116E-02
0.31000 TO 0.33000	0	0.0	0.0	0.0	0.0	0.0	0.0
0.33000 TO 0.35000	0	0.0	0.0	0.0	0.0	0.0	0.0
0.35000 TO 0.37000	0	0.0	0.0	0.0	0.0	0.0	0.0
0.37000 TO 0.39000	0	0.0	0.0	0.0	0.0	0.0	0.0
0.39000 TO 0.41000	0	0.0	0.0	0.0	0.0	0.0	0.0
0.41000 TO 0.43000	0	0.0	0.0	0.0	0.0	0.0	0.0

1369

WEIGHTED AVERAGE MOMENTUM = 5.734 GEV/C

BEAM KINETIC ENERGY = 4.870 GEV

S = 12.666 (GEV)**2

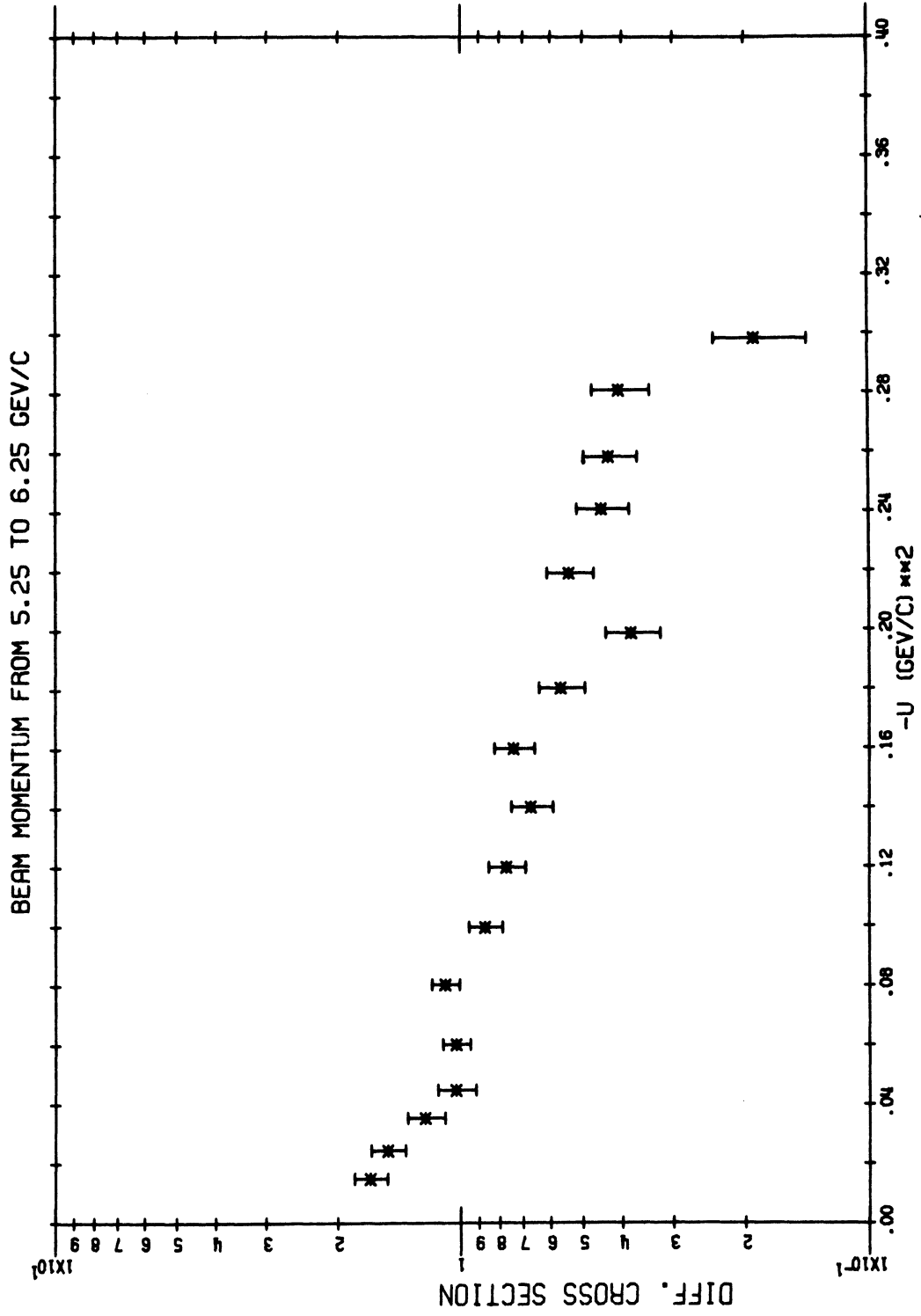Table X   The Differential Cross Sections for 5.25 GeV/c
< p < 6.25 GeV/c

Fig. 40 The Differential Cross Sections for 5.25 GeV/c
< p < 6.25 GeV/c

CROSS SECTIONS FOR 6.25 GEV/C TO 7.20 GEV/C

ABS U BINS		NUMBER	ABSU $\|u\|\ (GeV/c)^2$	SIGMA $\frac{d\sigma}{du}$	ERROR	COSINE $\cos\theta_{cm}$	SIGMA $\frac{d\sigma}{d\Omega}$	ERROR
0.0	TO 0.01000	0	0.0	0.0	0.0	0.0	0.0	0.0
0.01000	TO 0.02000	82	1.4948E-02	2.6741E 00	2.9530E-01	-9.9742E-01	2.3459E 00	2.5906E-01
0.02000	TO 0.03000	62	2.4824E-02	1.6324E 00	2.0732E-01	-9.9573E-01	1.4185E 00	1.8015E-01
0.03000	TO 0.04000	56	3.4579E-02	1.4689E 00	1.9629E-01	-9.9377E-01	1.2798E 00	1.7102E-01
0.04000	TO 0.05000	50	4.4412E-02	1.1953E 00	1.6904E-01	-9.9186E-01	1.0395E 00	1.4701E-01
0.05000	TO 0.07000	85	5.9324E-02	9.2305E-01	1.0012E-01	-9.8907E-01	7.9920E-01	8.6686E-02
0.07000	TO 0.09000	69	8.0258E-02	8.2718E-01	9.9581E-02	-9.8526E-01	7.1817E-01	8.6457E-02
0.09000	TO 0.11000	70	9.9032E-02	8.7873E-01	1.0503E-01	-9.8160E-01	7.5470E-01	9.0204E-02
0.11000	TO 0.13000	43	1.2076E-01	6.0122E-01	9.1685E-02	-9.7782E-01	5.2189E-01	7.9587E-02
0.13000	TO 0.15000	31	1.3913E-01	3.9057E-01	7.0149E-02	-9.7381E-01	3.3064E-01	5.9384E-02
0.15000	TO 0.17000	37	1.6069E-01	4.9392E-01	8.1199E-02	-9.6980E-01	4.1892E-01	6.8870E-02
0.17000	TO 0.19000	42	1.8146E-01	6.2178E-01	9.5943E-02	-9.6646E-01	5.3627E-01	8.2748E-02
0.19000	TO 0.21000	26	2.0030E-01	4.1183E-01	8.0767E-02	-9.6347E-01	3.6030E-01	7.0661E-02
0.21000	TO 0.23000	25	2.1902E-01	4.1317E-01	8.2634E-02	-9.6004E-01	3.6113E-01	7.2226E-02
0.23000	TO 0.25000	23	2.3760E-01	3.6462E-01	7.6029E-02	-9.5635E-01	3.1626E-01	6.5944E-02
0.25000	TO 0.27000	16	2.6038E-01	2.8273E-01	7.0683E-02	-9.5261E-01	2.4759E-01	6.1897E-02
0.27000	TO 0.29000	16	2.7807E-01	2.8650E-01	7.1625E-02	-9.4887E-01	2.4884E-01	6.2211E-02
0.29000	TO 0.31000	13	3.0174E-01	2.4088E-01	6.6808E-02	-9.4389E-01	2.0650E-01	5.7272E-02
0.31000	TO 0.33000	0	0.0	0.0	0.0	0.0	0.0	0.0
0.33000	TO 0.35000	0	0.0	0.0	0.0	0.0	0.0	0.0
0.35000	TO 0.37000	0	0.0	0.0	0.0	0.0	0.0	0.0
0.37000	TO 0.39000	0	0.0	0.0	0.0	0.0	0.0	0.0
0.39000	TO 0.41000	0	0.0	0.0	0.0	0.0	0.0	0.0
0.41000	TO 0.43000	0	0.0	0.0	0.0	0.0	0.0	0.0

746

WEIGHTED AVERAGE MOMENTUM = 6.689 GEV/C

BEAM KINETIC ENERGY = 5.816 GEV

S = 14.439 (GEV)**2

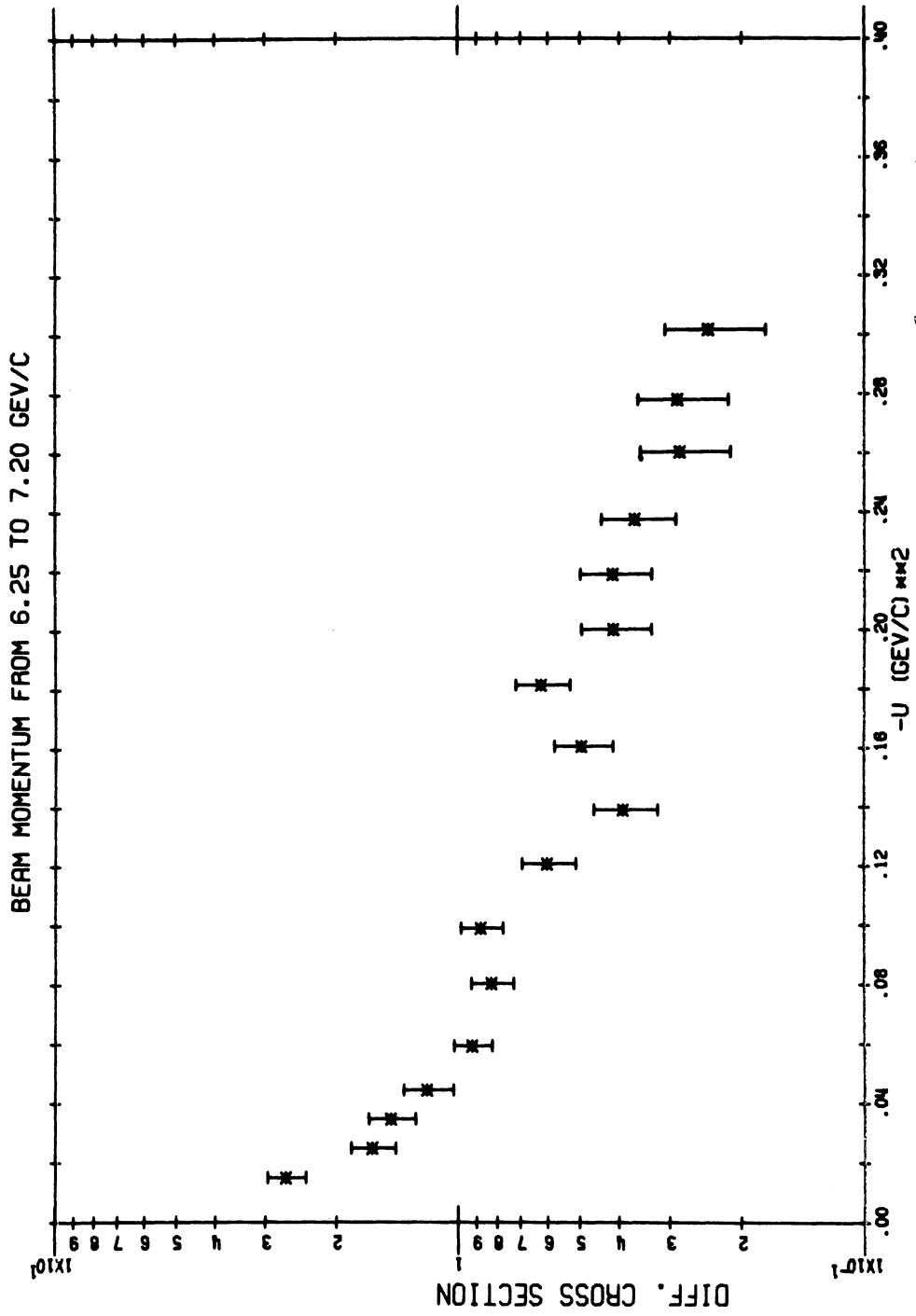Table XI   The Differential Cross Sections for 6.25 GeV/c < p < 7.20 GeV/c

Fig. 41 The Differential Cross Sections for 6.25 GeV/c
< p < 7.20 GeV/c

LIST OF REFERENCES

1. H. Palevsky, J. A. Moore, R. L. Stearns, H. R. Muether, R. J. Sutter, R. E. Chrien, A. P. Jain, and K. Otnes, Physical Review Letters 9, 509 (1962).

2. M. N. Kreisler, F. Martin, M. L. Perl, M. J. Longo, and S. T. Powell,III, Physical Review Letters 16, 1217 (1966); M. N. Kreisler, Report No. SLAC-66, Stanford Linear Accelerator Center, Stanford University, Stanford, California (1966); J. Cox, M. L. Perl, Michael N. Kreisler, Michael J. Longo, and S. T. Powell,III, Physical Review Letters 21, 641 (1968); J. Cox, M. L. Perl, Michael N. Kreisler, and Michael J. Longo, Physical Review Letters 21, 645 (1968); M. L. Perl, J. Cox, Michael J. Longo, and M. N. Kreisler, Physical Review D (to be published).

3. R. Hagedorn, Relativistic Kinematics (W. A. Benjamin, Inc., New York, 1963) pp. 69-79.

4. J. L. Friedes, H. Palevsky, R. L. Stearns, and R. J. Sutter, Physical Review Letters 15, 38 (1965).

5. G. Manning, A. G. Parham, J. D. Jafar, H. B. van der Raay, D. H. Reading, D. G. Ryan, B. D. Jones, J. Malos, and N. H. Lipman, Nuovo Cimento 41, 167 (1966).

6. Richard Wilson, Annals of Physics 32, 193 (1965).

7. R. E. Mischke, P. F. Shepard, and Thomas J. Devlin, Physical Review Letters 23, 542 (1969); P. F. Shepard, T. J. Devlin, R. E. Mischke, and J. Solomon,

Princeton-Pennsylvania Accelerator Report No. PPAR-10, Princeton University, Princeton, New Jersey (1969).

8. A reprint of Hideki Yukawa's original paper may be found in the Supplement of the Progress of Theoretical Physics 1, 1 (1955).

9. J. Iwadare, S. Otsuki, R. Tamagaki, and W. Watari, Supplement of the Progress of Theoretical Physics 3, 32 (1956).

10. Vernon D. Barger and David B. Cline, Phenomenological Theories of High Energy Scattering (W. A. Benjamin, Inc., New York, 1969) p. 10.

11. Geoffrey F. Chew, Physical Review 112, 1380 (1958).

12. N. S. Amaglobeli and Yu. M. Kazarinov, Soviet Physics JETP 37, 1125 (1960).

13. R. R. Larsen, Nuovo Cimento 18, 1039 (1960).

14. A. Ashmore, W. H. Range, R. T. Taylor, B. M. Townes, L. Castillejo, and R. F. Peierls, Nuclear Physics 36, 258 (1962).

15. S. D. Drell, Reviews of Modern Physics 33, 458 (1961).

16. Ivan J. Muzinich, Physical Review 130, 1571 (1963); Physical Review Letters 11, 88 (1963).

17. M. M. Islam and T. W. Preist, Physical Review Letters 11, 444 (1963).

18. Akbar Ahmadzadeh, Physical Review 134, B633 (1964).

19. Victor Flores-Maldonado, Physical Review 155, 1773 (1967); Physical Review Letters 17, 113 (1966).

20. R. J. N. Phillips, Physics Letters 4, 19 (1963).

21. K. Gottfried and J. D. Jackson, Nuovo Cimento $\underline{34}$, 735 (1964).

22. G. A. Ringland and R. J. N. Phillips, Physics Letters $\underline{12}$, 62 (1964).

23. E. M. Henley and I. J. Muzinich, Physical Review $\underline{136}$, B1783 (1964).

24. Loyal Durand,III and Yam Tsi Chiu, Physical Review $\underline{137}$, B1530 (1965).

25. Farzam Arbab and Jan W. Dash, "Regge Pole Analysis of $pn \rightarrow np$ and $p\bar{p} \rightarrow n\bar{n}$ Scattering", UCRL-17585, Lawrence Radiation Laboratory, University of California, Berkeley, California (1967).

26. Elliot Leader, Physcial Review $\underline{166}$, 1599 (1968).

27. R. J. N. Phillips, Nuclear Physics $\underline{B2}$, 394 (1967).

28. F. Henyey, G. L. Kane, Jon Pumplin, and M. H. Ross, Physical Review $\underline{182}$, 1579 (1969).

29. N. Byers and C. N. Yang, Physical Review $\underline{142}$, 976 (1966).

30. Nina Byers, Physical Review $\underline{156}$, 1703 (1967).

31. Marc Ross, Regge Pole Conference, University of California at Irvine, 1969 (unpublished); G. Williamson et al. (to be published).

32. G. L. Kane, private communication. (February 1970).

33. Dow Corning Corporation, Midland, Michigan

34. D. H. Nelson and P. G. Watson, LRL Engineering Notes MT-188 and MT-189, Book No. 461, Lawrence Radiation Laboratory, University of California, Berkeley,

California (1964).

35. Sylvania Type PPF plastic "Panelescent" lamps with green phosphor, rated at 115 volts ac.

36. Arpad Barna, Michael N. Kreisler, and Michael J. Longo, Review of Scientific Instruments 37, 521 (1966).

37. D. E. Damouth and O. E. Haas, "A Pulsed Rapid Film Advance Camera", Technical Report No. 13, Department of Physics, University of Michigan, Ann Arbor, Michigan (1963).

38. Tom Innes and Quentin Kerns, "Triggered Nanosecond Pulsed Light Source", Lawrence Radiation Laboratory Report UCRL-9726, (1961).

39. Thomas P. Clements and Lester Winsberg, "Polynomial Fits of Nucleon-Nucleon Scattering Data", Lawrence Radiation Laboratory Report No. UCRL-9043, University of California, Berkeley, California (1960).

40. Richard J. Kurz, "A 709/7090 FORTRAN II Program to Compute the Neutron-Detection Efficiency of Plastic Scintillator for Neutron Energies from 1 to 300 MeV", Lawrence Radiation Laboratory Report No. UCRL-11339, University of California, Berkeley, California (1964).

41. D. G. Crabb, J. G. McEwen, E. G. Auld, and A. Langsford, Nuclear Instruments and Methods 48, 87 (1967).

42. Kimio Fujimura, Supplement of the Progress of Theoretical Physics 41 and 42, 282 (1967).